

**Photoproduction of Open Charm  
in  $ep$  - Collisions at HERA**

Dissertation

zur

Erlangung der naturwissenschaftlichen Doktorwürde  
(Dr. sc. nat.)

vorgelegt der

Mathematisch-naturwissenschaftlichen Fakultät  
der

Universität Zürich

von

Martin zur Nedden  
aus Österreich

Begutachtet von  
Prof. Dr. Peter Truöl  
und Dr. Felix Sefkow

Zürich 1998

Die vorliegende Arbeit wurde von der Mathematisch-naturwissenschaftlichen Fakultät der Universität Zürich auf Antrag von Prof. Dr. Peter Truöl und Prof. Dr. Roland Engfer als Dissertation angenommen.

## Abstract

In positron-proton collisions at the storage ring HERA heavy quarks are produced very copiously. Two kinematical regions are distinguished according to the momentum transfer squared  $Q^2$ : deep inelastic scattering (DIS,  $Q^2 > 2 \text{ GeV}^2$ ) and photoproduction ( $\gamma p$ ,  $Q^2 < 0.01 \text{ GeV}^2$ ). In the case of photoproduction the electron beam acts as a source of quasi real on-shell photons, the electron is scattered under very small angles emitting a photon. In Quantum Chromo Dynamics (QCD), in lowest order perturbation theory charm quarks are produced mainly directly via photon gluon fusion. Alternatively, in the so-called resolved process, the photon fluctuates into a hadronic state before the interaction and the charm quark is produced mainly by gluon gluon coupling. The processes are sensitive to the parton densities in the proton and the photon.

If the charm quark fragments into a  $D^*$  meson, the decay products can be observed in the H1-detector ( $c \rightarrow D^{*\pm} \rightarrow (K^{\mp}\pi^{\pm})\pi_s^{\pm}$ ). In this thesis measurements for the single and double differential cross sections at an average center of mass energy  $\overline{W}_{\gamma p} = 196 \text{ GeV}$  are presented and compared to theoretical calculations in next to leading order QCD. These calculations are either performed in the so-called massive scheme, where charm quarks are produced in the hadronic final state only, or in the massless scheme, where charm quarks are treated also as massless partons in the initial state.

Good agreement between data and predictions is observed for the massive scheme in the low transverse momentum range ( $p_{\perp} < 5 \text{ GeV}$ ) as expected by the theory. In the medium  $p_{\perp}$  range ( $3.5 \text{ GeV} < p_{\perp} < 5.5 \text{ GeV}$ ) both calculations describe the data reasonably well. For the high transverse momenta region the statistical accuracy is not yet good enough for final conclusions. The measurements are also compared to various parameterizations of the photon and proton parton density function in the massive scheme and to different variants of the fragmentation function.

## Zusammenfassung

Bei Positron-Proton Kollisionen im Speicherring HERA werden unter anderem auch schwere Quarks produziert. Je nach Impulsübertrag zum Quadrat  $Q^2$ , wird dabei zwischen zwei verschiedenen kinematischen Bereichen unterschieden, der tief unelastischen Streuung (DIS,  $Q^2 > 2 \text{ GeV}^2$ ) und der Photoproduktion ( $\gamma p$ ,  $Q^2 < 0.01 \text{ GeV}^2$ ). In der Photoproduktion, die hier untersucht wird, wirkt der Elektronenstrahl als Quelle quasi-reeller Photonen. Das Elektron wird unter sehr kleinen Winkeln gestreut und emittiert dabei ein Photon. In niedrigster Ordnung quantenchromodynamischer Störungstheorie (QCD) werden Quark-Antiquark Paare mit Charm direkt durch eine Photon-Gluon Fusion erzeugt. Fluktuiert das Photon vor der Wechselwirkung in einen hadronischen Zustand, wird das Paar im sogenannten aufgelösten Prozeß vorwiegend durch eine Gluon-Gluon Kopplung erzeugt. Die Prozesse sind direkt sensitiv auf die Parton-Dichte-Verteilungen im Proton und im Photon.

Wenn das Charm-Quark in ein  $D^*$  Meson fragmentiert, können dessen Zerfallsprodukte im H1-Detektor beobachtet werden ( $c \rightarrow D^{*\pm} \rightarrow (K^\mp \pi^\pm) \pi_s^\pm$ ). In dieser Arbeit werden Meßresultate für die einfach und doppelt differenziellen Wirkungsquerschnitte in diesem Kanal der Photoproduktion bei einer Schwerpunktsenergie von  $\overline{W}_{\gamma p} = 196 \text{ GeV}$  präsentiert. Diese Daten werden mit zwei verschiedenen theoretischen Rechnungen verglichen, in denen die Charm-Quarks entweder nur als massive Teilchen im hadronischen Endzustand, oder auch als masselose Partonen im Anfangszustand behandelt werden.

Im Bereich kleiner Transversalimpule  $p_\perp$  ( $p_\perp < 3.5 \text{ GeV}$ ) beobachtet man gute Übereinstimmung im massiven Ansatz, bei höheren Transversalimpulsen ( $p_\perp > 5.0 \text{ GeV}$ ) läßt die unzureichende Ereigniszahl noch keine endgültigen Schlüsse zu, im Übergangsbereich ( $3.5 \text{ GeV} < p_\perp < 5.5 \text{ GeV}$ ) beschreiben beide Rechnungen die Daten hinreichend gut. Im Modell der massiven Quarks werden die Daten auch mit Vorhersagen verglichen, die verschiedene Parametrisierungen der Parton-Dichten im Photon und Proton, sowie verschiedene Varianten der Peterson Fragmentationsfunktion verwenden.

# Contents

|          |                                                               |           |
|----------|---------------------------------------------------------------|-----------|
| <b>1</b> | <b>Physics of electron - proton collisions at HERA</b>        | <b>1</b>  |
| 1.1      | Overview of physics at HERA . . . . .                         | 1         |
| 1.1.1    | Physics program . . . . .                                     | 2         |
| 1.2      | Kinematics at HERA . . . . .                                  | 3         |
| <b>2</b> | <b>Charm production and decay</b>                             | <b>7</b>  |
| 2.1      | The Weizsäcker-Williams Approximation . . . . .               | 7         |
| 2.2      | Charm production at HERA . . . . .                            | 9         |
| 2.3      | QCD calculations in the massive scheme . . . . .              | 9         |
| 2.3.1    | Differential distributions of charm cross sections . . . . .  | 13        |
| 2.3.2    | Charm photoproduction at large $p_{\perp}$ . . . . .          | 16        |
| 2.4      | QCD calculations in the massless scheme . . . . .             | 17        |
| 2.4.1    | Photoproduction cross section calculations . . . . .          | 17        |
| 2.4.2    | Differential distributions . . . . .                          | 19        |
| 2.5      | Comparison of the massive and the massless approach . . . . . | 21        |
| <b>3</b> | <b>HERA and the H1-experiment</b>                             | <b>23</b> |
| 3.1      | The HERA ring . . . . .                                       | 23        |
| 3.2      | The experiment H1 . . . . .                                   | 26        |
| 3.2.1    | The tracking system . . . . .                                 | 28        |
| 3.2.2    | The luminosity system . . . . .                               | 31        |
| 3.2.3    | The trigger system . . . . .                                  | 31        |
| 3.3      | Performance of the inner z-drift chamber CIZ . . . . .        | 34        |
| <b>4</b> | <b>Event selection</b>                                        | <b>43</b> |
| 4.1      | Kinematics of events with charm . . . . .                     | 43        |
| 4.1.1    | General properties of $D^*$ events . . . . .                  | 44        |
| 4.1.2    | Detector motivated cuts on kinematical variables . . . . .    | 45        |
| 4.2      | Online data selection . . . . .                               | 47        |
| 4.2.1    | L1 Trigger and the photoproduction subtriggers . . . . .      | 47        |
| 4.2.2    | Filter farm and event classification . . . . .                | 49        |
| 4.3      | Offline data selection . . . . .                              | 50        |
| 4.4      | Luminosity . . . . .                                          | 54        |

|          |                                                                            |            |
|----------|----------------------------------------------------------------------------|------------|
| 4.4.1    | Electron-tagger acceptance . . . . .                                       | 55         |
| 4.5      | The $D^*$ signal . . . . .                                                 | 55         |
| 4.5.1    | Fit method . . . . .                                                       | 56         |
| <b>5</b> | <b>Measurement of charm cross sections</b>                                 | <b>59</b>  |
| 5.1      | General aspects of cross section measurement . . . . .                     | 60         |
| 5.2      | Determination of the number of events . . . . .                            | 61         |
| 5.2.1    | Fitting technique . . . . .                                                | 61         |
| 5.2.2    | Results of the fits . . . . .                                              | 63         |
| 5.3      | Acceptance and efficiencies . . . . .                                      | 67         |
| 5.3.1    | The method used for efficiency determination . . . . .                     | 67         |
| 5.3.2    | Acceptance corrections . . . . .                                           | 69         |
| 5.3.3    | Reconstruction efficiencies . . . . .                                      | 69         |
| 5.3.4    | Trigger efficiency . . . . .                                               | 72         |
| 5.4      | Systematic studies . . . . .                                               | 73         |
| 5.5      | Raw Data Spectras . . . . .                                                | 74         |
| 5.6      | The total cross section $\sigma(\gamma p \rightarrow c\bar{c}X)$ . . . . . | 76         |
| 5.7      | Differential cross sections . . . . .                                      | 77         |
| <b>6</b> | <b>Comparison to theory</b>                                                | <b>80</b>  |
| 6.1      | Comparison to Monte Carlo generators . . . . .                             | 80         |
| 6.1.1    | AROMA-IJRAY . . . . .                                                      | 80         |
| 6.1.2    | HERWIG . . . . .                                                           | 83         |
| 6.2      | Comparison to the massive calculations . . . . .                           | 87         |
| 6.3      | Comparison to the massless calculations . . . . .                          | 92         |
| <b>7</b> | <b>Conclusions</b>                                                         | <b>97</b>  |
| <b>A</b> | <b>Tables of efficiencies and cross sections</b>                           | <b>98</b>  |
|          | <b>Bibliography</b>                                                        | <b>100</b> |
|          | <b>List of tables</b>                                                      | <b>104</b> |
|          | <b>List of figures</b>                                                     | <b>105</b> |
|          | <b>Acknowledgments</b>                                                     | <b>109</b> |
|          | <b>Curriculum Vitae</b>                                                    | <b>110</b> |

# Chapter 1

## Physics of electron - proton collisions at HERA

This chapter briefly describes the physics of  $ep$  collisions at HERA [1, 2]. The center of mass energy reached at HERA ( $\sqrt{s_{ep}} \approx 300$  GeV), the worldwide unique electron-proton storage ring, lies more than one order of magnitude above the energies achieved in earlier lepton-nucleon scattering experiments. This allows to progress to a previously uninvestigated kinematical region with four-momentum transfers squared up to  $Q^2 \approx 10^5$  GeV/c<sup>2</sup>, leading to a spatial resolution of  $\Delta \approx \hbar/Q^2 \approx 10^{-18}$  m. This is three orders of magnitude lower than the proton radius. The higher the momentum transfer  $Q^2$  the smaller the objects 'inside' the proton that can be 'observed'. These objects, quarks and gluons, carry a fraction  $x$  (Björken- $x$ ) of the proton momentum, and are generally called "partons". At HERA also the region of  $x$ , is extended to very low values ( $x \approx 10^{-5}$ ).

In the second part of this chapter the kinematical variables used to describe the  $ep$  events are defined, and the accessible kinematical regions of HERA are compared to those of earlier experiments.

### 1.1 Overview of physics at HERA

Scattering experiments play a central role in the exploration of the structure of matter. The basic concept is quite simple: a point-like and energetic test particle is scattered on the probe and its angular and energy distribution are measured. One of the earliest example is the experiment of Rutherford (1909), who let  $\alpha$  particles scatter on a gold foil. The observation of particles scattered at large angles led Rutherford to the assumption of a hard nucleus in the atom.

The structure of the nucleon has been explored mostly and very successfully with lepton beams. Elastic scattering of electrons with beam energies of the order of 1 GeV showed, that the proton is an extended object with a radius of the order of 1 fm (1966) [3]. Inelastic scattering of 20 GeV electrons on nucleons at SLAC

(1969)<sup>1</sup> [4] observed approximate scaling of the structure functions [5] resulting from scattering on charged, point-like constituents in the nucleon as explained by the quark parton models. The structure function  $F_2$  describes the sum over all quark densities in the proton for partons with spin  $\frac{1}{2}$  and 0. If  $F_2$  depends only on  $x$  and not on  $Q^2$ , it is called “scaling”. The observation of logarithmic violation of scaling ([7], [8]), which became particularly clear with beam energies of several hundred GeV (1976), was very basic for the formulation of Quantum Chromo Dynamics (QCD) ([9], [10]). Scaling appears in a static quark parton model. If the model is expanded to a dynamic one, which takes the strong interaction between the quarks into account, the quarks can radiate off gluons building new quark antiquark pairs. Therefore the parton densities, and also the structure functions, depend then also on  $Q^2$ . This is called scaling violation.

The object size  $\Delta$  that can be reached in the scattering process is determined by the momentum transfer  $Q^2$  via the uncertainty  $\Delta \approx \hbar/Q$ . Better resolution requires larger momentum transfers and therefore higher energies. A storage ring, where the test particles (electrons,  $E_e = 27.5$  GeV) and the probe particles (protons,  $E_p = 820$  GeV) collide head-on, is the best facility to achieve the necessary energies. With the electron proton collider HERA at DESY, a center of mass energy of 300 GeV can be reached compared to 30 GeV in fixed target experiments. HERA vastly increases the available phase space and hence also the physics potential for lepton nucleon scattering, the maximum momentum transfer  $Q$  is rising by a factor of ten and the energy transfer by a factor of hundred. The richness of present and future HERA physics has been subject of three recent workshops held in 1987 [11], 1991 [12] and 1996 [13].

The most important scattering process at HERA is deep inelastic scattering (**DIS**) of electrons on quarks of the proton, where an electron or a neutrino appears in the final state. This leads to values of the momentum transfer where the contributions of the weak interaction are of the same order as the electromagnetic contributions, or even higher. An other interesting field of HERA physics is the investigation of photon-proton interactions (**photoproduction**  $\gamma p$ ) at center of mass energies of about 200 GeV. The bremsstrahlung from the electron is a source of high energetic quasi real photons at very low momentum transfers ( $Q^2 \approx 0$ ).

### 1.1.1 Physics program

Some of the main areas of HERA physics are briefly listed below:

- **Search for substructures in quarks and leptons:**

An important part in the extensive physics program of HERA is the test of the standard model and the search for physics beyond it. The new particles, predicted by various theoretical models, could be seen with masses up to 250 GeV/c<sup>2</sup>, as for example a bound state of quarks and leptons.

---

<sup>1</sup>SLAC: **S**tanford **L**inear **A**ccelerator **C**enter.

- **Measurement of the proton structure function:**

Apart from its phenomenological meaning the measurement of the structure functions provides an important test of the QCD prediction covering a big region in  $Q^2$  and  $x$ .

- **Measurement of the momentum distribution of quarks and gluons at low  $x$  values:**

The high center of mass energy of HERA opens the possibility to measure parton densities at very low values of  $x$  (“soft partons”). There are theoretical reasons for a sharp rise of the parton densities with decreasing  $x$ , but below a critical value of  $x$  saturation effects due to recombination of partons are expected. They prevent an unlimited increase of the parton densities.

- **Investigation of the structure of the photon:**

Apart from the measurement of the total photon-proton cross section, analysis of hard scattering processes in photoproduction can give some important informations about the quark and gluon distributions in the photon.

- **Measurement of heavy quarks:**

Charm and bottom quarks are produced at HERA very copiously. The analysis of processes with heavy quarks delivers detailed information about the production mechanism. The production rates are very sensitive to the parton density functions within the proton and the photon. The high production rates lead to a better sensitivity in the search for rare or forbidden decays of heavy quarks. They are predicted by many theories beyond the standard model.

Of course, this is only an incomplete overview, a complete collection of the enormous physics program of HERA can be found in [11] - [13].

## 1.2 Kinematics at HERA

In deep inelastic scattering the incoming electron couples to an electroweak current, which probes the structure of the proton. The basic deep inelastic scattering process (DIS) is illustrated in Figure 1.1. For a momentum transfer  $Q^2$  much larger than the mass squared of the proton, the proton can be thought of as a group of quasi-free partons (quarks and gluons). One of these interacts with the electroweak current while the rest of the group moves on unperturbed ( $p$  remnant). Depending on the charge of the exchanged boson, the electroweak current is called neutral (“neutral current” NC) or charged (“charged current” CC). While the neutral current exchanges a virtual photon  $\gamma$  or a  $Z^0$ -boson, respectively, the charged current consists of a charged  $W^\pm$  boson. They can be distinguished by the final state electron (NC) or neutrino (CC).

$$ep \rightarrow e'X: \text{NC}$$

$$ep \rightarrow \nu_e X: \text{CC}$$

Due to the high masses of the  $W$  and  $Z$  bosons, the exchange of photons is the dominant process.

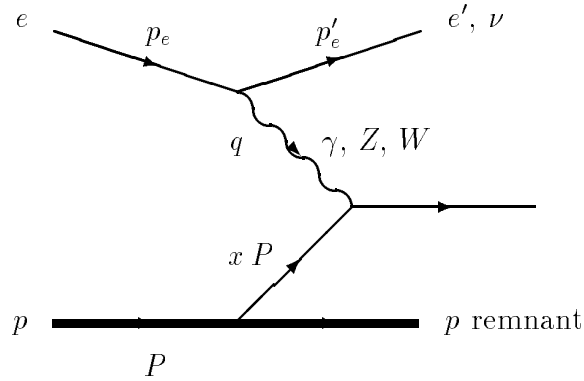


Figure 1.1: *The kinematics of a deep inelastic ep scattering event at HERA*

The large imbalance between the electron and proton beam energies ( $E_p = 820$  GeV,  $E_e = 27.5$  GeV) makes the kinematics at HERA quite different from that of other colliders where both beams have equal momenta or from fixed target experiments where the nucleon at rest. The relevant kinematic variables are the center of mass energy  $\sqrt{s}$ , the invariant mass of the hadronic final state  $W$ , the momentum transfer  $Q$  and the dimensionless Björken scale variables  $x$  and  $y$ . In the Quark Parton Modell  $x$  denotes the fraction of the proton momentum carried by the parton from the proton coupling to the electroweak current, and  $y$  corresponds to the relative energy loss of the electron in the center of mass system of the proton.

$$s := (p_e + P)^2 \quad (1.1)$$

$$W^2 := (P + q)^2 \quad (1.2)$$

$$Q^2 \equiv -q^2 := -(p_e - p'_e)^2 \quad (1.3)$$

$$y := \frac{P \cdot q}{P \cdot p_e} \quad (1.4)$$

$$x := \frac{Q^2}{2P \cdot q} \quad (1.5)$$

The relations are connected via:

$$Q^2 = x \cdot y \cdot s \quad (1.6)$$

where  $p_e$  is the momentum of the incoming electron,  $P$  the momentum of the proton and  $q$  the momentum transferred by the electroweak current. All momenta used in

equations 1.1 - 1.5 are four-vectors. If the electron and proton mass are neglected ( $m_e \ll E_e$ ,  $m_p \ll E_p$ ) the invariant mass of the hadronic final state  $W$  and the total center of mass energy  $\sqrt{s}$  can be written as:

$$W^2 = Q^2 \cdot \frac{1-x}{x} \quad (1.7)$$

$$\sqrt{s} \approx \sqrt{4 \cdot E_e \cdot E_p} = 300 \text{ GeV} \quad (1.8)$$

For fixed center of mass energy, inclusive scattering is described by two variables for which e.g.  $x$  and  $Q^2$  can be chosen. The same variables describe the lowest order process where the electron scatters elastically on a free constituent of the proton. For NC events these variables can be determined either from the energy  $E'_e$  and angle  $\vartheta_e$  of the scattered electron, or from the hadronic final state, or from a mixture of both. For CC events, only the hadron system is accessible for measurement. This is also the case for events in photoproduction ( $Q^2 \approx 0$ ) where the electron escapes into the beampipe before being measured in one of the electron taggers.

If  $E'_e$  is the energy and  $\vartheta_e$  the angle of the scattered electron measured with respect to the proton beam direction, the electron side yields:

$$Q_e^2 = 4 \cdot E_e \cdot E'_e \cdot \cos^2(\vartheta_e/2) \quad (1.9)$$

$$y_e = 1 - \frac{E'_e}{E_e} \cdot \sin^2(\vartheta_e/2) \quad (1.10)$$

All other variables can now be extracted from equations 1.6 and 1.7.

Using the method of Jacquet-Blondel [6] the hadron variable can be determined approximately by summing the energies ( $E_h$ ), the transverse ( $p_{\perp,h}$ ) and longitudinal momenta ( $p_{z,h}$ ) of all hadronic final states particles. The method rests on the assumption that the total transverse momentum carried by those hadrons which escape the detector through the beam pipe in the proton beam direction can be neglected. The same assumption is made for the energy carried by the particles escaping through the beam pipe in electron beam direction. The formulas read as:

$$Q_{JB}^2 = \frac{(\sum_h p_{x,h})^2 + (\sum_h p_{y,h})^2}{(1 - y_{JB})}, \text{ where} \quad (1.11)$$

$$y_{JB} = \frac{\sum_h (E_h - p_{z,h})}{2 \cdot E_e} \quad (1.12)$$

For events in photoproduction ( $Q^2 \approx 0$ ) the electron is scattered under very low polar angles  $\vartheta_e$ . If the electron does not escape detection through the beampipe and it is tagged by one of the electron taggers, equation 1.10 can be simplified to:

$$y_e \approx 1 - \frac{E'_e}{E_e} = \frac{E_e - E'_e}{E_e} = \frac{E_\gamma}{E_e} \quad (1.13)$$

with the photon energy  $E_\gamma$ . The center of mass energy of the photon-proton system is given from equations 1.6 and 1.7:

$$W_{\gamma p} = \sqrt{y \cdot s - Q^2} \approx \sqrt{y \cdot s} = 2 \cdot \sqrt{y \cdot E_e \cdot E_p} \quad (1.14)$$

To describe the hadronic final state also the rapidity or pseudorapidity is used apart from the momenta and angles of the particles. The rapidity  $\hat{y}$  of a particle with the Energy  $E$  and the longitudinal momentum  $p_z$  is defined as:

$$\hat{y} := \frac{1}{2} \ln\left(\frac{E + p_z}{E - p_z}\right) \quad (1.15)$$

If the mass of the particle is small compared to its energy ( $m \ll E$ ), the rapidity can be approximated by the pseudorapidity  $\eta$  by replacing the energy by the momentum:

$$\eta := \frac{1}{2} \ln\left(\frac{p + p_z}{p - p_z}\right) = \frac{1}{2} \ln\left(\frac{1 + \cos(\vartheta)}{1 - \cos(\vartheta)}\right) = -\frac{1}{2} \ln(\tan(\vartheta/2)) \quad (1.16)$$

The rapidity is a Lorentz invariant variable and closely related to the polar angle distribution, whereas the pseudorapidity is Lorentz invariant apart from an additive constant.

In Table 1.1 a comparison of the kinematical ranges accessible at HERA and in previous lepton nucleon experiments is given:

|                                                | <b>HERA</b>       | <b>pre - HERA</b> |
|------------------------------------------------|-------------------|-------------------|
| $s$ [GeV <sup>2</sup> ]                        | 10 <sup>5</sup>   | 10 <sup>3</sup>   |
| maximal $Q^2$ [GeV <sup>2</sup> ]              | 40000             | 400               |
| spatial resolution $\Delta$ [m <sup>-1</sup> ] | 10 <sup>-18</sup> | 10 <sup>-16</sup> |
| maximal Energy transfer $\nu$ [GeV]            | 52000             | 500               |
| minimum $x$ at $Q^2 = 10$ GeV <sup>2</sup>     | 10 <sup>-4</sup>  | 10 <sup>-2</sup>  |

Table 1.1: *Kinematic regions accessible at HERA and in previous experiments*

The maximum energy transfer is increased by a factor of  $\sim 100$ : HERA is equivalent to a fixed target experiment with an incident electron beam of 52 TeV, or in the case of photproduction to an incident photon energy of 40 TeV. The domain in  $Q^2$  over which electron proton scattering can be measured is also increased by two orders of magnitude. Since the typical  $Q^2$  values in DIS are much larger than the proton mass, the electron interacts only with one of the partons out of the proton. HERA can therefore be regarded as a parton - electron collider.

# Chapter 2

## Charm production and decay

In this chapter the basic theoretical ideas concerning charm photoproduction at high energies are described. We start with a brief phenomenological overview of the production mechanism in a leading order QCD picture. In this approximation charm photoproduction has two sources: the direct process, where the proton interacts via a  $c\bar{c}$ -quark pair directly with a gluon of the proton, and the resolved (or hadronic) process, where the photon fluctuates into a hadronic state before the interaction. The direct process dominates.

There are two approaches to describe these processes in QCD, loosely termed “massive” and “massless”. In the massive approach the active flavours in the proton are the light ones only ( $N_f = 3$ ) and charm is produced during the interaction. In the massless case charm is assumed as an intrinsic flavour of the proton ( $N_f = 4$ ) and the charm quark is treated as a massless parton. While the massive scheme delivers good results for the low  $p_\perp$  region, the massless scheme is expected to describe the higher  $p_\perp$  region.

The electroproduction cross section is connected to the photoproduction cross section via the Weizsäcker-Williams Approximation (WWA), describing the probability of emission of a photon by the scattered electron.

### 2.1 The Weizsäcker-Williams Approximation

Photoproduction events are characterized by very moderate momentum transfer  $Q^2$ . The separation of these events from events in deep inelastic scattering (DIS) is done by a detector motivated kinematical cut:

- **Photoproduction:**

- tagged:  $Q^2 < 0.01 \text{ GeV}^2$
- untagged:  $Q^2 < 2.0 \text{ GeV}^2$

- **Deep inelastic scattering:**  $Q^2 > 2 \text{ GeV}^2$

In the photoproduction case, the electron is scattered under very low polar angle  $\vartheta_e$  and escapes the main detector. The photon emitted by the electron interacts with the proton.

Using the extended Weizsäcker Williams Approximation ([15]-[17]) the connection of electro- and photoproduction cross section can be written as:

$$\sigma_{ep} = \int_{y_{min}}^{y_{max}} dy \int_{Q_{min}^2}^{Q_{max}^2} dQ^2 F_{\gamma/e}(y, Q^2) \sigma_{\gamma p}(ys) \quad (2.1)$$

The cross section factorizes according to 2.1 into a photon proton cross section depending on  $W_{\gamma p} = \sqrt{ys}$  and into the photon flux  $F_{\gamma/e}(y, Q^2)$ . The photon flux factor  $F_{\gamma/e}$  denotes the probability of the emission of a photon by the electron ( $e \rightarrow e'\gamma$ ):

$$F_{\gamma/e}(y, Q^2) = \frac{\alpha_{em}}{2\pi Q^2} \left( \frac{1 + (1-y)^2}{y} - \frac{2(1-y)}{y} \cdot \frac{Q_{min}^2(y)}{Q^2} \right) \quad (2.2)$$

where  $\alpha_{em}$  is the electromagnetic coupling constant and  $Q_{min}^2 = (m_e y)^2 / (1-y)$  gives the minimal virtuality of the photon. Integration over  $Q^2$  leads to:

$$\frac{d\sigma_{ep}(s)}{dy} = \int_{Q_{min}^2}^{Q_{max}^2} dQ^2 F_{\gamma/e}(y, Q^2) \cdot \sigma_{\gamma p}^{tot}(W_{\gamma p}) = f_{\gamma/e}(y) \sigma_{\gamma p}^{tot}(W_{\gamma p}) \quad (2.3)$$

with

$$f_{\gamma/e} = \frac{\alpha_{em}}{2\pi} \left( \frac{1 + (1-y)^2}{y} \ln\left(\frac{Q_{max}^2}{Q_{min}^2}\right) - \frac{2(1-y)}{y} \left(1 - \frac{Q_{min}^2}{Q_{max}^2}\right) \right) \quad (2.4)$$

$Q^2$  is constrained by experimental conditions. The first term on the right hand side of equation 2.4 is coming from the original WWA [15], the second one is a correction term, which is not negligible at HERA [17] and is of the order  $\mathcal{O}(7\%)$ . A mean value over the measured region in  $W_{\gamma p}$  of  $f_{\gamma/e}$  can be determined under the assumption that the cross section does not strongly depend on  $W_{\gamma p}$  or on  $y$ :

$$\sigma_{ep}(\bar{y}) = \sigma_{\gamma p}(\bar{y}) \cdot \int dy f_{\gamma/e}(y). \quad (2.5)$$

This relation is used later to extract the photoproduction cross sections from the measured electroproduction cross section.

## 2.2 Charm production at HERA

The  $ep$  collisions of HERA offer a good opportunity to study the charm production mechanism and to test the prediction of perturbative QCD. Charm production in high energy  $ep$  collisions at HERA is dominated by photoproduction events, where the electron (positron<sup>1</sup>) is scattered at a small angle ( $Q^2 \approx 0$ ). In leading order QCD (LO) the main process is photon gluon fusion where the photon interacts directly with the gluon from the proton producing a  $c\bar{c}$  pair in the final state ( $\gamma g \rightarrow c\bar{c}$ ). Apart from the direct photoproduction (BGF) charm production at HERA can proceed also via the resolved photoproduction process, where the photon fluctuates in a hadronic state and behaves therefore as a source of partons. They interact with the partons in the proton as for example  $gg \rightarrow c\bar{c}$ .

In Figure 2.1 the production mechanisms are shown in a leading order picture for the massive scheme, where the charm quark is produced during the interaction. In the massive scheme the active intrinsic flavours in the initial state are the light ones only (u,d and s,  $N_f = 3$ ) and the massive charm quark appears only in the final state.

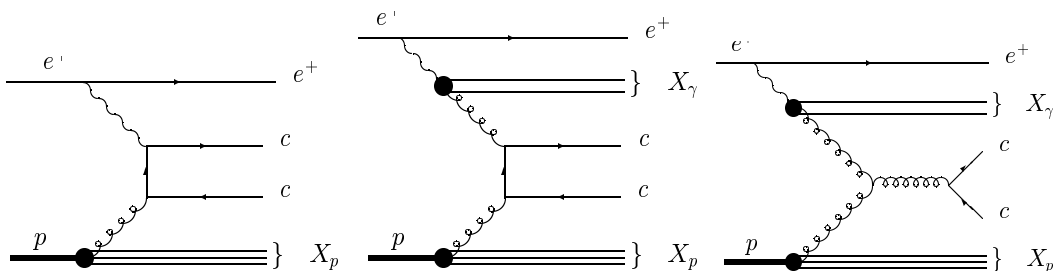


Figure 2.1: *Leading order charm photoproduction process: direct process (boson gluon fusion) (a) and resolved processes (b) and (c)*

## 2.3 QCD calculations in the massive scheme

In the case of photoproduction the electron can be considered to be equivalent to a beam of on-shell real photons. An on-shell photon has a finite probability to fluctuate into a hadronic state before undergoing a hard collision. In this case the photon is called “hadronic” (or “resolved”), in contrast to those events in which the photon interacts directly with the hadron (“point-like” or “direct”). Therefore the differential photoproduction cross section can be written as the sum of a point-like and a hadronic photon contribution ( $P_\gamma, P_p$ : momenta of photon/proton):

$$d\sigma^{(\gamma p)}(P_\gamma, P_p) = d\sigma_{direct}^{(\gamma p)}(P_\gamma, P_p) + d\sigma_{resolved}^{(\gamma p)}(P_\gamma, P_p) \quad (2.6)$$

<sup>1</sup>In the years 1994 - 1997 HERA was running with positrons instead of electrons, due to longer beam life times using positron beams. The word electron stands for positrons as well.

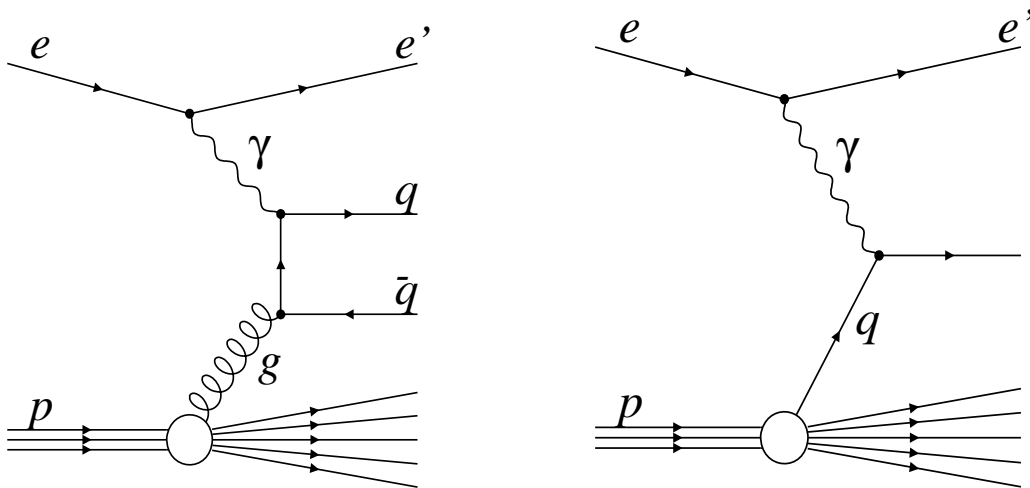


Figure 2.2: *Leading order picture for photoproduction of charmed mesons: massive scheme (a) versus massless scheme (b)*

The charm quark mass  $m_c = 1.5 \text{ GeV} \gg \Lambda_{QCD} = 151 \text{ MeV}$  acts as a cut-off parameter and sets the scale for the perturbative calculation. The cross section factorizes into a partonic hard-scattering cross section multiplied by densities of light quarks and gluons [14]. Thanks to the factorization theorem of perturbative QCD, the cross section can be written as follows, if the process is described by a hard scale:

$$d\sigma_{direct}^{(\gamma p)}(P_\gamma, P_p) = \sum_j \int dx f_j^{(p)}(x, \mu_F) \times d\hat{\sigma}_{\gamma j}(P_\gamma, xP_p, \alpha_s(\mu_R), \mu_F, \mu_\gamma) \quad (2.7)$$

$$d\sigma_{resolved}^{(\gamma p)}(P_\gamma, P_p) = \sum_{ij} \int dx dy f_i^{(\gamma)}(x, \mu_\gamma) f_j^{(p)}(y, \mu'_F) \times d\hat{\sigma}_{ij}(xP_\gamma, yP_p, \alpha_s(\mu'_R), \mu'_F, \mu_\gamma) \quad (2.8)$$

where:

- $i, j$ : indices running over all partons in the proton and the photon respectively,
- $f_j^{(p)}, f_i^{(\gamma)}$ : partonic densities in the proton and the photon,
- $\hat{\sigma}_{\gamma j}, \hat{\sigma}_{ij}$ : partonic cross sections for the interaction of a photon with a parton of type  $j$  in the proton (direct process) and of two partons of type  $i$  and  $j$  in the proton and photon (resolved process) respectively,
- $\alpha_S$ : strong coupling constant,
- $\mu_R, \mu'_R, \mu_F, \mu'_F$ : renormalization and factorization scales for the proton,

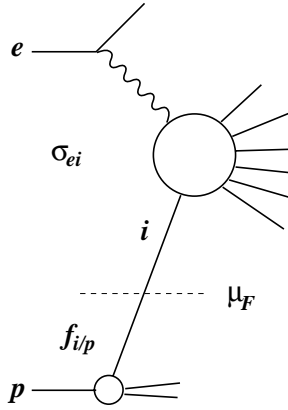


Figure 2.3: The factorizations scale  $\mu_F$ : cut between “long distance” and “short distance” physics.

- $\mu_\gamma$ : factorization scale for the photon for the resolved process.

The factorization scale  $\mu_F$  gives the cut between the physics of “short distances” (high energies) corresponding to the partonic cross section and the effects of the physics of “long distances” (small energies) which are absorbed into the partonic density functions:  $P_{p,\perp}^2, P_{\gamma,\perp}^2 < \mu_F^2$ : “long distances”,  $P_{p,\perp}^2, P_{\gamma,\perp}^2 > \mu_F^2$ : “short distances”. The partonic density functions and cross sections depends therefore on the choice of the factorization scale. This is indicated in Figure 2.3.

The  $f_j^{(p)}$  and  $f_i^{(\gamma)}$  partonic densities are universal, but not calculable in perturbation theory and need to be determined experimentally. They satisfy a renormalization group equation, which can be obtained in the proton case by slightly modifying the Altarelli-Parisi equation to the Dokshitzer - Gribov - Lipatov - Altarelli - Parisi (DGLAP) equation. For the photon case it reads<sup>2</sup>:

$$\frac{\partial f_i^{(\gamma)}}{\partial \log \mu^2} = \frac{\alpha_{em}}{2\pi} P_{i\gamma} + \frac{\alpha_S}{2\pi} \sum_j P_{ij} \otimes f_j^{(\gamma)} \quad (2.9)$$

The first term of equation 2.9 right hand side ( $P_{i\gamma}$ ), which is not present in the usual DGLAP - equation, results from the direct coupling of the photon to the quarks. At the lowest order we have (leading order LO):

$$P_{i\gamma} = N_c e_i^2 (x^2 + (1-x)^2) \quad (2.10)$$

where  $N_c = 3$  is the number of colours and  $e_i$  is the electric charge of the parton in the units of the charge of the electron (for gluons  $e_i = 0$ ).

The number of active flavours in the initial state is  $n_f = 3$ , while the massive charm quark appears only in the final state. The default value of the charm quark

<sup>2</sup>The symbol  $\otimes$  indicates convolution, i.e.:  $f(x) \otimes g(x) = \int_x^1 \frac{dz}{z} f(z)g(x/z)$ .

mass is chosen as  $m_c = 1.5$  GeV. The renormalization scale will be taken as  $\mu_R = \mu_0$ , and the factorization scale for the photon and the proton is set to  $\mu_F = \mu_\gamma = 2\mu_0$ , where  $\mu_0 = \sqrt{p_\perp^2 + m_c^2}$  and  $p_\perp$  is the transverse momentum of the scattered parton. It should be stressed that the direct and the resolved components of the photoproduction cross section are very closely related [19], and only their sum is physically meaningful. The separation of a cross section into a direct and a resolved component is ambiguous beyond leading order, it depends on the factorization scheme and scale. The photon parton densities are quite soft. Therefore, the resolved component is only important for large CM energies and small masses of the produced system. This process can therefore be used to constrain the densities in the photon, which are very poorly known at the moment.

The perturbative calculation ends in the massive scheme with massive charm quarks and massless partons (light quarks and gluons) in the final state. The fragmentation of charm quarks into a physical charmed meson ( $D^{*\pm}$ ) is described in [21], using the Peterson fragmentation function for the parameterization of the transition:

$$D(x) = \frac{1}{x(1 - 1/x - \epsilon/(1-x))^2} \quad (2.11)$$

where  $x$  is the fraction of the charm quark momentum and  $\epsilon$  is a free parameter describing the hardness of the fragmentation and needs to be determined experimentally. The value of  $\epsilon$  needs to be determined from a fit to data from  $e^+e^-$  experiments. These fits are performed in [22] and yields  $\epsilon_c = 0.06$ . For the photoproduction analysis  $\epsilon$  is chosen to be  $\epsilon = 0.035$  as obtained from recent NLO fits on LEP data [23]. In Figure 2.4 the function  $D(x)$  for different values of  $\epsilon$  is shown.

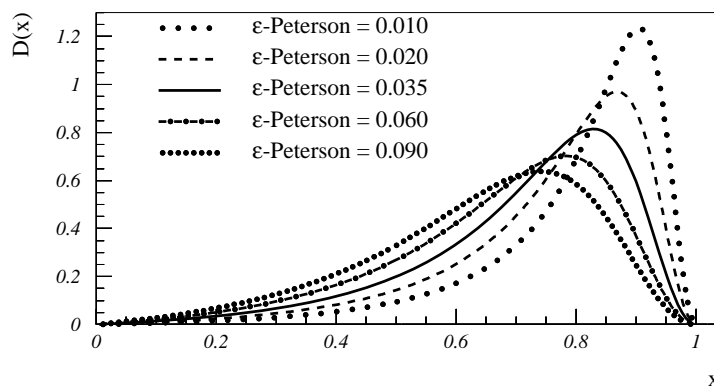


Figure 2.4: *The Peterson fragmentation function for  $\epsilon = 0.01, 0.02, 0.036, 0.06$  and  $0.09$ .*

### 2.3.1 Differential distributions of charm cross sections

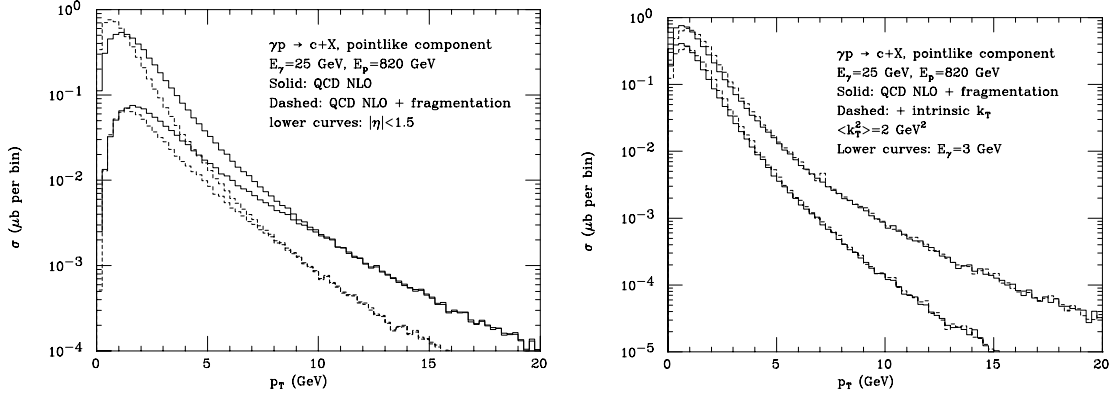


Figure 2.5: Charm transverse momentum distributions in photon proton collisions, showing the effects of applying a fragmentation function to the final state quark (a) and an intrinsic transverse momentum to the incoming parton (b) [20].

In this section, some results of next to leading order calculations are reproduced [20, 24, 25], which are based on the principles outlined above. The transverse momentum and pseudorapidity dependence of the direct contribution will be shown and the possibility be discussed, whether the resolved and the direct part can be separated with appropriate cuts.

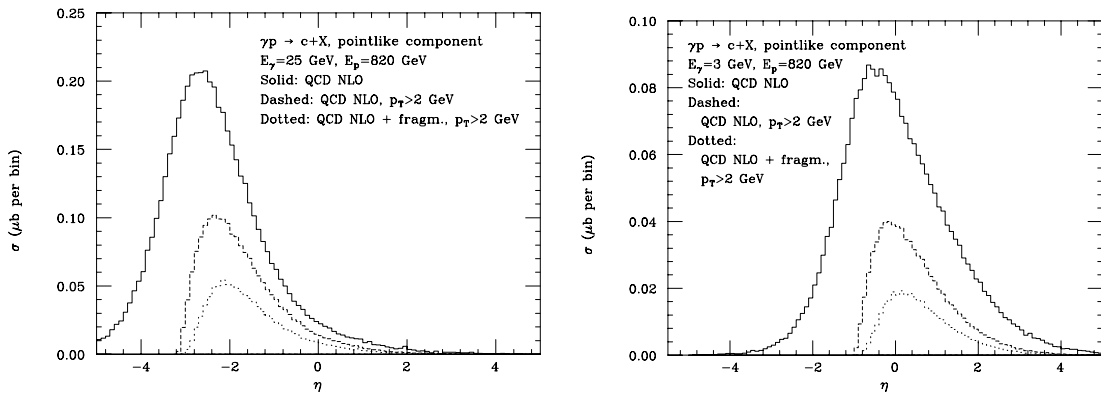


Figure 2.6: Charm pseudorapidity distribution in photon proton collisions showing the effect of fragmentation for  $E_\gamma = 25$  GeV (a) and  $E_\gamma = 3$  GeV (b) [20].

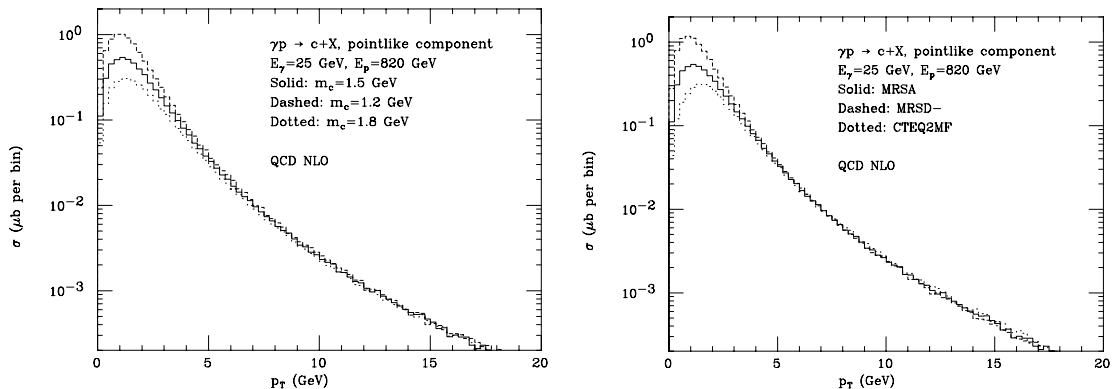


Figure 2.7: Sensitivity of the  $p_{\perp}$  distribution of charm to the charm mass and different parton densities [20].

## Direct component

In the following the set of parton densities MRSA [26] with  $\Lambda_5 = 151$  MeV is used<sup>3</sup>, with the default values of charm quark mass as well as the factorization and renormalization scale as given in section 2.3.

In Figure 2.5 the transverse momentum distribution of the charm quark at different photon energies is shown. Applying the Peterson fragmentation ( $\epsilon = 0.06$  here) softens the  $p_{\perp}$  spectrum considerably. The effect of assigning an intrinsic transverse momentum  $k_T$  to the incoming parton is also illustrated and found to be small even for a very large value ( $\langle k_T^2 \rangle = 2$  GeV<sup>2</sup>).

Pseudorapidity distributions are presented in Figure 2.6 for various photon energies. The direct contribution to the cross section peaks at large negative pseudorapidities, and tends to move towards the central region if a transverse momentum cut is applied. The fragmentation has little effect on the pseudorapidity of the charm quark, but degrades its transverse momentum. Fragmentation without transverse momentum cut is not well defined [28] and therefore not shown in the Figure.

In Figure 2.7 the sensitivity of the distributions to the various parameters that enter the computation is shown, e. g. the charm quark mass is varied between 1.2 and 1.8 GeV and two different parton densities (MRSD' [29], CTEQ2MG [30]) are compared. The shape of the  $p_{\perp}$  distribution (Figure 2.7) clearly depend on the quark mass and the parton density. No mass dependence is expected at high transverse momenta, while in the massless limit the cross section diverges at small momenta. Therefore smaller mass values lead to higher cross section at low  $p_{\perp}$ .

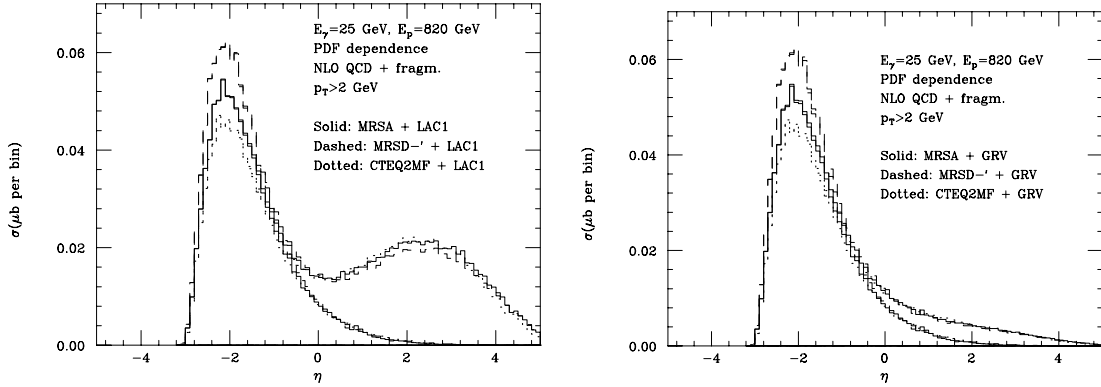


Figure 2.8: Sensitivity of the  $\eta$  distribution of charm to the parton and photon density functions LAC1 (a) and GRV (b) [20]. The direct contribution and the sum of direct and resolved processes are plotted separately.

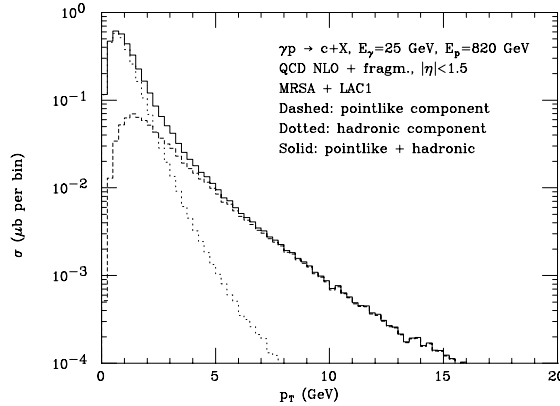


Figure 2.9: Transverse momentum distribution of the charm quark. The direct (pointlike, MRSA) and resolved contributions (hadronic, LAC1) are plotted separately [20].

### Resolved component

Different parton density functions of the photon for the resolved component of the charm production cross section (LAC1 [31], GRV [32]) can lead to quite different predictions. The resolved part may even dominate over the direct one. However the two components differ clearly in the pseudorapidity distribution, and whatever the choice of the photon density is, the resolved component favors positive values of  $\eta$ , i.e. the backward region (Figure 2.8). The shapes of the pseudorapidity distributions are very sensitive to the choice of the photon parton density functions and therefore to

<sup>3</sup>MRSA was updated to MRSG in [62] to include the new HERA deep inelastic scattering data. The shape of the distributions shown are not significantly different when the new parameterization is used.

the charm production mechanism. This offers an opportunity to distinguish among different density functions and should have measurable effects. Finally, Figure 2.9 presents the  $p_{\perp}$  distribution, separately for the direct and the resolved process and the sum of both. The resolved contribution drops with higher  $p_{\perp}$ , and can therefore be suppressed by a  $p_{\perp}$  cut.

### 2.3.2 Charm photoproduction at large $p_{\perp}$

New measurements at HERA of the differential cross section  $d\sigma/d\hat{y}, dp_{\perp}$  of inclusive  $D^{*\pm}$  production make it possible to test the theory in a different regime of scales. The experimental cross sections extend up to  $p_{\perp} = 12$  GeV, therefore the authors of [34] argue that  $p_{\perp}$  rather than  $m_c$  should be considered as the large scale. Because of the large photon - proton energies at HERA, the  $\ln(s/m_c^2)^4$  terms appearing in the charm cross section may get large and spoil the convergence of the perturbative series. Then, in NLO, terms proportional to  $\alpha_s \ln(p_{\perp}^2/m_c^2)$  arise from collinear gluon emission by charm quarks or from almost collinear branching of gluons or photons into charm - anticharm pairs (gluon-splitting). For large enough  $p_{\perp}$ , these terms are bound to spoil the convergence of the perturbative series and cause large scale dependences of the NLO result at  $p_{\perp} \gg m_c$ .

The proper procedure in the regime of large  $p_{\perp}$  ( $p_{\perp} \gg m_c$ ) is to absorb the terms proportional to  $\alpha_s \ln(p_{\perp}^2/m_c^2)$  into the perturbative fragmentation functions (FF) of charm quarks into charmed hadrons (i.e.  $D^*$ ). The transverse momentum distribution is in principle affected by the presence of  $\ln(p_{\perp}^2/m_c^2)$  terms. These logarithms can be resummed by observing that, at high  $p_{\perp}$ , the charm quark mass is negligible, and by using perturbative fragmentation functions. To perform this absorption information on the charm contribution to the parton density functions (PDF) and the fragmentation functions are needed. The fixed-order and the resummed results of [34] agree in a very wide range in  $p_{\perp}$ . The massless approach can therefore be used to predict the  $D^*$  spectra in the large  $p_{\perp}$  regime at HERA. At low and intermediate  $p_{\perp}$  regions and close to the phase space boundaries, the massive scheme gives the best results. It is one of the aims of this analysis to test the massless and the massive scheme and to study how well the data are described by the two schemes.

There are two major differences between the massive and the massless scheme. The PDF's are not the same because the massive scheme starts without a charm contribution in the proton and the photon, while in the massless scheme a content of massless charm in the proton and the photon is needed. Also the relative contributions of direct and resolved processes to the whole cross section are different. In the massive scheme, the visible resolved contribution is assumed to be very small, in the massless scheme it is of the same order as the direct contribution. Since the same behaviour is well known for light quarks, this is not surprising.

---

<sup>4</sup> $s(\text{theory})$  is  $W_{\gamma p}(\text{experimental})$  in this case.

## 2.4 QCD calculations in the massless scheme

In the massless approach, first proposed in reference [36] the number of active flavours in the proton is assumed to be  $N_f = 4$ ,  $q = u, d, s$  and  $c$ . The  $c$ -quark is also an ingoing parton originating either from the proton or the photon in case of a resolved process, as illustrated for the leading order in Figure 2.10. As already mentioned above, the massless scheme is valid in the region of large transverse momenta  $p_\perp \gg m_c$  [33]. In this scheme, the low  $p_\perp$ - region is not calculable and the cross section diverges in the limit  $p_\perp \rightarrow 0$ . The collinear singularities corresponding to the  $\alpha_s \ln(p_\perp^2/m_c^2)$  of the massive scheme are then absorbed into the charm quark parton density functions and the fragmentation functions in the same way as for the light  $u, d$  and  $s$  quarks.

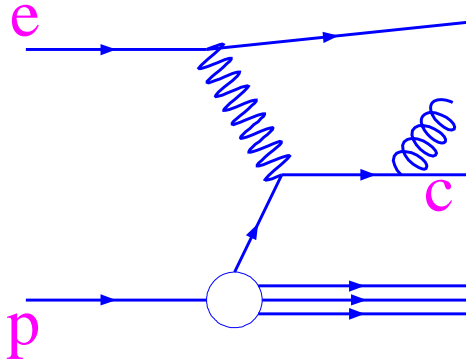


Figure 2.10: *Leading order charm photoproduction process in the massless scheme in a LO picture.*

### 2.4.1 Photoproduction cross section calculations

Sketching the NLO calculation in somewhat more detail, one can list the following steps, which are necessary to calculate the cross sections:

- The hard-scattering cross sections for the direct- and resolved-photon processes are calculated in the massless approach with  $N_f = 4$  active flavours. The collinear singularities are subtracted according to the  $\overline{MS}$  renormalization scheme.
- The charm quark is accommodated in the PDF's of the proton and photon as a light flavour. The finite mass of the charm quark is taken into account by including it in the evolution in a way, that its PDF's are only vanishing below a scale set by its mass.
- In the massless approach, the fragmentation functions FF have - as opposed to the massive scheme - a perturbative (PFF) *and* a non-perturbative part.

- The FF's characterize the hadronization of the massless partons, including the charm quark, into physical particles (i.e.  $D^*$ -mesons), and must be determined experimentally.
- For higher scales ( $\mu > \mu_0$ ) the PDF's, the non-perturbative FF's and the PFF's are evolved in NLO up to the chosen factorization scale via the Altarelli-Parisi equation and convoluted with the NLO hard-scattering cross section.

The large logarithmic terms proportional to  $\ln(p_\perp^2/m_c^2)$ , which appear in the massive scheme, are resummed in this approach by splitting them in three parts,

$$\ln\left(\frac{p_\perp^2}{m_c^2}\right) = \ln\left(\frac{p_\perp^2}{\mu^2}\right) + \ln\left(\frac{\mu^2}{\mu_0^2}\right) + \ln\left(\frac{\mu_0^2}{m_c^2}\right) \quad (2.12)$$

where  $\mu$  is some factorization scale. The part  $\ln(p_\perp^2/\mu^2)$  appears in the hard-scattering cross section, while the residual part proportional to  $\ln(\mu_0^2/m_c^2)$  is absorbed into the PDF's and FF's. It is treated with fixed order perturbation theory in the case of PDF's, or is part of the non-perturbative input in the case of general FF's.

For the FF of a parton into a  $D$  meson the following ansatz is used [35]:

$$D_i^D(x, \mu) = D_i^c(x, \mu) \otimes D_{np}^D(x). \quad (2.13)$$

The first term on the right hand side of 2.13,  $D_i^c(x, \mu)$  is the perturbative FF for a massless parton to fragment, via a perturbative QCD cascade, into the massive charm quark  $c$ .  $D_{np}^D(x)$  on the other hand is a non-perturbative fragmentation function, describing the transition from the heavy quark to the  $D$  meson. From perturbative QCD the initial state conditions for the perturbative FF's at a scale  $\mu_0$  of the order of the charm quark mass  $m_c$  can be extracted ( $\mu_0 = m_c$ ):

$$D_c^c(x, \mu_0) = \delta(1-x) + \frac{\alpha_s(\mu_0)C_F}{2\pi} \times \left[ \frac{1+x^2}{1-x} (\ln(\frac{\mu_0^2}{m^2}) - 2\ln(1-x) - 1) \right], \quad (2.14)$$

$$D_g^c(x, \mu_0) = \frac{\alpha_s(\mu_0)F_F}{2\pi} [x^2 + (1-x)^2] \ln(\frac{\mu_0^2}{m^2}), \quad (2.15)$$

$$D_{q,\bar{q},\bar{c}}^c(x, \mu_0) = 0 \quad (2.16)$$

where  $c$  represents (here) the charm quark and  $g$  and  $q$  the gluon and light quarks, respectively ( $C_F = 4/3$ ,  $T_F = 1/2$ ). The absorption of the logarithmic terms referred to above is also visible in equations 2.14 and 2.15.

However, it is not at all clear that the PFF's give the correct description for the fragmentation of the charm quark into charmed hadrons, since the charm quark is only moderately heavy. Therefore, the Peterson fragmentation function [21] is usually considered as a better approximation for the FF's at the starting scale  $\mu_0$  [34].

The perturbative FF's, evolved up to any scale  $\mu$  via the DGLAP - equations, can be used to evaluate charm cross sections in the large  $p_\perp$  region ( $p_\perp \gg m_c$ ) [35]. Finally, the  $\gamma p$  cross section can be written schematically as:

$$\begin{aligned} d\sigma^{(\gamma p)} &= d\sigma_{direct}^{(\gamma p)} + d\sigma_{resolved}^{(\gamma p)} \\ &= \int f_i^{(p)} d\hat{\sigma}_{\gamma i \rightarrow k} D_k^D + \int f_i^{(p)} f_j^{(\gamma)} d\hat{\sigma}_{ij \rightarrow k} D_k^D. \end{aligned} \quad (2.17)$$

In this expression, the  $f_i^{(p)}$  and  $f_j^{(\gamma)}$  terms are the PDF's as described in equation 2.7 in the massive scheme.

### 2.4.2 Differential distributions

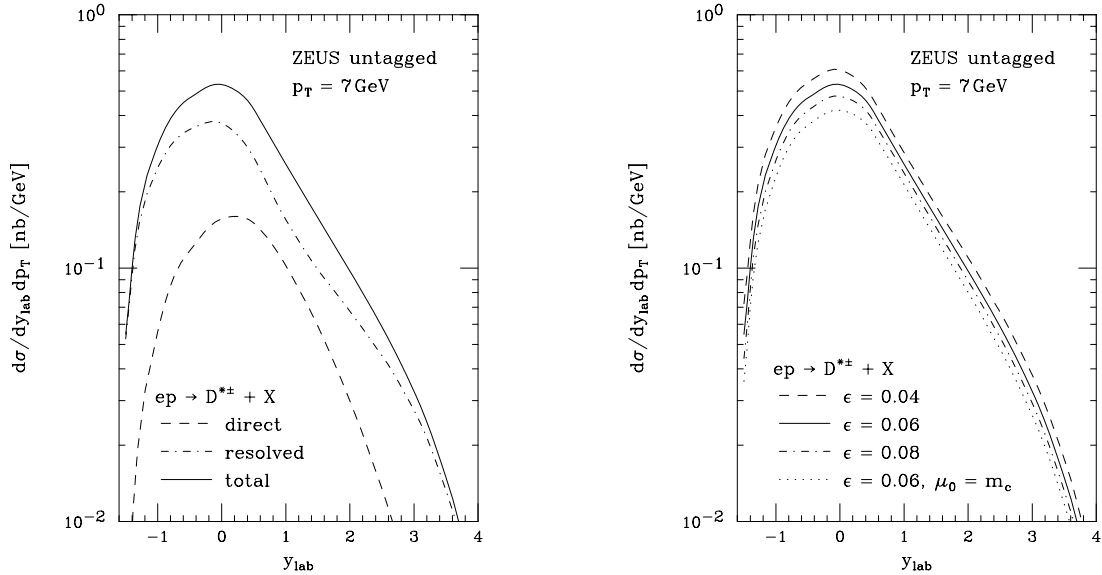


Figure 2.11: Rapidity dependence of the direct and resolved contributions to the charm cross section separately (left) and of their sum on the fragmentation parameter  $\epsilon_{Peterson}$  in the massless scheme [34].

To conclude the discussion of the massless approach representative distributions from calculations of inclusive  $D^{*\pm}$  cross sections [34] are shown in Figures 2.11, 2.12 and 2.13. The  $p_\perp$  and  $\hat{y}$  distributions refer to the kinematical conditions of the H1 and ZEUS experiment.

Whereas in the massive approach direct photoproduction dominates at large  $p_\perp$  over the resolved process, in the massless approach both contributions are of the same order of magnitude (Figure 2.11). Both cross sections peak at  $\hat{y} \approx 0$ , whereas in the direct approach the resolved contribution peaks at larger  $\hat{y}$  s. It should be stressed again that the decomposition of the photoproduction cross section in a direct and a resolved photon contribution is ambiguous at NLO, whereas the sum is

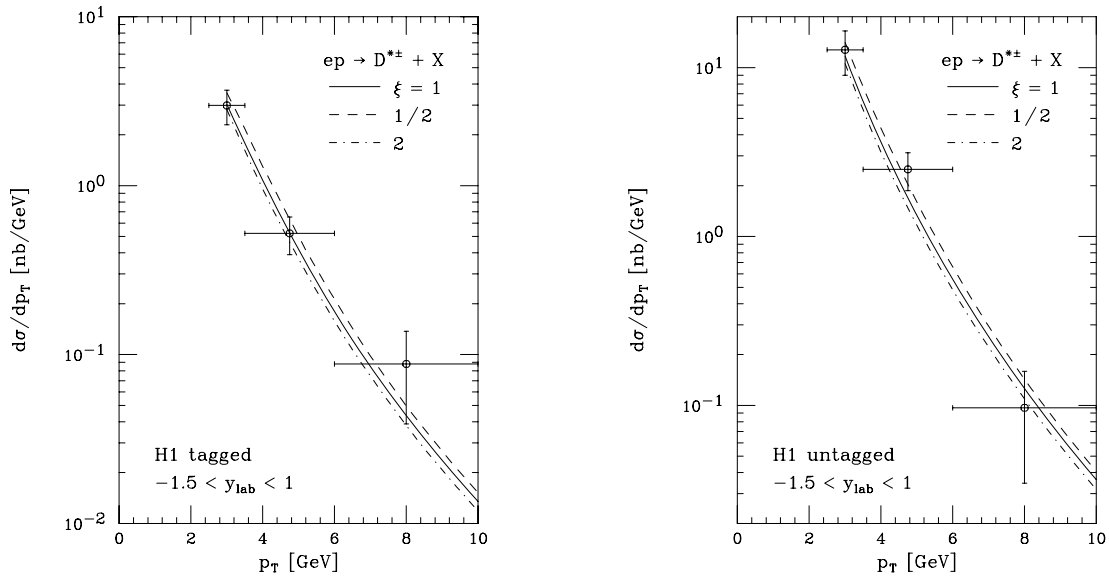


Figure 2.12: Cross sections in photoproduction ( $d\sigma/dp_{\perp}$ ) in the massless scheme [34].

unambiguously defined. Figure 2.11 also shows how variations in  $\mu_0$  and  $\epsilon$  affect the cross section. The standard choice of the renormalization and factorization scales is  $\mu = m_T = \sqrt{m_c^2 + p_{\perp}^2}$ . The evolution of the FF's starts at  $\mu_0 = 2m_c$ . If this value is reduced to  $\mu_0 = m_c$  keeping  $\epsilon = 0.06$ , the cross section decreases. This reduction can be compensated by adjusting  $\epsilon$  to a smaller value. Decreasing  $\epsilon$  leads to a larger cross section due to the harder fragmentation (see Figure 2.4).

In Figures 2.12 and 2.13, the massless NLO predictions are compared to earlier measurements of inclusive  $D^{*\pm}$  photoproduction cross sections (tagged and untagged) at HERA with the H1 detector. The respective experimental constraints are adopted in the calculations: tagged:  $Q_{max}^2 = 0.01 \text{ GeV}^2$ , untagged:  $Q_{max}^2 < 4 \text{ GeV}^2$ . The renormalization and factorization scales are chosen to be  $\mu = M_f/2 = \xi m_T$  and  $m_T = \sqrt{m_c^2 + p_{\perp}^2}$ . The scale dependence is small for the  $d\sigma/dp_{\perp}$  distribution ( $\mathcal{O}(10\%)$ ), indicating that corrections beyond NLO are likely to be small. The rapidity distributions  $d\sigma/d\hat{y}$  are more sensitive to the production mechanism and allow a more stringent test of the theory than  $d\sigma/dp_{\perp}$ .

The  $p_{\perp}$  distribution of the cross section is integrated over the rapidity interval  $-1.5 < \hat{y} < 1.0$ , the  $\hat{y}$  distribution over the transverse momentum interval  $2.5 \text{ GeV}/c < p_{\perp} < 10 \text{ GeV}/c$ . The agreement of data and theory is quite satisfactory in the  $p_{\perp}$ -spectra, even at small  $p_{\perp}$ . The theoretical prediction for tagged and untagged rapidity spectra are quite different, the tagged curve has its maximum at smaller  $\hat{y}$  (ca.  $\hat{y} \approx -1.2$ ), and shows a much stronger variation with  $\hat{y}$  than the untagged distribution ( $\hat{y}_{max} \approx -0.5$ ). The agreement of data and theory is less consistent than for the  $p_{\perp}$ -spectra. Due to the already large errors of these data, new measurements

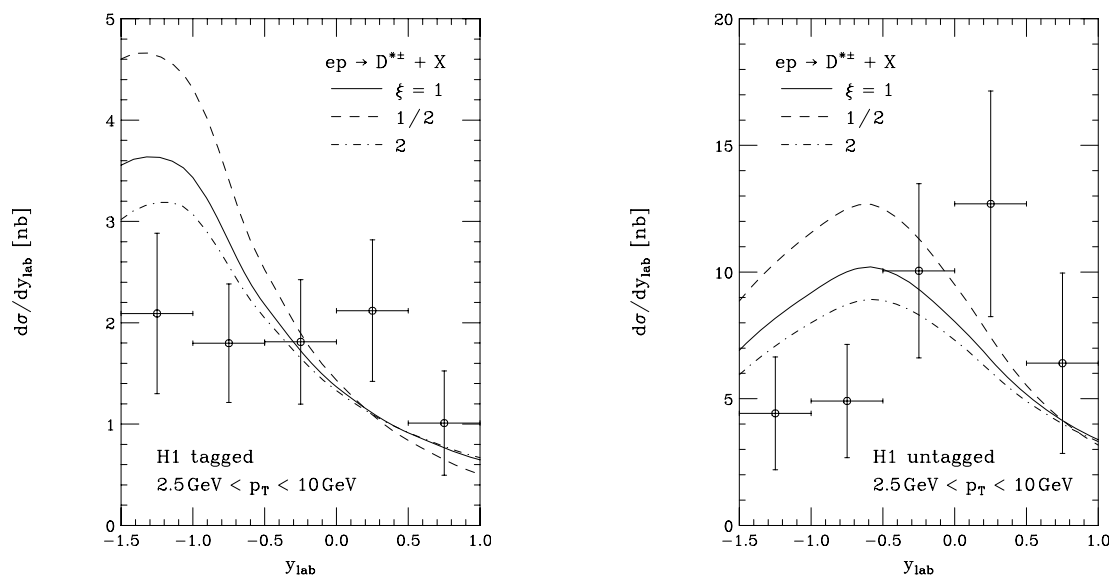


Figure 2.13: Cross sections in photoproduction ( $d\sigma/d\hat{y}$ ) in the massless scheme[34].

are needed.

## 2.5 Comparison of the massive and the massless approach

An older measurement of the tagged ( $Q^2 < 0.01 \text{ GeV}^2$ ) H1 data is compared in Figure 2.14 ([37, 72]) to predictions in NLO QCD with both the massive and the massless scheme. The massive calculation makes use of the PDF's MRSG and GRV-HO,  $m_c = 1.5 \text{ GeV}/c^2$  and two different values of  $\epsilon_{\text{Peterson}}$  ( $\epsilon = 0.02/0.06$ ), whereas the massless calculation uses the PDF's CTEQ4M and GRV-HO with an  $\epsilon$  value of 0.0674 ([34], [38]).  $\epsilon = 0.06$  does not give a satisfactory description of the data shape, whereas the choice of  $\epsilon = 0.02$  increases the overall normalization and enhances the forward region ( $\hat{y} > 0$ ) closer to the massless prediction. The question rises how much of the remaining discrepancy is due to the FF's and how much originates from higher order corrections.

In Table 2.1 we summarize schematically the two approaches again.

It is the aim of this analysis to test the QCD predictions by measuring the charm photoproduction cross section and to compare them to various QCD calculations and different proton and photon structure functions. To reach this goal a much bigger amount of data was analyzed than was available so far. This not only lowers the statistical errors and but also allows a first measurement of the double differential cross section  $d^2\sigma_{\gamma p}/d\hat{y}dp_{\perp}$ .

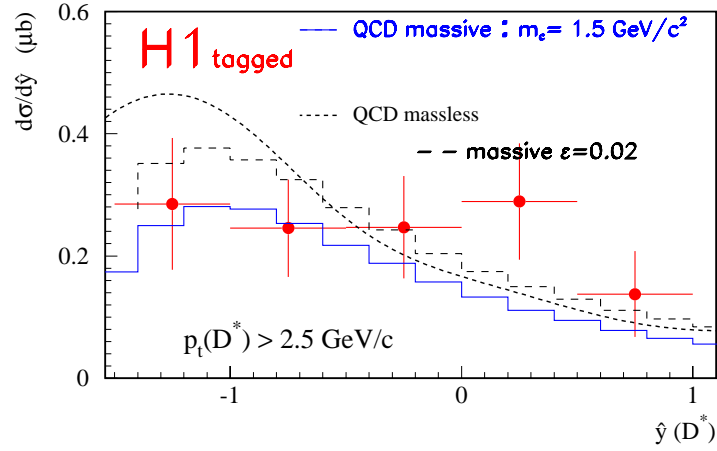


Figure 2.14: Charm cross sections in photoproduction ( $d\sigma/d\hat{y}$ ) of H1 tagged analysis of 1994. Comparisons are done to the massive and massless scheme. The massive NLO QCD calculation was done for  $m_c = 1.5 \text{ GeV}/c^2$  and  $\epsilon$ -Peterson = 0.06 and 0.02.

| massive scheme                                                                                                                                                                                                | massless scheme                                                                              |
|---------------------------------------------------------------------------------------------------------------------------------------------------------------------------------------------------------------|----------------------------------------------------------------------------------------------|
| $\gamma p \rightarrow c\bar{c} + X$                                                                                                                                                                           | $\gamma p \rightarrow c + X$<br>with $c \rightarrow D^{*\pm}$                                |
| $N_f = 3$ (massless) flavours in proton and photon PDF's, massive charm in final state                                                                                                                        | $N_f = 4$ massless flavours in initial and final state                                       |
| no collinear divergences and factorization in final state, no FF's necessary                                                                                                                                  | absorb final-state collinear divergences into FF's; resum large logs evolving PDF's and FF's |
| indispensable for $\sigma_{tot}$ and $d\sigma/dp_\perp$ at $p_\perp \lesssim m_c$ , breaks down for $p_\perp \gg m_c$ due to initial- and final-state collinear divergences in $\ln(\frac{p_\perp^2}{m_c^2})$ | indispensable for $p_\perp \gg m_c$ , breaks down for $p_\perp \lesssim m_c$                 |

Table 2.1: Comparison of massive and massless scheme, survey of the most important points discussed in this chapter.

# Chapter 3

## HERA and the H1-experiment

The storage ring system HERA at the DESY laboratory (Deutsches Elektronen Synchrotron) in Hamburg (Germany) is a facility to accelerate and store leptonic and hadronic beams. The HERA project was approved in 1984 and the first  $ep$  collisions were observed in autumn 1991. The collider experiments H1 and ZEUS started with their data taking programs in 1992. Apart from H1 and ZEUS, two other experiments make use of the HERA beams: HERMES (data taking since 1995) and HERA-B (start 1998).

A brief overview of HERA and the experimental setup of H1 is given in this chapter. The main detector components of H1 are described with regard to the analysis presented here. Finally some long term performance studies for the innermost central  $z$  drift and proportional chambers (CIZ and CIP) are shown.

### 3.1 The HERA ring

A schematic overview of the HERA tunnel [12]<sup>1</sup> and the preaccelerators is given in Figure 3.1. Due to the different properties of lepton and hadron beams, HERA consists of two independent accelerators for electrons<sup>2</sup> (HERA-e) and protons (HERA-p) with a total circumference of 6.4 km. The beam energies of 820 GeV for HERA-p and 27.5 GeV for HERA-e lead to a center of mass energy  $\sqrt{s} \approx 300$  GeV. This is one order of magnitude larger than the energies achieved so far in fixed target lepton-nucleon scattering experiments. To reach the same center of mass energy in a fixed target experiment, the electron beam has to be accelerated up to 52000 GeV, as was already mentioned in section 1.2.

Electrons (or positrons resp.) are produced in the linear accelerator LINAC II and injected into DESY II with an energy of 450 MeV. After accelerating them to 7.5 GeV, they are transferred to PETRA II, where they reach the injection energy

---

<sup>1</sup>HERA: **H**adron **E**lectron **R**ing **A**ccelerator.

<sup>2</sup>In summer 1994 the operation of the electron ring was changed to positrons. Furthermore the word electron stands for positrons as well.

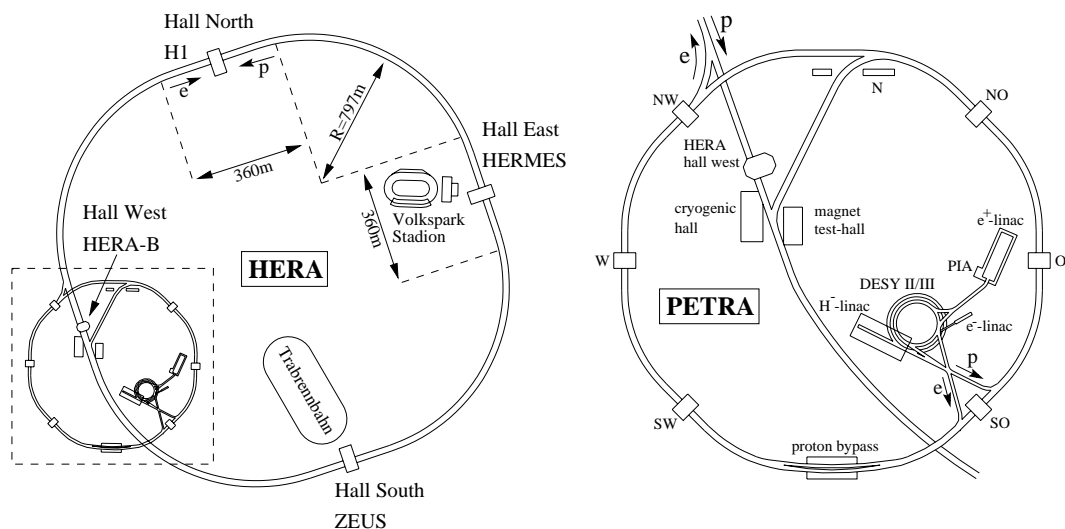


Figure 3.1: *The storage ring HERA and the preaccelerators at DESY*

of 12 GeV for HERA-e. Protons take a similar way, starting as negative charged hydrogen ( $H^-$ ) in LINAC III with an energy of 50 MeV. They are sent through a stripper foil, so that they lose the electrons, and are injected to DESY III as bare protons. The injection energy for PETRA II is 7.5 GeV and for HERA-p 40 GeV, respectively. The beams are filled into HERA and accelerated separately. If they have reached their final energy frontal collisions are tuned in the interaction regions of H1 and ZEUS. The life time of the proton beam is much longer than 24 hours ( $\sim 100$  h), the electron beam is gone after 12 hours.

Synchrotron radiation of the electron beam increases strongly with the beam energy and causes large beam energy losses, which is one of the limiting factors of HERA. On the other hand high energetic protons need magnets of large strength to bend them towards the orbit. HERA-p consists of superconducting magnets producing a magnetic field of 4.6 T.

The electron and proton beams are packed into 210 bunches with a short bunch crossing interval of 96 ns (10.4 MHz). 180 bunches were filled in 1996 with  $10^{10} - 10^{11}$  particles in each bunch. The radial extension at the interaction point is  $\sigma_x = 0.29(0.27)$  mm and  $\sigma_y = 0.07(0.02)$  mm for protons (electrons). The longitudinal extension, giving the length of the interaction zone, is  $\sigma_z = 110(8)$  mm.

To study background conditions some bunches from both beams have no collision partner (pilot bunches). Background originates from interactions of the beams with rest gas molecules in the beam pipe or with the beam pipe itself or from synchrotron radiation. The proton or electron induced background can then be studied separately. The total beam current has been increased from year to year, in 1996  $I_e \approx 40$  mA and  $I_p \approx 90$  mA were reached. The luminosity produced in the years 1992 up to 1997 is shown in Figure 3.2. The rise of beam currents and HERA performance during the last years is obvious.

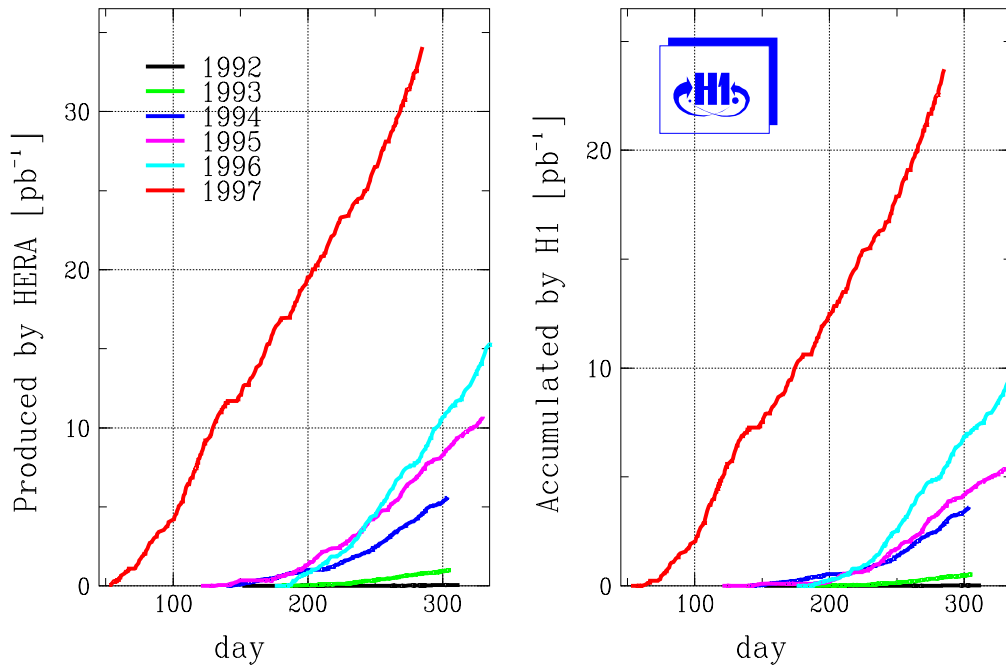


Figure 3.2: *The integrated luminosity produced by HERA and measured in H1 for the years 1992 -1997*

At HERA there are four interaction regions. Two of them are occupied with the collider experiments ZEUS [40] and H1 [39]. The HERMES [42] experiment studies the spin structure of the nucleon, scattering the polarized electron beam off polarized gas targets. To measure the CP violation in systems of  $B$  mesons, produced by scattering of beam halo protons off a wire target, the experiment HERA-B [41] was designed.

## 3.2 The experiment H1

Due to the different beam energies of HERA the  $ep$  system in the detector is strongly boosted along the proton direction. The layout of the H1 detector takes this into account: the forward direction<sup>3</sup> is more massive and instrumented with higher granularity.

A schematic overview of the H1 detector is given in Figure 3.3. The beam pipe [1]<sup>4</sup> is surrounded by the tracking system, consisting of the central tracker [2] and the forward tracker [3]. The central tracker is described in more detail in section 3.2.1. In the cryostat [15] the liquid argon calorimeter is placed enclosing the tracking system, divided into an electromagnetic [4] and a hadronic part [5]. The tracking system and the calorimeter are surrounded by a super conducting solenoid [6], producing a magnetic field parallel to the  $z$ -axis of 1.2 T. The iron return yoke [10] of the magnetic field is instrumented with streamer tubes. Additional muon chambers enable an identification and track recognition of muons. Hadronic showers leaking out of the calorimeter are measured in the instrumented iron as well. High energetic muons boosted in forward direction are registered in the forward muon system, consisting of a toroid magnet [11] and muon drift chambers [9]. The liquid argon calorimeter is complemented in the forward direction by a copper/silicon calorimeter (Plug) [13] and in the backward region by a scintillating fiber calorimeter SPACAL [12]. The SPACAL calorimeter is divided also into an electromagnetic and hadronic part (see also Figure 3.4). The backward drift chamber (BDC) is installed at the inner side of the electromagnetic SPACAL. There are some further detectors in the HERA tunnel. The luminosity system is located in electron beam direction, composed of the electron detector at  $-33$  m and the photon detector at  $-103$  m. The proton remnant detector is located in proton beam direction.

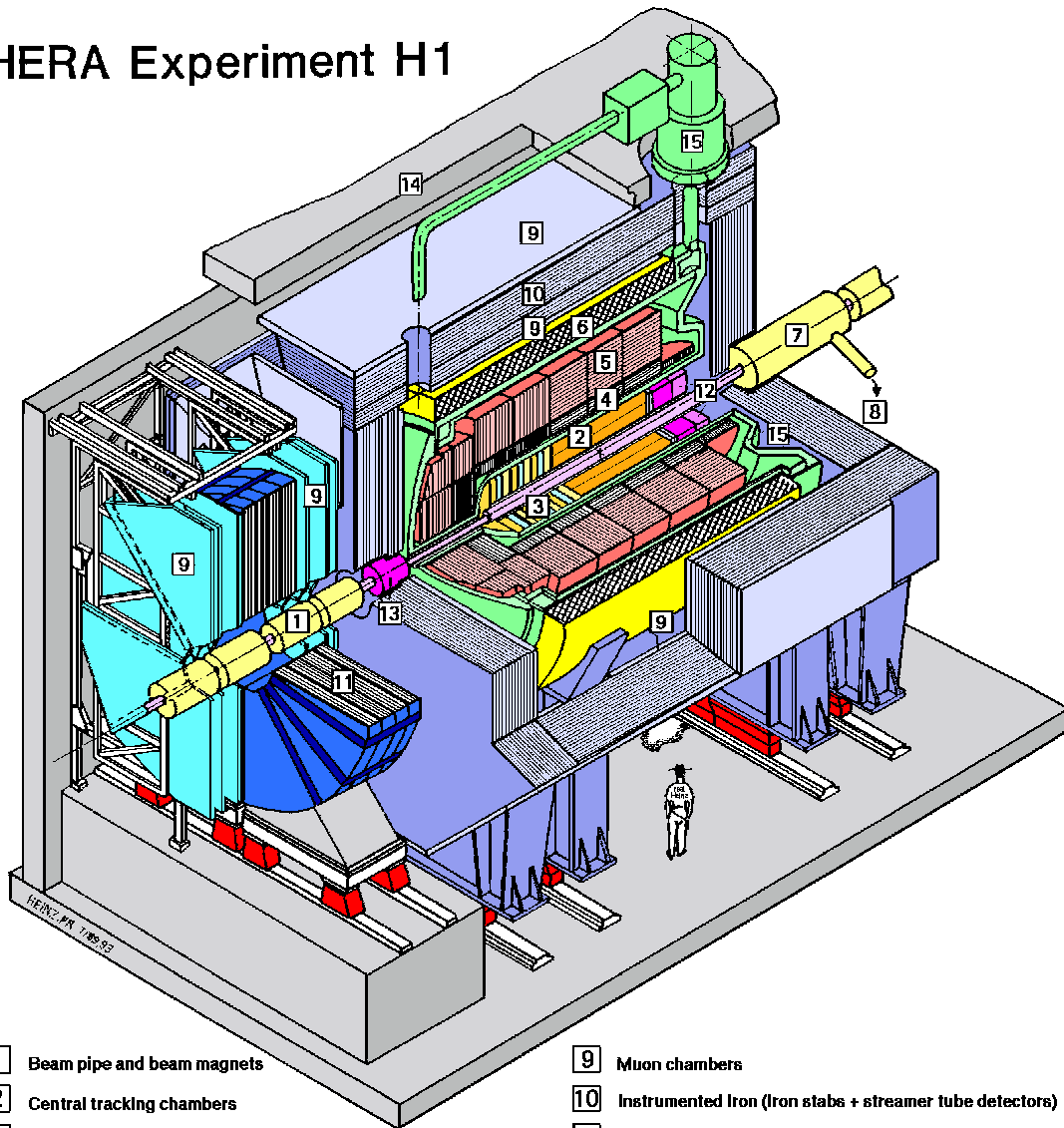
In the following section the detector components needed for the analysis presented in this thesis are described in more detail. A complete description of the H1 detector is given in [39].

---

<sup>3</sup>The H1 coordinate system is a right handed system. The  $\hat{z}$ -direction is given by the proton beam direction,  $\hat{x}$  points to the center of the HERA ring,  $\hat{y}$  denotes the vertical direction and the origin is chosen at the nominal interaction point. The  $+\hat{z}$  direction is then called the forward direction, this corresponds to polar angles  $\vartheta < 90^\circ$ .

<sup>4</sup>The numbers correspond to the numbers in Figure 3.3.

## HERA Experiment H1



- |   |                                           |    |                                                          |
|---|-------------------------------------------|----|----------------------------------------------------------|
| 1 | Beam pipe and beam magnets                | 9  | Muon chambers                                            |
| 2 | Central tracking chambers                 | 10 | Instrumented Iron (Iron slabs + streamer tube detectors) |
| 3 | Forward tracking and Transition radiators | 11 | Muon toroid magnet                                       |
| 4 | Electromagnetic Calorimeter (lead)        | 12 | Warm electromagnetic calorimeter                         |
| 5 | Hadronic Calorimeter (stainless steel)    | 13 | Plug calorimeter (Cu, Si)                                |
| 6 | Superconducting coil (1.2T)               | 14 | Concrete shielding                                       |
| 7 | Compensating magnet                       | 15 | Liquid Argon cryostat                                    |
| 8 | Helium cryogenics                         |    |                                                          |
- } Liquid Argon

Figure 3.3: The H1 detector at HERA. The size of the detector is  $12\text{ m} \times 10\text{ m} \times 15\text{ m}$  and its total weight is ca 2800 t. The protons enter from the right hand side, the electrons from the left.

### 3.2.1 The tracking system

The task of the tracking system is, on one hand, to identify and to reconstruct charged particle tracks with high precision, on the other hand to deliver trigger signals for the online event selection using the H1 trigger system. The tracking system is divided into two independent parts according to the boosted event kinematics. The forward tracking device (**FTD**) covers a  $\vartheta$  region of  $7^\circ < \vartheta < 25^\circ$  and is optimized for tracks with small polar angles in the forward direction. The FTD was not used for this analysis. The main part is the central tracking device (**CTD**) covering a polar angle region around the interaction point of  $20^\circ < \vartheta < 160^\circ$ . The whole tracking system is shown in Figure 3.4.

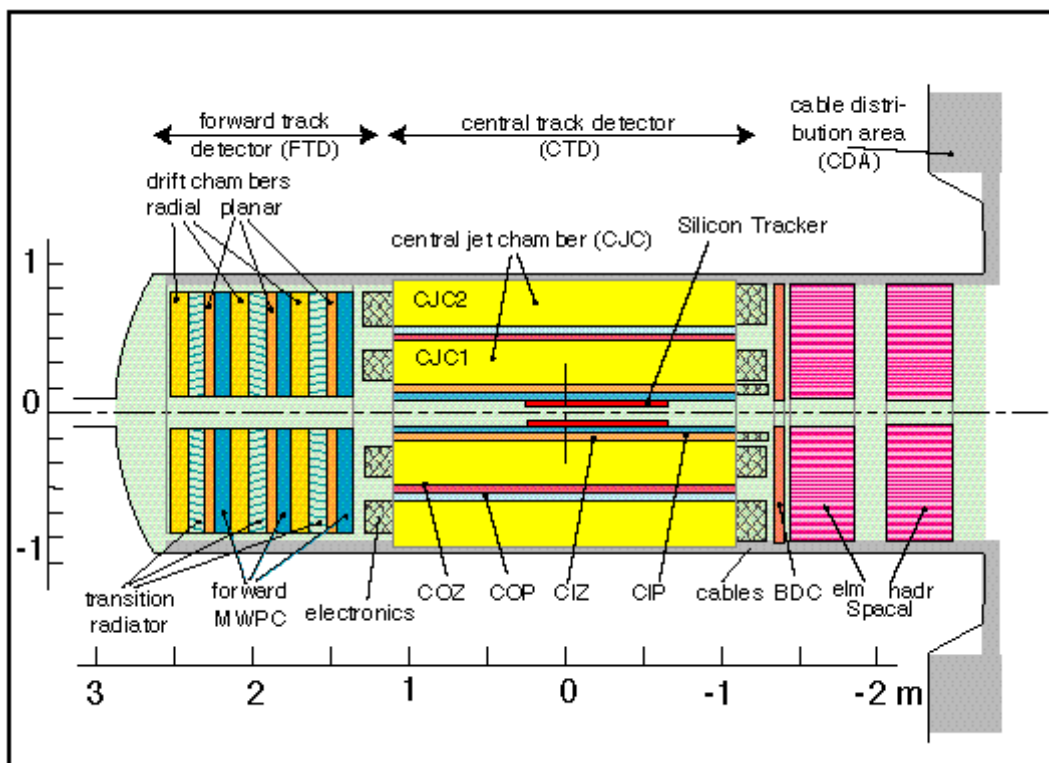


Figure 3.4: *The H1 tracking system: schematic overview in rz*

The central tracker consists out of 6 concentricly arranged cylindrical chambers. A radial overview is given in Figure 3.5.

#### Central Jet Chamber CJC

The track reconstruction in the central region of H1 is based on two large independent drift chambers (CJC1 and CJC2 [43]). The chambers have wires strung parallel to the beam axis ( $z$ -direction) and the drift cells inclined about  $30^\circ$  with respect to the radial direction. The inner chamber is divided in 30 cells with 24

layers of signal wires each, the outer chamber has 60 cells with 32 layers of signal wires. The active length in  $z$  is 220 cm, in the radial direction 22.4 cm for CJC1 and 29.6 cm for CJC2 respectively.

The cells are limited by cathode wire planes and field forming wires close to the signal wires, forming a drift field orthogonal to the signal wire plane (see Figure 3.5). Due to the presence of a magnetic field, the ionization electrons do not drift anymore parallel to the drift field. The Lorentz force causes a constant angle between the drift direction and the drift field lines, called the *Lorentz angle*. The tilt of the cells compensates this effect, the ionization electrons drift perpendicularly to tracks of high energetic particles. Furthermore, the particles cross several layers of signal wires or drift cells. Ambiguities, caused by the impossible distinction of track and mirror track, can be resolved. Mirror tracks have no continuation in the neighboring cell.

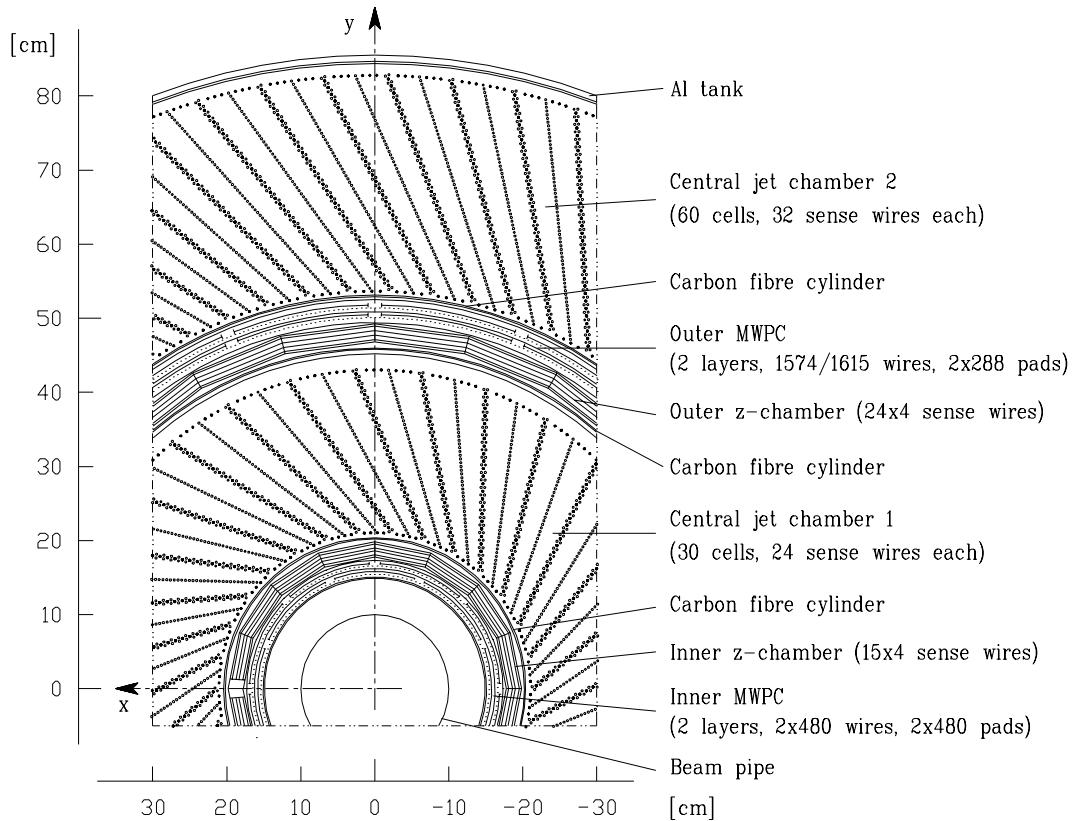


Figure 3.5: *The H1 central tracing system: schematic overview in  $r\varphi$*

The spatial resolution in the  $r\varphi$ -plane was measured as  $\sigma_{r\varphi} = 170\mu\text{m}$ . The signal wires are read out at both ends. The  $z$ -component can be measured in the CJC using charge division [44]. The resolution in  $z$  is worse than in  $r\varphi$  and was determined as  $\sigma_z = 22\text{ mm}$ . In practice the measurement of the  $z$ -coordinate is mainly done by the  $z$ -drift chambers CIZ and COZ.

### Central Inner/Outer $z$ -Driftchambers CIZ/COZ

The  $z$  coordinate is measured with better accuracy with two thin drift chambers, the central inner (CIZ [45, 46]) and central outer (COZ [48])  $z$ -drift chambers than with charge division in CJC. The CIZ fits into the space of the inner cylinder of CJC1, and COZ is installed between CJC1 and CJC2. The  $z$  measurement with satisfactory resolution in  $z$  ( $\sigma_z \approx 300\mu\text{m}$ ) requires a drift direction parallel, and sense wires perpendicular, to the beam axis. This is realized by the modular construction method of the chambers: rings with four signal wires each are arranged along the beam axis. The CIZ consists out of 15, the COZ out of 24 similar rings.

The sense wire planes of CIZ are tilted by  $45^\circ$  with respect to the radial direction. The first nine cells in the backward region ( $-z$  region) are tilted backward, changing the orientation at the interaction point for the last 6 rings in forward direction ( $+z$  region), corresponding to the orientation of the tracks crossing the respective cells. The orientation of the sense wire planes of COZ is normal to the beam axis.

By combining the information of both chamber types (CJC and  $z$ -chambers), a good spatial resolution in  $r\varphi$  as well as in  $z$  can be achieved and therefore a good track reconstruction is possible. The schematic overview is given in Figures 3.4 and 3.5.

### Central Inner/Outer Proportional Chambers CIP/COP

The central multiwire proportional chambers (CIP/COP, [49]) are cylindrical double layer chambers, situated around the beam axis. The inner one (CIP) is closest to the beam pipe and covers a polar angle of  $8^\circ < \vartheta < 172^\circ$ , its outer partner fits in between COZ and CJC2 (see Figure 3.5). The cathodes, used for a fast read out, consist of pads segmented in  $z$  and  $\varphi$ . The layers of CIP are 60-fold segmented in  $z$  and 8-fold in  $\varphi$ . The inner chamber is rotated by  $22.5^\circ$  with respect to the outer chamber to achieve an effective 16-fold segmentation. Both layers of COP are constructed in the same way as CIP. Differences occur in pad size and radius: the layers of COP are 16-fold segmented in  $\varphi$  and 18-fold in  $z$ .

A fast timing signal with pad information, with a better timing resolution than the HERA bunch crossing distance of 96 ns, is delivered by the proportional chambers. The signals are used for trigger purpose to deliver a fast first level trigger (L1) decision. A four-fold coincidence out of pads of both double layers systems leads to a first estimation of the  $z$  position of the vertex. Furthermore a minimal transverse momentum of 70 MeV/c is needed by particles to reach the outer chamber. The direction and the point of intersection with the  $z$  axis of the particle can be estimated approximately. The impact point in  $z$  enters in a 16 bin histogram around the nominal interaction point ( $z = \pm 44\text{cm}$ ). For genuine  $ep$  events, a significant peak near to the event vertex is expected in the distribution of intersection points.

### 3.2.2 The luminosity system

The luminosity system of H1 is located downstream in the direction of the electron beam in the HERA tunnel as is shown in Figure 3.6. The system consists of two detectors: the electron tagger (ET) at  $-33$  m and the photon detector (PD) at  $-103$  m. The measurement of luminosity is done with the Bethe-Heitler process  $ep \rightarrow ep\gamma$ , its cross section is well known in QED and insensitive to an internal proton structure [50]. A simultaneous detection of  $e$  and  $\gamma$  in ET and PD in the final state is required.

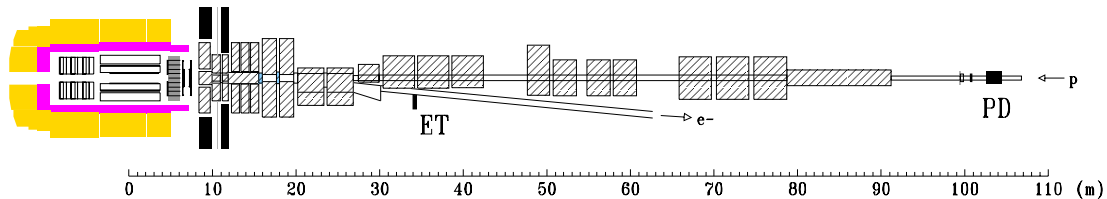


Figure 3.6: *The H1 luminosity system: the Electron tagger is located at 33 m behind the interaction point.*

The main source of background is bremsstrahlung from the residual gas ( $eA \rightarrow eA\gamma$ ) in the beam pipe. These events are expected at 10 % of the  $ep \rightarrow ep\gamma$  rate [51], and can be subtracted using data from electron pilot bunches. The luminosity is given by

$$L = \frac{R_{tot} - (I_{tot}/I_0)R_0}{\sigma_{vis}} \quad (3.1)$$

where  $R_{tot}$  is the total rate of the bremsstrahlung events,  $R_0$  is the rate for electron pilot bunches,  $I_{tot}/I_0$  the ratio of the corresponding beam currents and  $\sigma_{vis}$  the visible part of the Bethe-Heitler cross section. The precision of the H1 luminosity measurement in 1995 was 1.07 %, in 1994 1.4 % [51]

#### The electron tagger

The Electron Tagger (ET) is also used to register the scattered electron in photoproduction events. To hit the ET the polar angle of the scattered electron must be smaller than 5 mrad ( $180^\circ - \vartheta_e < 5$  mrad) and the energy  $E'_e$  within the region of  $5.5 \text{ GeV} < E'_e < 22 \text{ GeV}$ . This corresponds to squared momentum transfer  $Q^2 < 0.01 \text{ GeV}^2/c^2$ . The acceptance  $\mathcal{A}(y, Q^2)$  depends on the kinematical variables  $y$  and  $Q^2$  and the position of the electron beam as can be seen in Figure 4.6. The acceptance correction is measured by the Bethe-Heitler process with an accuracy of 3 % [52] and is discussed in detail in section 4.4.1.

### 3.2.3 The trigger system

Due to the small cross sections of  $ep$  physics, large beam current and a high bunch crossing rate (10.4 MHz) is needed, as was claimed above in section 3.1. This

leads to huge background rates, which consist of synchrotron radiation from the electron beam, proton gas interactions in the beam pipe vacuum, stray protons, which produce particle showers hitting the beam pipe walls and cosmic muons. The total rate of background events is about a factor 1000 higher than genuine  $ep$  interaction events. The variety of physics processes covers a wide range of rates. It extends from photoproduction, where the visible  $ep$  cross section of several  $\mu\text{b}$  implies an event rate of 20-30  $\text{Hz}^5$  towards  $W$  production where a few events per week are expected. On the other hand, the expected rate for beam gas interaction is about 50 kHz [39].

It is the aim of the central trigger logic (CTL) to decide with low dead time, if an event should be kept or not. At H1 a four level pipelined trigger concept is realized. The information from all detector parts can principally contribute to the trigger decision. Therefore the individual data are stored into pipelines with necessary length (min. 25 bunch crossings or 24  $\mu\text{s}$ ). A schematic overview of the four levels of the trigger system is given in Figure 3.7.

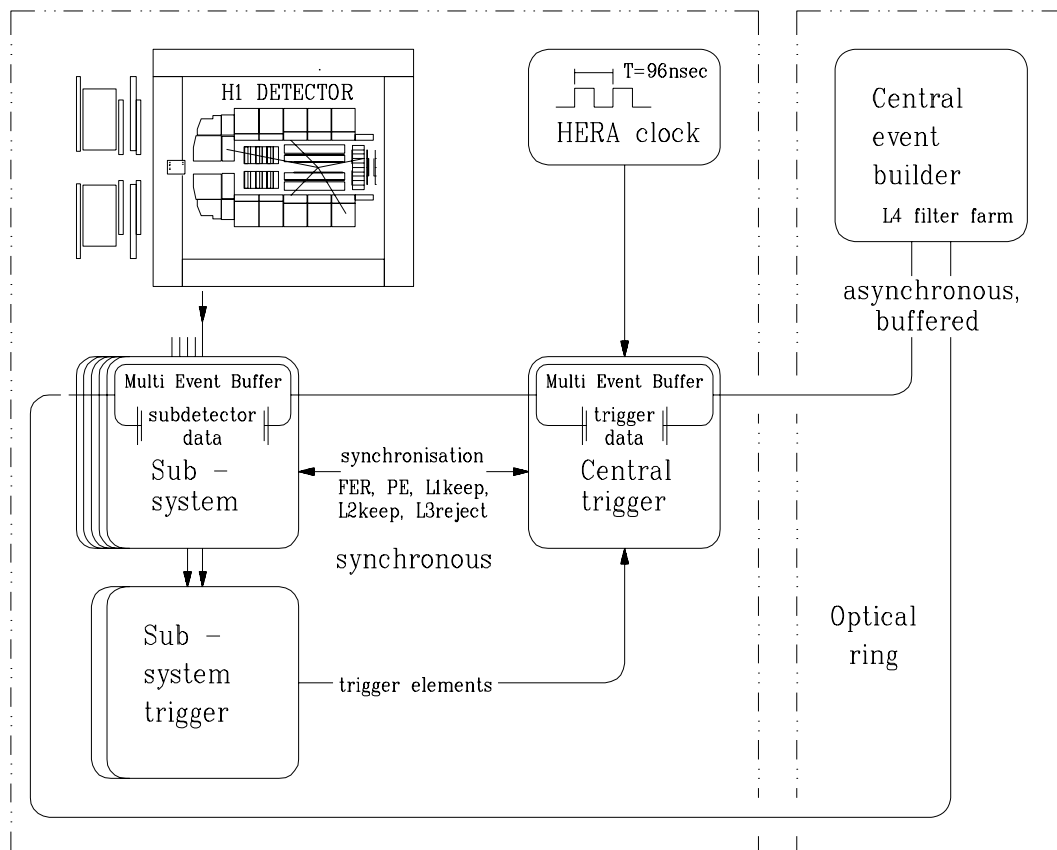


Figure 3.7: *The H1 trigger system: schematic overview.*

<sup>5</sup>All values are given for design luminosity of  $\mathcal{L} = 1.5 \cdot 10^{-31} \text{ cm}^2\text{s}^{-1}$ .

### First level trigger

The first level trigger ( $L1$ ) runs completely dead time free due to the pipelined architecture of its readout system. All detector subsystems deliver a set of *trigger elements* (TE) representing some characteristic signals of the corresponding detector component. In the CTL the TE are logically combined to generate a  $L1$  trigger signal. Up to 128 different *subtriggers* (ST) are formed by applying suitable coincidences and threshold requirements. If any of the ST is set, the  $L1 - keep$  signal will be sent, and the front end pipelines are held for read out their data. If all subsystems are read out, the recording of detector data can be restarted. The decision time of  $L1$  takes ca.  $24 \mu s$ , the acceptance rate is about 50 Hz.

### Second and third level trigger

Dead time starts with the readout process. The level 2 trigger ( $L2$ ) evaluates more complex decisions based on combined information using neuronal networks and topological triggers. The decision is delivered after  $20 \mu s$  and the data taking restarts immediately if it is negative.

The third level trigger has been implemented, but has not yet been used for any decision.

### Fourth level trigger

The fourth level trigger ( $L4$ ) is an asynchronous software trigger based on a farm of fast processor boards. It is integrated into the central data acquisition and has the full event information available as opposed to the trigger levels before. A fast version of the H1-reconstruction program makes more detailed information accessible.

It is the purpose of the  $L4$ -trigger to verify the  $L1$  trigger decision, to identify background events and to classify good events into different event classes motivated by physics analysis. The trigger verification checks all conditions of the chosen trigger elements, i. e. for events with track triggers the presence of real measured tracks is checked. Background events can partially be rejected by a simple cut on the reconstructed vertex. Its position must lie within the nominal interaction zone. If a background event has its origin in the background region, a cut on the longitudinal energy flow<sup>6</sup> and the inelasticity  $y_{JB}$ <sup>7</sup>. might help.

The physics output of  $ep$  collisions is very rich and covers a huge range of possible analyses. To facilitate the analysis, event classes are defined, according to the physics aspects of HERA/H1. The event classification routine is running first on  $L4$ , and assigns every event to one or more event classes. For heavy quark events for example, a routine  $HQSEL$  has been written, which preselects heavy quark events based on track information. All events, which were selected by  $HQSEL$  and triggered by

---

<sup>6</sup>The longitudinal energy flow  $\sum p_z / \sum p$  is expected to be large for background events ( $\approx 1$ ).

<sup>7</sup>The inelasticity of Jacquet-Blondel  $y_{yb}$  is very small for background events ( $\approx 0$ ).

certain heavy quark specific triggers, were kept after the trigger verification. The routine *HQSEL* is explained in more detail in chapter 4.2.2.

The online monitoring of the performance of all detector and trigger systems is also done on *L4*. For monitoring reasons, 1 % of all *L4*-rejected events is nevertheless written to tape.

### Fifth level trigger

*L5* is the final event offline reconstruction at the DESY computing center. If an event is kept by the filter farm *L4*, the raw data are sent to the DESY computing center and written to tape. After several complex steps of reconstruction, e.g. track finding, calorimetry cluster finding, applying calibration constants and jet finding, the data are ready for analysis. At the reconstruction step, the event classification is done once more, this time using the full version of the reconstruction program and allowing multiply class assignments. For the heavy flavour quark selection the same routine is used as on *L4*. Only a few events are rejected at *L5*.

## 3.3 Performance of the inner z-drift chamber CIZ

The central inner *z*-drift chamber CIZ (chapter 3.2.1) is one of the innermost chambers of the H1-detector and therefore very sensitive to the beam and background conditions. On one hand, the CIZ can be used for beam optimizations but on the other hand the high radiation activity in the central region of the detector causes ageing. The chamber was operated in the running periods 1995 to 1997 under stable conditions and has not been opened during this time. Ageing effects can therefore be well observed. Performance studies of CIZ and details of the construction have been previously reported in [47, 53].

### Hardware outline

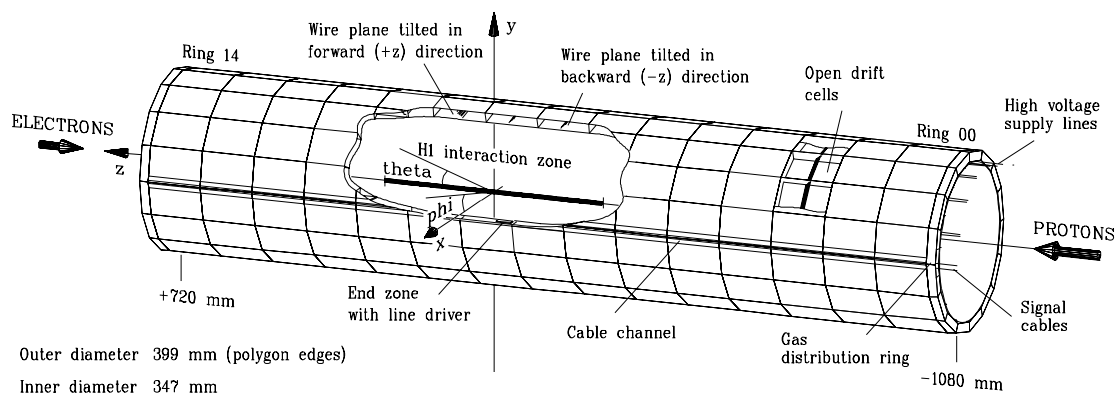
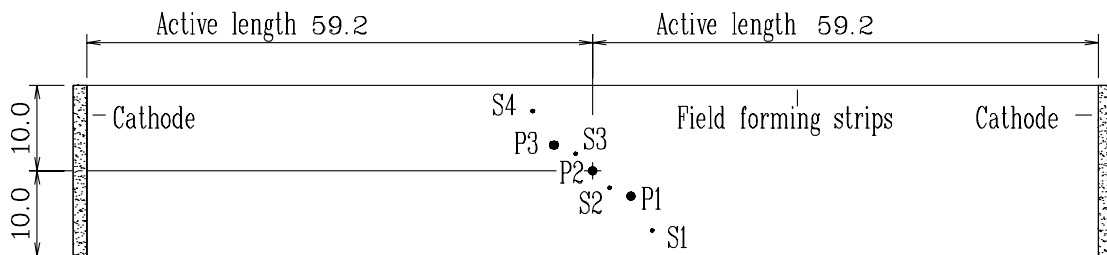


Figure 3.8: Outline of the central inner *z*-drift chamber CIZ

A general outline of the H1 tracking system was given in Figures 3.4 and 3.5. The CIZ chamber consists of 15 independent rings, each divided in 16 drift cells arranged on a regular polygon (see Figure 3.8 for the chamber layout and Figure 3.9 for the drift cell layout). Three field forming wires (potential wires, P1 - P3 in Figure 3.9) and four anode wires (signal wires, S1 - S4 in Figure 3.9) are running around the ring. The rings are electrically independent and the walls of the drift cells act as support for the cathode strips.

A dedicated current monitoring system [54] is used to measure the currents of the signal wires, in the range of a few nA. The signal wires control the gas amplification in the chamber. The measured current of the signal wires  $I_{SW}$  provides a very sensitive monitoring of the beam condition and of the performance of the chamber.

Since the wire planes are tilted by  $45^\circ$ , the drift field configuration is such, that the two outer wires (S1 and S2 in Figure 3.9) collect charge only from one side of the drift cell, i. e. that, where the distance to the cell division is shorter<sup>8</sup>. The collected charge in this case is higher than the charge arriving at the inner wires, because corresponding drift field region is wider. This solves the left - right ambiguity in the drift time distribution.



Wire positions [mm]

|                       |            |            |                   |            |            |
|-----------------------|------------|------------|-------------------|------------|------------|
| Potential wire 1 (P1) | $z = 4.5$  | $y = -3.0$ | Anode wire 1 (S1) | $z = 7.0$  | $y = -7.0$ |
| Potential wire 2 (P2) | $z = 0.0$  | $y = 0.0$  | Anode wire 2 (S2) | $z = 2.0$  | $y = -2.0$ |
| Potential wire 3 (P3) | $z = -4.5$ | $y = 3.0$  | Anode wire 3 (S3) | $z = -2.0$ | $y = 2.0$  |
|                       |            |            | Anode wire 4 (S4) | $z = -7.0$ | $y = 7.0$  |

Wire diameters

|                 |                   |             |                  |
|-----------------|-------------------|-------------|------------------|
| Potential wires | $120 \mu\text{m}$ | Anode wires | $20 \mu\text{m}$ |
|-----------------|-------------------|-------------|------------------|

Figure 3.9: Outline of the drift cell of the central inner z - drift chamber CIZ

## Calibration

The final measurement of  $z$  of the track depends on a number of calibration constants and parameters, including also geometrical constants. There are other parameters which depend on the running conditions of the drift chamber, e. g. the drift velocity

<sup>8</sup>This is the case for the left hand side of wire S4 and for the right hand side of wire S1.

$v_D$  depends on the applied electric field as well as the magnetic field. Finally the readout and signal electronics influence the determination of time and charge. The drift time  $t_D$  needed to calculate the  $z$ -position has to be corrected for all known offsets.

$$t_D = t_M - t_0^{offset} - t_0^{wire} \quad (3.2)$$

Here  $t_M$  is the measured time,  $t_0^{wire}$  the wire by wire offset and  $t_0^{offset}$  the global time offset determined by the global delays in the readout system. Space points corresponding to given fixed values of drift time are listed in the isochrone map. The drift length is therefore extracted from the isochrone map, nevertheless a linear correction factor  $c_{scale}$  is used for a precise adjustment to the actual drift velocity:

$$v_D = \frac{1}{c_{scale}} \cdot v_{norm}; \quad \text{where} \quad v_{norm} = 50 \frac{\text{mm}}{\mu\text{s}} \quad (3.3)$$

The most crucial parameters ( $t_0^{offset}$  and  $v_D$  (resp.  $c_{scale}$ )) have to be determined regularly. A detailed description of the calibration of the other parameters can be found in [47].

Cosmic data are used to determine  $v_D$  and  $t_0^{offset}$ . A clean cosmic event, which penetrates the central tracker near the beam axis, produces signals in all devices of the central tracker. The event reconstruction in the jet chamber (CJC) recognizes it as two tracks coming from a common vertex. The linking procedure fits the CJC-track using the more accurate  $z$ -information from the  $z$ -chambers. The cosmic ray track sections above and below the beam axis can be fitted to one straight line in the  $(z, s)$  plane, where  $z$  is the coordinate along the beam axis and  $s$  the arclength. For the calibration fit, the combined track information of CJC and  $z$ -chambers is only used for the track selection. The calibration fit itself is performed with the raw data information of both  $z$ -chambers only.

In the magnetic field the particles travel along a helix in space, in the  $(x, y)$  projection the track appears as a circle of radius  $\rho = \kappa^{-1}$ , while in the  $(z, s)$  projection, it appears as a straight line. The arclength at a point  $(x_i, y_i)$  can be calculated as follows:

$$s_i = \rho \cdot \arccos\left(\frac{\rho^2 + d^2 - r_i^2}{2\rho \cdot d}\right) \quad ; \quad \text{where} \quad r_i = \sqrt{x_i^2 + y_i^2} \quad (3.4)$$

where  $d = \rho - r_0 \text{sign}(\kappa)$  and  $r_0$  is the distance of closest approach to the  $z$  axis. Using the  $(z_i, r_i)$  pairs for the correlated  $z$ -chamber hits, we use the CJC information to convert them to  $(z_i, s_i)$  pairs in the  $(z, s)$  plane. The parameters  $\kappa$  and  $r_0$  are taken from the CJC track. The points should then fall on a line

$$z = \alpha \cdot s + \beta. \quad (3.5)$$

For the two sections of the track the sign of  $s_i$  is reverted for the fit of a straight line with  $n$  points, each of which is measured with an error  $\sigma_i = \delta z_i$ , which yields  $\alpha$  and  $\beta$ . In a fit step the COZ can be used to calibrate the CIZ. Fitting the tracks

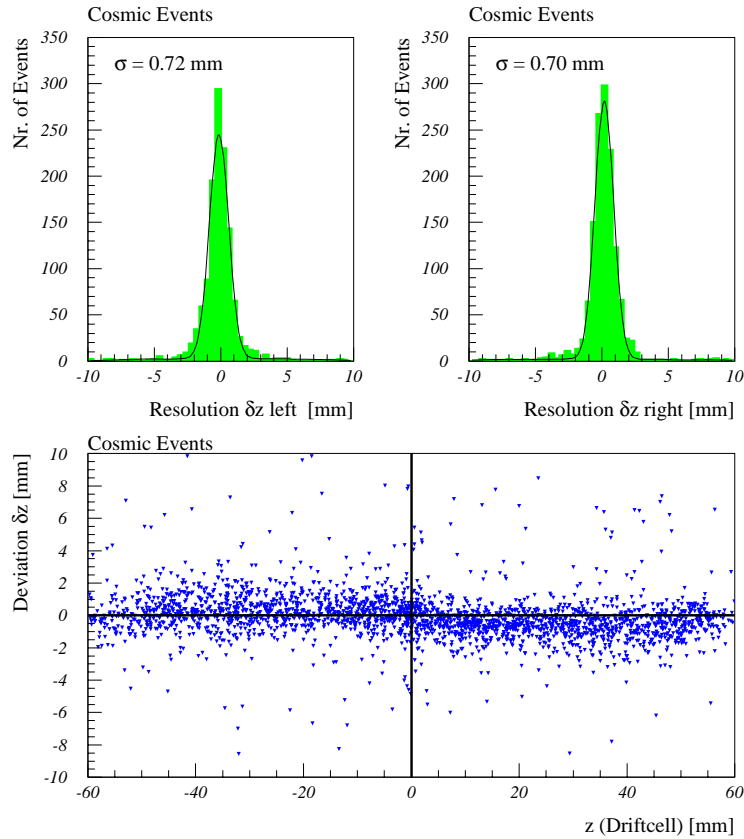


Figure 3.10: *Resolution and deviation of the CIZ calibration using cosmic data. In the lower plot 0 cm denotes the center of the drift cell. All driftcells are mapped into one*

using the COZ hits only and looking at the *deviations* of the CIZ hits from the track fit as a function of the drift distance, we will immediately see systematic shifts, caused by wrong  $t_0^{offset}$  or drift velocity  $v_D$ . Figure 3.10 shows the distributions for a well calibrated chamber. Further the single hit *resolution* can be determined by excluding each wire in turn from the fit, and then computing the distance from the hit observed to the line.

Table 3.1 gives an overview over the behaviour of the main calibration constants during the last years (1995 - 1998) in CRME time units <sup>9</sup> (one CRME time unit corresponds to 0.2 ns). The calibration with cosmic data and with *ep* data is described in detail in [53].

<sup>9</sup>CRME: The “Central\_Response\_Ynner\_z\_chamber\_Event bank”, containing the raw information (drift time and charge) of every hit measured in CIZ in one event.

|                |       |       |       |       |       |       |       |
|----------------|-------|-------|-------|-------|-------|-------|-------|
| year           | 95    | 96    | 96    | 96    | 97    | 97    | 98    |
| month          | june  | may   | sep.  | nov.  | apr.  | oct.  | aug.  |
| $c_{scale}$    | 1.040 | 1.029 | 1.009 | 1.003 | 1.010 | 1.010 | 1.039 |
| $t_0^{offset}$ | 77    | 91    | 88    | 101   | 87    | 87    | 79    |

Table 3.1: Drift velocity  $v_{drift}$  (calibration constant  $v_{cal}$ ) and time offset  $t_0$  of CIZ during the last three years.

### Efficiency monitoring

An efficiency check independent of other detector components is the *single wire efficiency*. If two hits on different wires within the same driftcell are measured a third is required to call the wire efficient. For good track measurements all three hits of the drift cell are needed. The *linking efficiency* is measured using tracks from the CJC. If at least two hits within the CIZ are found, which are associated with the CIZ is called efficient. The  $z$ -linked tracks are used to improve the measurement of the  $z$ -coordinate of a CJC track.

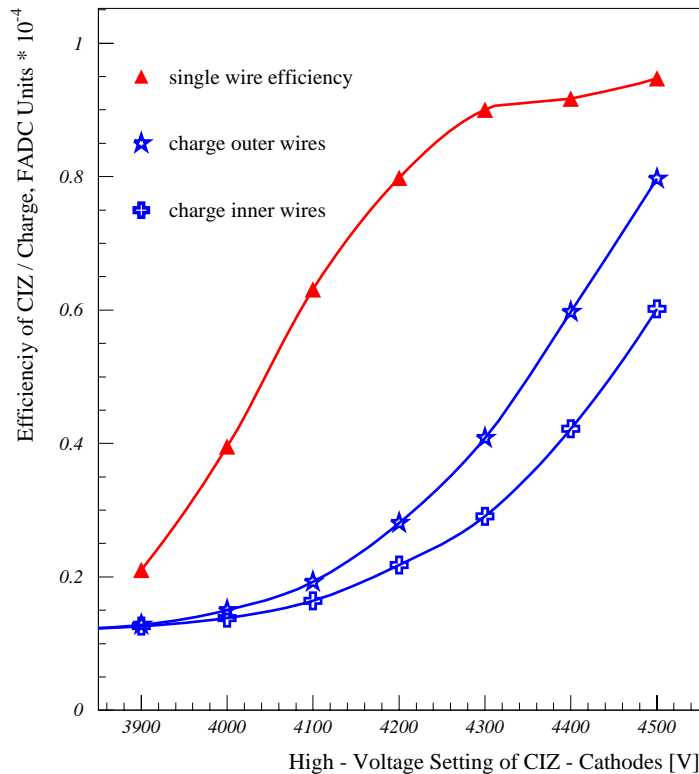


Figure 3.11: The correlation of the high voltage settings of CIZ signal and efficiency and the deposited charge. The charge is measured in CRME units scaled with  $10^{-4}$ .

In Figure 3.11 the charge deposited on the signal wires and the single wire efficiency are given as a function of the chamber high voltage (HV). The efficiency increases with the strength of the drift field and the charge produced. The efficiency saturates at  $HV_{cathod} = 4300$  V. This was the point of operation during the last years (1995 - 1998).

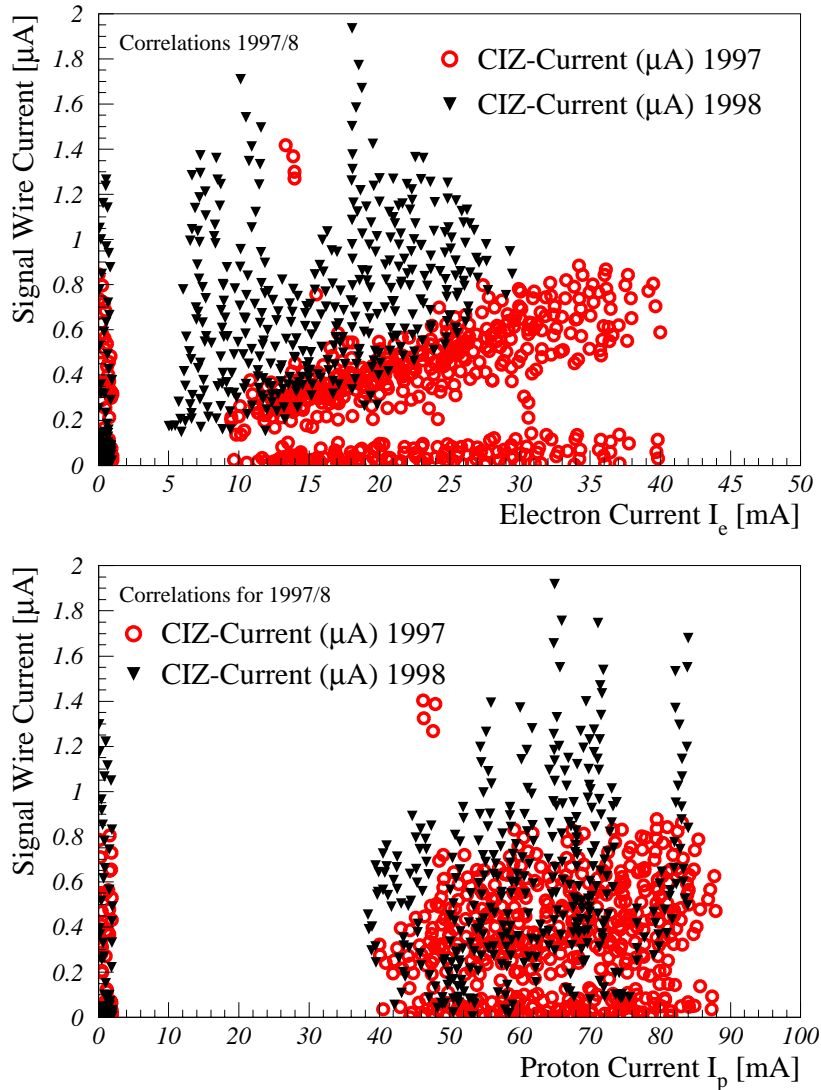


Figure 3.12: *The correlation of the beam currents an the currents measured on the CIZ signal wires for 1997 and 1998. The low signal currents correspond to the charging currents during the swich-on phase of the HV of the chamber in the early luminosity phase.*

The electron beam current  $I_e$  and the current of the signal wires (Figure 3.12) are strongly correlated. The proton beam current does not influence the chamber currents. This indicates that the load of the chamber originates mainly from the

electron beam background which is caused by synchrotron radiation. Due to this sensitivity CIZ is used for collimator studies and beam steering optimizations. The entries at  $I_{e,p} = 0$  occur, if the chamber is switched on during times of no beams (i.e. Cosmics).

Figure 3.13 presents the same correlations as above, but restricted to the forward region (ring 14) and to the backward region (ring 0 (1998), ring 1(1997)<sup>10</sup>) respectively. There is a tendency to higher chamber currents for the same proton beam currents in the forward direction whereas in the correlation to the electron beam current no difference could be seen. The event kinematics of H1 is strongly boosted to the forward region leading to a higher activity of the detector.

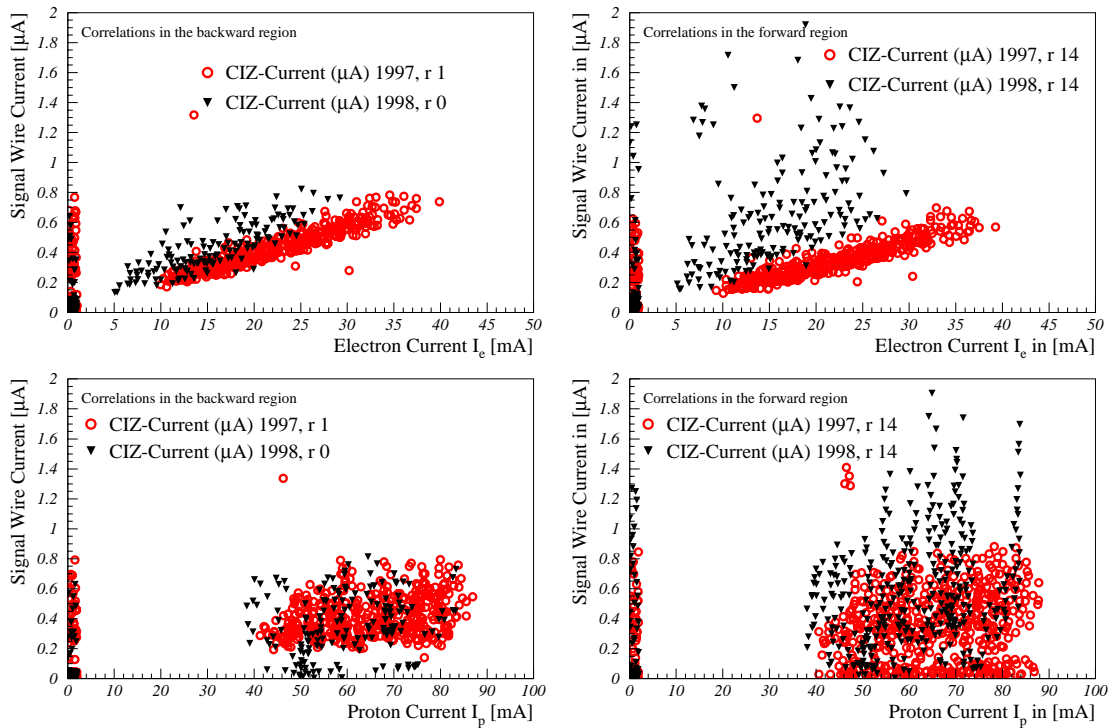


Figure 3.13: *The correlation of the beam currents an the currents measured on the CIZ signal wires for 1997 and 1998. The left figures present the backward region, the right figures the forward region, with respect to the proton beam direction.*

<sup>10</sup>Ring 0 was not available in 1997 due to problems with too high current in the ring, caused by deposits on the potential and signal wires.

### Ageing effects

Due to ageing effects a decreasing efficiency in time is expected. This is visualised in Figure 3.14, where the linking efficiency and the single wire efficiency are shown as function of the electron beam current for an early running period in 1995 and a late running period in 1997. The chamber was partially rewired in the winter shutdown 1994/95 and was not reopened until end of 1997. A clear reduction of the efficiencies can be seen. Another effect is visible, too: the efficiencies are decreasing with increasing electron currents. High electron currents cause high background rates, and high background rates increase the activity in the chamber. As can also be seen in Figure 3.13, the current measured on the signal wires increases with increasing electron currents. Thus too much charge is produced in the chamber, reducing the efficiency.

There are several factors influencing the ageing:

- deposits on the wires and cathodes from oil residues left over from the production of the wire,
- dirt in the chamber from the opening period,
- wrong gas mixture.

The oil residues can be removed with a special tool which cleans the wires before putting them into the chamber in a ultrasound bath. Dirt in the chamber during the opening time can only be avoided in a clean room. In the early phase of operating CIZ (1992, 1993) a gas mixture of Argon / Methane (80 % / 20 %) was used. Inspection of the wires showed serious ageing effects [53]. After the shutdown 1993/1994 a gas mixture of Argon / Ethane (70 % / 30 %) was used. This mixture caused much less deposits on the wires as was seen in the following shutdown.

Table 3.1 listed the development of the drift velocity  $v_D(c_{scale})$  and the time offset  $t_0^{offset}$ . Accompanying the decrease in efficiency is an increase of the drift velocity by about 3 %. The deposits on the wires lower the gas amplification near the signal wires, which explains the decrease of the efficiency. Obviously the drift field is influenced by the deposits on the wires, too. In the shut down 1997/1998 the chamber was completely rewired and cleaned, what is reflected in the drift velocity of 1998 (Table 3.1).

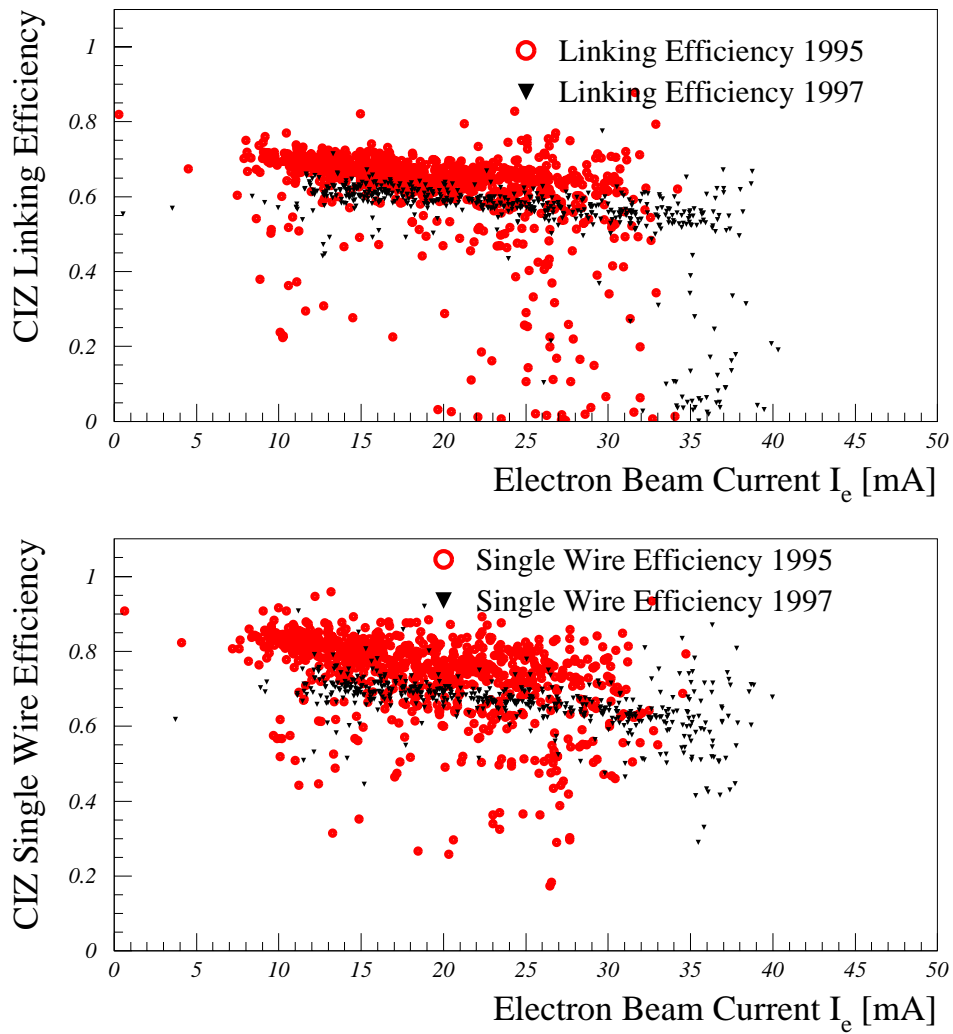


Figure 3.14: *The linking and single wire efficiency of CIZ after the rewiring 1994/95 and before the next rewiring 1997/98.*

# Chapter 4

## Event selection

In this chapter we describe the selection chain for events containing charm quarks in *photoproduction* from the  $ep$ -collision to the  $D^*$ -Signal. Charm quarks are produced predominantly by *photon gluon fusion* (PGF)  $\gamma g \rightarrow c\bar{c}$ , where the  $c\bar{c}$  pair fragments into a  $D^{*\pm}$ - Meson. If the scattered electron escapes the main part of the detector the process is called *photoproduction*. The lepton is either lost in the beam pipe (*untagged photoproduction*,  $Q^2 \leq 2 \text{ GeV}^2/c^2$ ) or detected at small angles with respect to the electron beam direction (*tagged photoproduction*,  $Q^2 \leq 0.01 \text{ GeV}^2/c^2$ ). In the analysis presented in this thesis tagged events are used only. The data were taken with the H1-detector during the run periods 1994 - 1996. In this period a total integrated uncorrected Luminosity of  $\mathcal{L} \approx 17 \text{ pb}^{-1}$  was delivered by the accelerator. Our subsample corresponds to  $\mathcal{L}_{sub} \approx 12.1 \text{ pb}^{-1}$ .

During data taking the events are first preselected online using the H1 trigger system, which is divided in four (five)<sup>1</sup> levels. One of these levels (Level 4) is the L4-Filter farm, as described in the previous chapter. For heavy quark candidates a classification routine *HQSEL* delivers a selection flag. The trigger conditions and the selection on L4/L5 is described in more detail in this chapter. The second part of data selection is done offline in the analysis of reconstructed data applying more sophisticated cuts and using the full event information.

### 4.1 Kinematics of events with charm

Production of charm quarks can be recognized by reconstruction of hadrons with charm. Good candidates for detection within the H1-detector are decays of  $D^*$ -Mesons. For this analysis the decay channel

$$D^{*\pm} \rightarrow D^0 \pi_s^\pm \rightarrow (K^\mp \pi^\pm) \pi_s^\pm \quad (4.1)$$

is used. The  $D^0$  meson is a  $J^P = 0^-$  state of a  $c$  and  $\bar{u}$  quark<sup>2</sup> and can only decay via weak interaction. The mass difference between the vector mesons  $D^{*\pm}$

---

<sup>1</sup>Level 5: offline data reconstruction.

<sup>2</sup>Charge conjugated states are always implicitly included.

(2010.0 MeV/c<sup>2</sup>) and  $D^{*0}$  (2006.7 MeV/c<sup>2</sup>) and the pseudoscalar mesons  $D^\pm$  (1869.3 MeV/c<sup>2</sup>) and  $D^0$  (1864.5 MeV/c<sup>2</sup>) originates from the different spin configuration of the quarks. The decay chain selected for the analysis has one of the highest branching ratios of decays with only charged particles in the final state. The tight kinematical conditions for this decay provide a further advantage for the analysis: the small value of  $m_{D^*} - (m_{D^0} + m_{\pi_s}) = 5.9$  MeV allows only a small phase space for accidental combinations. The momentum of the pion is very low in the  $D^*$  rest frame, it is usually called ‘slow pion’.

### 4.1.1 General properties of $D^*$ events

#### The generators AROMA/IJRAY

To illustrate the typical kinematical structure of the events we use Monte Carlo (MC) generators. The direct boson-gluon fusion induced events are produced with the generator AROMA [55, 56], the resolved part with the generator IJRAY [58]. The full electroweak structure of the electron-gluon interaction is contained in these generators with complete matrix elements up to the order  $\alpha^2\alpha_s$  and the masses of the heavy quarks are taken into account. Higher order QCD radiation is treated using initial and final state parton showers, and hadronization is performed using the Lund string model [60, 61]. The IJRAY generator is an adaption for the H1 experiment based on the PYTHIA generator [57], to simulate the QED vertex  $e \rightarrow e\gamma$  by calculation of the photon flux. It is basically the flux of transversely polarized photons with kinematical restrictions only on  $y$  and  $Q^2$  [59].

#### Kinematic studies

Figure 4.1 shows transverse momentum  $p_\perp$ , polar angle  $\vartheta$ , rapidity  $\hat{y}$  and  $\log_{10}(x_{gluon})$  of the  $D^*$  meson, separately for direct and resolved processes. The ratio of the direct and resolved components of the total cross section depend on  $Q^2$ . The resolved contribution increase with decreasing  $Q^2$ , i. e. it is high for events in photoproduction and vanishes for events of DIS ( $Q^2 > 2$  GeV<sup>2</sup>/c<sup>2</sup>). For this analysis  $Q^2 \approx 0$  and  $\overline{W}_{\gamma p} \approx 200$  GeV the direct and resolved processes are predicted [63] to contribute to the total cross section as:

$$\frac{\sigma_{\gamma p \rightarrow c\bar{c}}^{dir}}{\sigma_{\gamma p \rightarrow c\bar{c}}^{tot}} = 79\% \quad \frac{\sigma_{\gamma p \rightarrow c\bar{c}}^{res}}{\sigma_{\gamma p \rightarrow c\bar{c}}^{tot}} = 21\% \quad (4.2)$$

Due to the lower momentum of the interacting parton from the photon direction, resolved events have higher probability to be boosted in forward direction ( $+z$  direction), which leads to lower values of the polar angle and therefore to higher values of the rapidity of the  $D^*$  meson (Figure 4.1). The transverse momentum distributions can not be distinguished with experimental cuts. For the gluon momentum ( $x_{gluon}$ ) distribution only the direct part is shown. In the resolved process

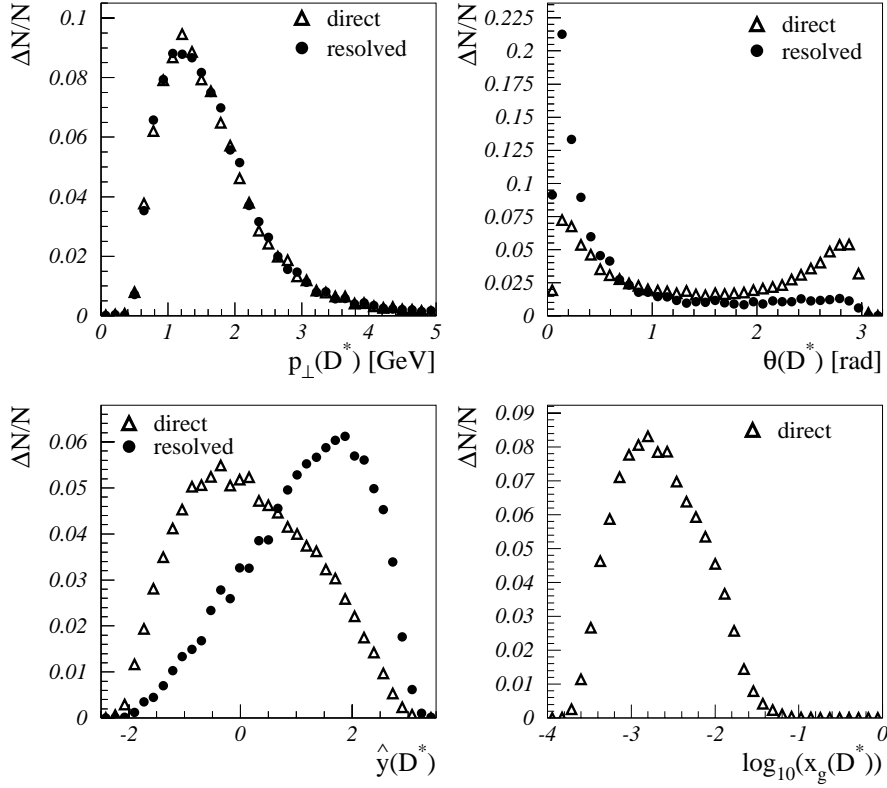


Figure 4.1: *Kinematical properties of the  $D^*$  meson: direct and resolved contributions in comparison*

$\sqrt{\hat{s}}$  is not given by the full photon energy and the relation

$$x_{gluon} = \frac{\sqrt{\hat{s}}}{W_{\gamma p}} \quad (4.3)$$

is not usable for the reconstruction of  $x_{gluon}$ .

#### 4.1.2 Detector motivated cuts on kinematical variables

There are two important acceptance restrictions by the H1-detector which affects the detection and reconstruction of kaons and pions from the  $D^*$  or  $D^0$  decay:

- the Central Jet Chamber (CJC) covers only a region of the polar angle  $\vartheta$  of  $20^\circ < \vartheta < 160^\circ$ ;
- the track reconstruction in the CJC needs a minimal transverse momentum  $p_\perp > 100 \text{ MeV}/c$ .

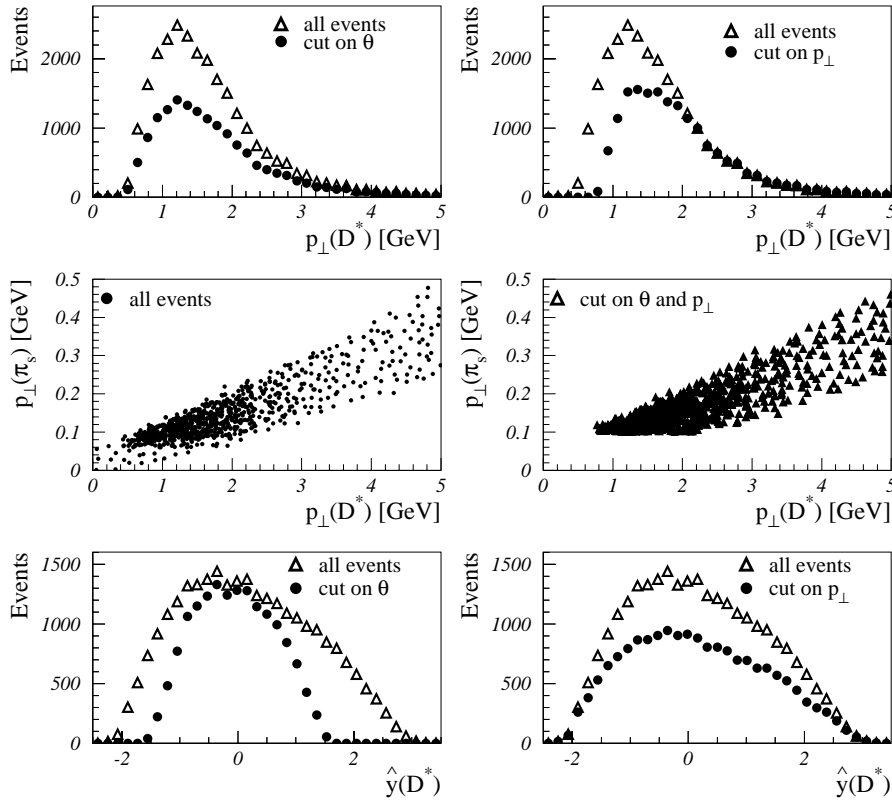


Figure 4.2: *Kinematical properties of the  $D^*$  meson: acceptance cuts*

For a good detection and reconstruction of a  $D^*$  meson a cut on  $\vartheta$  for all tracks ( $K$ ,  $\pi$  and  $\pi_s$ ) is needed. The transverse momentum conditions ensure that tracks reach at least the outer drift chamber (CJC2). For particles with lower transverse momentum multiple scattering and energy loss in the inner detectors and the beam pipe degrades the reconstruction quality, and also impedes the  $D^*$  reconstruction, because of the low transverse momentum of the slow pion  $\pi_s$  (Section 4.1). In the final analysis, the cut on transverse momenta of decay particles is increased further in order to suppress background events (Section 4.3).

The transverse momenta for  $\pi_s$  and  $D^*$  are strongly correlated (Figure 4.2). While the cut on  $\vartheta$  leaves the mean value of the transverse momentum of the  $D^*$  at  $\langle p_{\perp}(D^*) \rangle \approx 1.25$  GeV/c unchanged, the cut on  $p_{\perp}(\pi_s)$  leads to a higher mean value of  $p_{\perp}(D^*)$  ( $\approx 1.6$  GeV/c). This is also visible in the scatter plots: if the  $\pi_s$  cut is applied, the low  $p_{\perp}$  values of the  $D^*$  vanish. Later in the analysis there will be a stronger cut on  $p_{\perp}(D^*)$  in order to suppress background (Section 4.3). The cut on  $p_{\perp}(\pi_s)$  leaves rapidity distributions unchanged. The restricted range of  $\vartheta$  of course limits also the rapidity to the central region of  $-1.5 < \hat{y} < 1.5$ . The kinematical

distributions of the decay particles are shown in Figure 4.3.

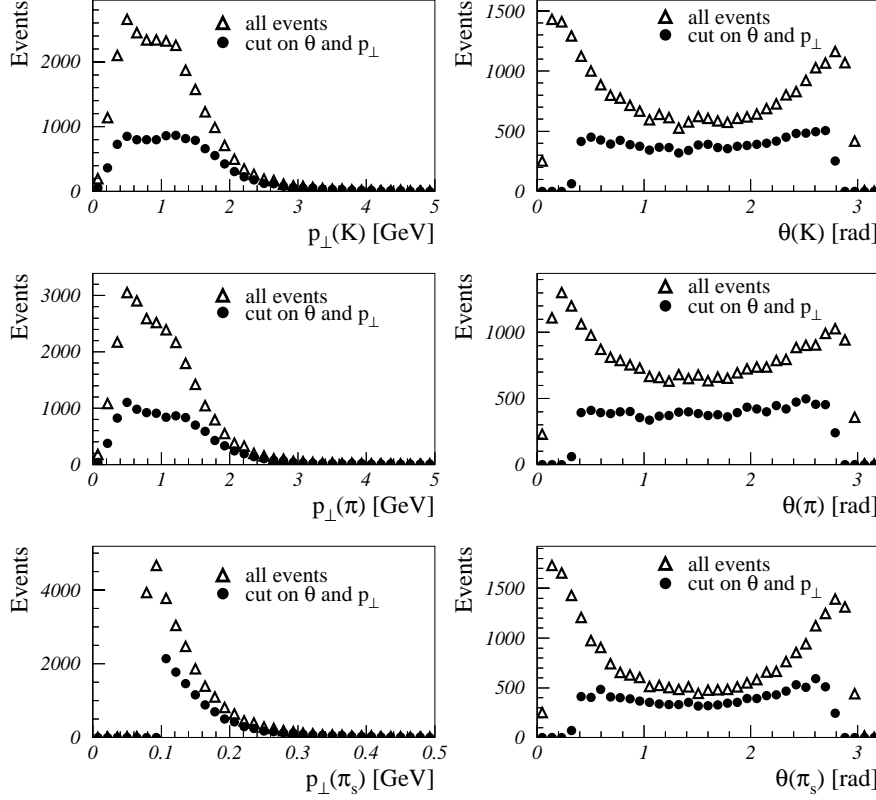


Figure 4.3: *Kinematical properties of the kaons and pions from the  $D^*$  and  $D^0$  decays.*

## 4.2 Online data selection

The online data selection consists of the first level trigger (*subtriggers*) and the filter farm ( $L_4$ ). A brief overview of the online event classification as a part of the  $L_4$  - filter farm from the point of view of heavy quark physics is given, too.

### 4.2.1 L1 Trigger and the photoproduction subtriggers

Nearly all detector components contribute to the first level trigger, which handles 192 trigger elements (TE). These trigger elements are combined to 128 different subtriggers (ST) in the central trigger logic. If at least one of the subtriggers gives a signal, the event is kept<sup>3</sup>.

<sup>3</sup>This is called *L1-keep*.

Generally there are four different classes of trigger systems: track trigger (CJC, MWPC), calorimeter triggers (LAR), muon triggers (Fwd- $\mu$  system, central- $\mu$  system) and electron triggers (SPACAL, e-tagger). Several veto and timing conditions are included in all subtriggers for background reduction as well. The event topology is not affected by these additional requirements. For open charm ( $D^*$ ) events, only track and electron triggers are used. Due to the small transverse energy flow, calorimeter triggers are not included in online data selection. Trigger elements which are building subtriggers relevant for the  $D^*$  analysis are described below:

**Electron Tagger (ET):** The trigger element *eTag* is set, if the deposited energy  $E'_e$  of the scattered electron in the ET exceeds 4 GeV. To avoid background from the bremsstrahlung process<sup>4</sup>  $ep \rightarrow ep\gamma$  the energy measured in the photon detector is required to be below 2 GeV.

**Central Jet Chamber (CJC):** The drift chamber trigger ( $DCr\varphi$ -trigger) delivers various trigger elements. They are derived from the signals of 10 of the 56 wire layers. These signals are digitized and transferred to shift registers. The drift time information is then compared with predefined masks, which contain bit patterns corresponding to track candidates with  $p_\perp > 400$  MeV/c. The trigger elements include information of transverse momentum, multiplicity and the sign of curvature. In order to reduce background sufficiently the  $DCr\varphi$  trigger is only sensitive to events whose distance to the beam axis is small ( $|DCA| < 2$ cm).

**Proportional Chambers (MWPC):** For a first estimate of the  $z$  position of the event vertex the multiwire proportional chambers (CIP, COP, FPC1) are used, from which the  $z$ -vertex trigger is derived. CIP and COP are double layer cylindrical MWPC with pad readout<sup>5</sup>. Particles with a transverse momentum of at least 150 MeV/c cross both CJC1 and CJC2 and therefore also CIP and COP. Coincidences signals from pads of each of the four layers of CIP/COP are combined to rays for all 16  $\varphi$  segments and extrapolated to the beam axis. The  $z$ -coordinate of the intersection of the ray with the beam axis is filled into a histogram of 16 bins ( $z$ -vertex histogram) within the region of  $\pm 44$  cm around the interaction point. For correct combinations of pads this yields a peak in the histogram. Background and wrong combinations of pads deliver a flat distribution. According to the significance of the peak various trigger elements are set.

**Time of flight system:** The ToF-system placed in the backward region of the main H1 detector is reached earlier by particles out of background interaction than those from the nominal  $ep$  interaction point (for example beam gas events of the proton beam). Therefore, two time slots are defined: ToF\_BG for background and ToF\_IA for interaction. This gives various trigger elements for background reduction. In 1995 additional ToF-Systems were installed in the backward ( $-z$ ) and forward ( $+z$ ) direction.

---

<sup>4</sup>This process is needed for the luminosity measurement.

<sup>5</sup>For the segmentation of CIP and COP see Chapter 3.2.1.

### Photoproduction subtrigger

The subtrigger for tagged photoproduction events requires as main conditions a measured electron in the electron tagger (ET) at  $z = -33$  m, a significant vertex, at least three track candidates in CJC and some veto conditions. All conditions are as follows:

- (eTag\_33): activity in ET at  $-33$  m
- (zVtx\_sig): significant peak in the  $z$ -vertex histogram
- (DCr $\varphi$ \_Tc): at least three track candidates in CJC
- ( $\neg$ BToF\_BG)  $\wedge$  ( $\neg$ CIP\_Backward): veto on background activity in the backward time of flight system and in the backward region of the central inner proportional Chamber (CIP)
- (FToF\_IA)  $\vee$  ( $\neg$ FToF\_BG): interaction or veto on background activity in the forward time of flight system
- ( $\neg$ SPLe\_AToF\_E1): no activity in the electromagnetic SPACAL at wrong time
- (zVtx\_T0):  $T_0$  signal from the  $z$ -vertex trigger

The subtrigger for tagged photoproduction carries the number **ST 83**. The trigger condition was stable in 1995 and 1996. In 1994 the condition for the track candidates and the background suppression by the backward ToF were different:

- (DCr $\varphi$ \_T<sub>neg</sub>): at least one track candidate in CJC with negative curvature
- (ToF\_BG): The backward ToF system was exchanged in the shutdown 1994/1994

The data for this analysis were collected with ST 83. During all running periods used for this analysis, the trigger was not changed. In the running period 1996, a new electron tagger was installed at  $z = -44$  m. The data out of this device were not used in this analysis.

#### 4.2.2 Filter farm and event classification

The fourth level of the H1 trigger system is called *L4 filter farm*. This is an asynchronous software trigger consisting of a farm of  $\sim 30$  parallel processors and is the last part of online data acquisition. All detector information is available and a reduced version of the H1 reconstruction program is applied. The aim of L4 is to verify the L1 trigger decision, to identify background events, to reject and to classify the kept event within various event classes, corresponding to the physics classes of the offline analysis. The event rate is reduced by more than 70 %. The aim of the event classification is to sort events into subsamples for the different physics analyses.

### Online heavy flavour event classification

The event finder *HQSEL* was written to select open charm events in exclusive decay channels. The package is designed to run on Level 4 of the H1 trigger system and also for the event classification on level 5. Hence both are using the same code, although some settings flags allow differences in operation and cut settings between L4 and L5. The code can run in a  $\gamma p$  or in a DIS mode. The sum of both modes determines the heavy quark event class. HQSEL is called on L4 for selected heavy quark subtriggers only ( $\gamma p$  and DIS). Further the program searches for events in several selected decay channels (ca. 14 channels) for  $D^*$ ,  $D^0$ ,  $D^\pm$ ,  $D_s^\pm$  and  $\Lambda_c^\pm$ . If any of the selected heavy quark subtriggers was verified on L4 and at least one candidate in any of the possible decay channels was found, the Heavy Quark selection bit is set to true.

The general structure of selection on L4 is first to search for open charm channels in  $\gamma p$  mode and second for a DIS electron candidate. If an electron candidate is found, the open charm decay channels are checked as in the  $\gamma p$  mode. Tracks are sorted into normal (*NQT*) and high quality tracks (*HQT*). All kaons of all decay channels are requested to be HQT. Every channel has a  $p_\perp$  cut on its initial particle momentum, increasing the value of the cut is used to control the rate of the individual channel. The further selection steps do not differentiate between these two classes. The parameters of the cuts are listed in Table 4.1. The loop over all combinations of tracks surviving the cuts also includes  $K_S^0$  and  $\Lambda$  candidates ( $V_0$ )<sup>6</sup>. Invariant mass combinations and transverse momenta for heavy quark event candidates are calculated and further cuts are applied. For the decay channel 4.1 looked at in this analysis cuts on the invariant masses of the  $D^0$  and the  $D^*$  are applied:  $|M(D^0) - M(D^0_{mess.})| < 100 \text{ MeV}/c^2$ ,  $|\Delta M(D^*) - \Delta M(D^*_{mess.})| < 170 \text{ MeV}/c^2$ . Further a cut on  $p_\perp$  of the  $D^*$  is set to 1.4 GeV/c for the  $\gamma p$  mode and to 1.0 GeV in the DIS mode.

When all calculations are done and candidates for predefined decay channels are found, the corresponding bits in two identification words (one each for  $\gamma p$  and DIS) are set. If any bit of any word is set, the classification bit for a heavy quark candidate is set.

### 4.3 Offline data selection

In the offline data selection the cuts on the track quality of the  $D^*$  particles  $\pi$ ,  $K$  and  $\pi_s$  are refined to suppress background. For photoproduction events a well measured electron in the tagger (ET) of the luminosity system is required, too, which demands acceptance cuts in this detector.

After reconstruction of the data (L5) the analysis programs search for charmed events fulfilling the criteria of the decay chain 4.1. The event candidates marked by

---

<sup>6</sup>A  $V_0$  is a combination of two tracks with opposite charge to a common secondary vertex.

| Var.                    | HQT        |         | NQT        |          |
|-------------------------|------------|---------|------------|----------|
|                         | $\gamma p$ | DIS     | $\gamma p$ | DIS      |
| $DCA <$                 | 0.4 cm     | 0.5 cm  | 2.0 cm     | 2.0 cm   |
| $R_{start} <$           | 25.0 cm    | 25.0 cm | 35.0 cm    | 35.0 cm  |
| $Track_{len} >$         | 25.0 cm    | 25.0 cm | 10.0 cm    | 10.0 cm  |
| $ z_{trk} - z_{evt}  <$ | 12.0 cm    | 12.0 cm | 20.0 cm    | 20.0 cm  |
| $p_{\perp}(\pi, K) >$   | 0.2 GeV    | 0.2 GeV | 0.12 GeV   | 0.12 GeV |
| $p_{\perp}(\pi_s) >$    | no cuts    |         | 0.1 GeV    | 0.1 GeV  |

Table 4.1: Cut parameters of the  $L4$  heavy quark finder on the track variables

the L4 classification (HQSEL) are subjected to general cuts concerning the whole event and more specific cuts applied individually to the various particles.

### General event specific cuts

Only runs<sup>7</sup> are accepted during which all important detector components are functioning and the beam conditions were stable (GOOD and MEDIUM runs). If due to high voltage problems one of the detector components relevant for this analysis was temporarily not available, the event is rejected too (HV Bits). Furthermore the reconstructed  $z$  position of the vertex is required to lie within  $\pm 40$  cm. The  $z$ -vertex distribution (Figure 4.4) has a width of  $\sigma_{z-vertex} = 11.2$  cm and is centered at  $\langle z - vertex \rangle = -1.3$  cm.

### Cuts on $D^*$ candidates and decay products

The cuts on kinematical quantities of  $D^*$ ,  $K$ ,  $\pi$  and  $\pi_s$  have already been discussed in Section 4.1 and are listed in Table 4.2. The most important difference to the Monte Carlo studies is, that the transverse momentum cuts have been raised in order to suppress combinatorial background

Further refinements concern the track quality. To ensure that a track starts in CJC1, the radial distance of the first hit from the beam line ( $r_{start}$ ) has to be smaller than 50 cm. We lower this limit to 35 cm, and require a minimum track length of 10 cm. This improves the momentum measurement, and avoids the problem of double counting split tracks, i. e. those where the track segments associated with a single particle in CJC1 and CJC2 do not match sufficiently well, and are thus treated as two tracks. The cut on the distance of closest approach DCA selects tracks from the primary vertex region.

Since particle identification is not possible over the full momentum range, both hypotheses have to be tested for the  $K$  and  $\pi$  masses. The accepted charge com-

<sup>7</sup>A run is the smallest unit of H1-data taking with a maximal duration of two hours.

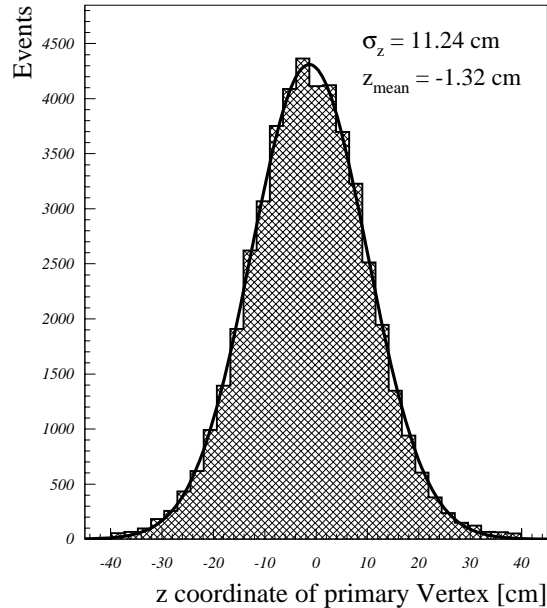


Figure 4.4:  $z$  coordinate of primary event vertex with Gaussian fit

binations are:

$$(K^- \pi^+) \pi_s^+ , (K^+ \pi^-) \pi_s^- \quad (4.4)$$

For  $D^0$  candidates the invariant mass  $M(K\pi)$  of the two oppositely charged tracks is required to lie within a region of  $\pm 100$  MeV/ $c^2$  around the nominal  $D^0$  mass of  $(1.864.5 \pm 0.5)$  GeV/ $c^2$  [64]. The measured mass resolution is  $\sigma_{M(K\pi)} = (24.2 \pm 2.3)$  (see Section 4.5.1). The mass difference  $\Delta M$  of the  $D^*$  candidate is required to lie below 180 MeV/ $c^2$ . Opening this cut unnecessarily increases the number of accepted events, decreasing the value narrows the region from which the background under the signal can be extrapolated. For candidate events with the overall charge combinations and  $\Delta M < 155$  MeV/ $c^2$  the cut on the  $D^0$  mass is expanded to  $\pm 400$  MeV/ $c^2$ , to allow for a check of the  $D^0$  mass resolution (see Figure 4.7). These cuts are summarized in Table 4.3.

### Electron cuts

The center of mass energy of the  $\gamma p$  ( $W_{\gamma p}$ ) system is determined by the energy deposited by the scattered electron in the electron tagger  $E_e^{eTag}$ : (see Equation 1.13):

$$y = 1 - \frac{E_e^{eTag}}{E_e}, W_{\gamma p} = \sqrt{ys}. \quad (4.5)$$

| <b>general event parameters</b>                                                                |                                                      |
|------------------------------------------------------------------------------------------------|------------------------------------------------------|
| primary vertex                                                                                 | $ z - vertex_{prim}  \leq 40$ cm                     |
| $\sigma(z - vertex_{prim})$                                                                    | $\sigma_{zvtx} \leq 10$ cm                           |
| run quality                                                                                    | GOOD and MEDIUM runs                                 |
| <b>parameters of the electron tagger</b>                                                       |                                                      |
| inelasticity $y$                                                                               | $0.29 \leq y \leq 0.62$                              |
| impact point $X_0$                                                                             | $ x_0  \leq 6.5$ cm                                  |
| <b>parameters of <math>D^*</math>, <math>K</math>, <math>\pi</math> and <math>\pi_s</math></b> |                                                      |
| polar angle $\vartheta$                                                                        | $20^\circ \leq \vartheta \leq 160^\circ$             |
| transverse momentum $p_\perp(K, \pi)$                                                          | $p_\perp \geq 500$ MeV                               |
| transverse momentum $p_\perp(\pi_s)$                                                           | $p_\perp \geq 150$ MeV                               |
| transverse momentum $p_\perp(D^*)$                                                             | $2.5 \text{ GeV} \leq p_\perp \leq 10.5 \text{ GeV}$ |
| rapidity $\hat{y}(D^*)$                                                                        | $ \hat{y}  \leq 1.5$ MeV                             |
| <b>parameters of track quality</b>                                                             |                                                      |
| track length                                                                                   | $\ell_{track} \geq 10$ cm                            |
| start radius                                                                                   | $R_{start} \leq 35$ cm                               |
| dist. of closest approach                                                                      | $DCA \leq 2$ cm                                      |

Table 4.2: *Cut parameters of  $D^*$  selection for reconstructed data.*

|               |                                                                                                                                                            |
|---------------|------------------------------------------------------------------------------------------------------------------------------------------------------------|
| signal region | $ M(K\pi) - M(D^0)  < 400$ MeV<br>for $0 \text{ MeV} < \Delta m < 155$ MeV<br>$ M(K\pi) - M(D^0)  < 100$ MeV<br>for $155 \text{ MeV} < \Delta m < 170$ MeV |
| $D^0$ mass    | $ m_{K\pi} - m_{D^0}  < 80$ MeV                                                                                                                            |

Table 4.3: *Cut parameters on the invariant mass of  $D^0$  for reconstruction a  $D^*$  signal*

The acceptance of the electron tagger at  $-33$  m shown in Figure 4.6 (Section 4.4.1) covers the region of  $160 \text{ GeV} < W_{\gamma p} < 240 \text{ GeV}$ . If the  $x$ -coordinate of the electron impact point is near the edges of the tagger, parts of the produced particle shower leak out of the detector, and the energy measurement becomes less reliable, as can be seen in Figure 4.5. In vertical direction the effect is less prominent. Therefore only a cut on the horizontal impact point is applied. Since the horizontal impact point is linked to the energy of the scattered electron and hence to  $y$  (Equation 1.10, this cut effectively determines the acceptance referred to above. The electron cuts are also listed in Table 4.2.

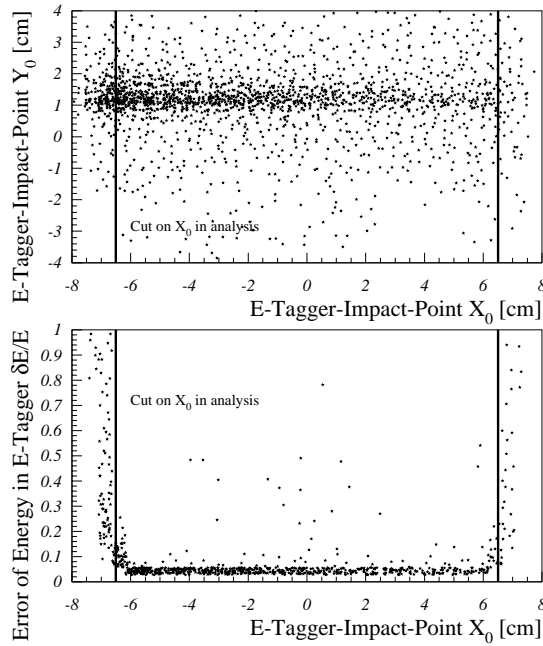


Figure 4.5:  $X_0$  versus  $Y_0$  of impact point of electron-tagger, error of energy measurement in dependence of  $X_0$ .

## 4.4 Luminosity

The integrated luminosity is measured run-wise by using the Bethe-Heitler process  $ep \rightarrow ep\gamma$ . In QED the cross section of this process is well known and theoretically predicted with high precision. For a good luminosity measurement some corrections have to be applied concerning proton pilot bunches, functionality of detectors, and prescale factors of subtrigger. In Table 4.4 the total luminosity and the luminosity for ST83 are listed, both corrected and uncorrected.

The luminosity correction rejects all runs where not all main detector components are fully operational (POOR runs). Furthermore, a fully operating high voltage

| sample       | 1994 [nb <sup>-1</sup> ] | 1995 [nb <sup>-1</sup> ] | 1996 [nb <sup>-1</sup> ] | 1994-1996 [nb <sup>-1</sup> ] |
|--------------|--------------------------|--------------------------|--------------------------|-------------------------------|
| all          | 3003                     | 4517                     | 9506                     | 17026                         |
| all, corr.   | 2774                     | 3910                     | 7769                     | 14453                         |
| ST 83        | 2991                     | 2026                     | 9309                     | 14326                         |
| ST 83, corr. | 2765                     | 1727                     | 7620                     | 12112                         |

Table 4.4: Overview of the integrated luminosities  $\int \mathcal{L} dt$  1994 -1996

supply for all detector components used for this analysis is requested. The presence of proton satellite bunches at  $\tau_{sat} = 19.2$  ns and at  $\tau_{sat} = 4.8$  ns with respect to the nominal proton bunch makes an additional correction necessary. The measurement of luminosity is also sensitive to events of bremsstrahlung released by the pilot bunches, whereas interactions with an electron are rejected by the  $z$ -vertex cut of  $\pm 40$  cm. This effect must also be taken into account. Finally, for the luminosity of a specific subtrigger the prescale correction has to be applied. A prescale factor  $n_{scale}$  means that only every  $(n_{scale} + 1)^{th}$  event delivers an L1-keep signal. Prescale factors are used to adapt the trigger rates run-wise to actual beam conditions.

#### 4.4.1 Electron-tagger acceptance

The electron hits the electron tagger only, if it is scattered less than 5 mrad in theta and if the energy lies in the region of  $5.5 \text{ GeV} < E'_e < 22 \text{ GeV}$ . This corresponds to  $Q^2 \leq 0.01 \text{ GeV}^2/c^2$ . The acceptance of the detector depends on the kinematical variables  $y$  and  $Q^2$  and also on the beam position of the electron beam. The dependence on  $Q^2$  can be neglected, the dependence on  $y$  (Figure 4.6) is taken into account in this analysis

In the Weizsäcker-Williams approximation [17] (see chapter 2.1) the  $ep \rightarrow D^* X$  process factorizes into a photon proton interaction and the photon flux. The acceptance of the ET for  $D^*$  events  $\mathcal{A}$  does not depend on the topology of the event, but enters through the photon flux, i. e. it depends on the inelasticity of the electron  $y$ .  $\mathcal{A}(y)$  is well known [65] and is used event-wise.

Every event is weighted by  $w_i(y) = \frac{1}{\mathcal{A}_i(y)}$ . To avoid large weights as in the tails, where also the energy measurement is less accurate, events are only kept, if the acceptance  $\mathcal{A}(y)$  exceeds the value 0.2.

## 4.5 The $D^*$ signal

In this section the last step of the chain from the  $ep$  event up to a  $D^*$  signal is shown. As described in the beginning of this chapter, this analysis makes use of the  $D^*$ -tagging, especially of the tight kinematical conditions of the decay  $D^* \rightarrow D^0 \pi_s \rightarrow (K\pi)\pi_s$ . The distribution of the mass difference

$$\Delta M = M(D^0 \pi_s) - M(D^0). \quad (4.6)$$

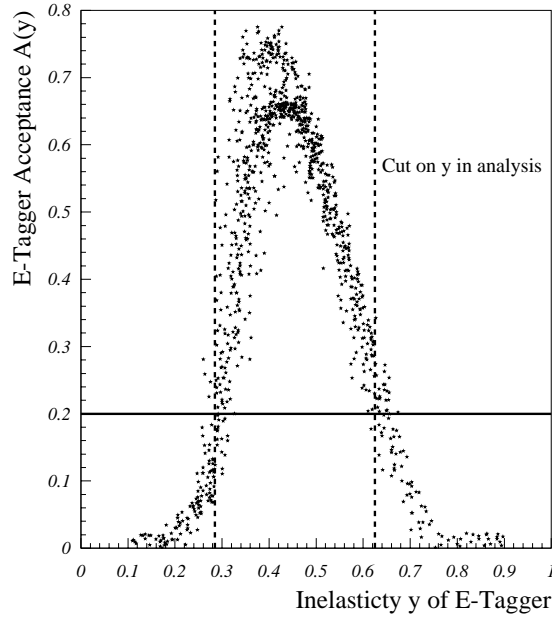


Figure 4.6: *The acceptance of e-tagger  $\mathcal{A}(y)$  in function of the inelasticity  $y$*

for the right charge combinations shows a clear peak at  $\Delta M = 145.4 \text{ MeV}/c^2$  (Figure 4.7). The expected mass difference is  $\Delta M = m_{D^*} - m_{D^0} = (145.42 \pm 0.05) \text{ MeV}$  [64]. To demonstrate that the events are coming from the proper decay channel the  $M(K\pi)$  invariant mass distribution for events from the signal region is shown also in Figure 4.7. A clear peak is visible at the nominal value of the  $D^0$  mass  $M(D^0) = 1.865 \text{ GeV}/c^2$  [64]

#### 4.5.1 Fit method

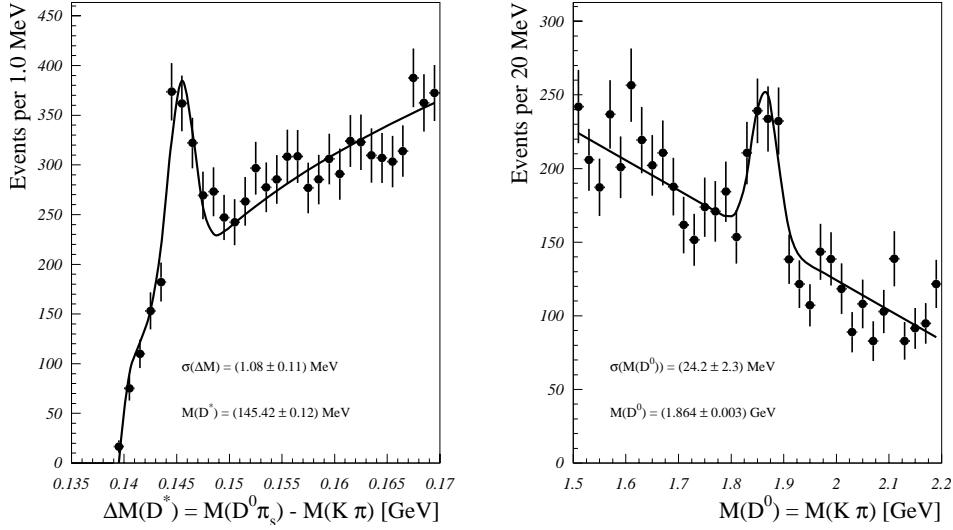
The number of  $D^*$  events is found by a fit of the  $\Delta M$  distribution shown in Figure 4.7 which contains the weighted number of  $D^*$  candidates  $\tilde{N}$ .

$$\tilde{N} = \sum_{i=1}^N \frac{1}{\mathcal{A}_i(y)} \quad (4.7)$$

with the statistical error [66]

$$\sigma_{\tilde{N}}^2 = \sum_{i=1}^N \left( \frac{1}{\mathcal{A}_i(y)} \right)^2. \quad (4.8)$$

In order to measure differential and double differential cross section a special treatment of weighted histograms is needed. The method described in [66] is called “Equivalent Number of Events” and described in the next chapter (section 5.2.1).

Figure 4.7:  $\Delta M$  fit of  $D^*$  signal and  $D^0$  signal

The fit function  $f(\Delta M) = f_{signal}(\Delta M) + f_{background}(\Delta M)$  used in the fit consists of a Gaussian of variable width, position and amplitude for signal region added to a polynomial describing the background.

$$f_{signal}(\Delta M, N, \mu, \sigma) = \frac{N}{\sqrt{2\pi} \cdot \sigma} \cdot e^{-\frac{(\Delta M - \mu)^2}{2 \cdot \sigma^2}} \quad (4.9)$$

$$f_{background}(\Delta M, A, b) = A \cdot (\Delta M - m_\pi)^b. \quad (4.10)$$

The fit is done by the maximum likelihood method minimizing the  $\chi^2$  given by errors in equation 4.8. The corresponding curves are shown in Figure 4.7. The unweighted number of  $D^*$  events seen is 550 with a statistical error of 48. The width of the  $D^*$  signal has been measured to  $\sigma_{D^*} = (1.08 \pm 0.11)$  MeV/ $c^2$ . To avoid correlations of errors the peak width is fixed for a second fit to determine the error of the total number of  $D^*$  events. The measured centroid of the  $D^0$  mass  $\langle M(D^0) \rangle = (1.864 \pm 0.003)$  GeV/ $c^2$  is in good agreement with the values published in [64], too. The width of the  $D^0$  peak is measured as  $\sigma_{D^0} = (24.2 \pm 2.3)$  MeV/ $c^2$ . This confirms the choice of the cut on the  $D^0$  mass.

The shape of background near the threshold is determined by the phase space for accidental combinations, which fortunately is very small. The phase space for the narrow signal region can be taken as constant. The number of accidental combinations delivering a  $D^*$  candidate within the region of invariant mass  $M$  up to  $M + dM$  is given approximately by:

$$dN \propto \sqrt{\Delta M - m_\pi} \cdot dM. \quad (4.11)$$

A good description of background is given if this is written more generally as

$$\frac{dN}{dM} = A \cdot (\Delta M - m_\pi)^b. \quad (4.12)$$

This is exactly the form used in equation 4.9. The exponent of the background is treated as a free value and found to be  $(0.37 \pm 0.01)$ , which is close to the expected value of 0.5 for the full phase space.

# Chapter 5

## Measurement of charm cross sections

In the previous chapter the data reduction from the whole amount of  $ep$  data to a clean sample of  $D^*$  events in photoproduction has been described. The aim of this chapter is to outline the measurement of the charm photoproduction cross section  $\sigma_{\gamma p}$ . The analysis includes the measurement of the total cross section in the visible and full range ( $\sigma_{\gamma p}^{vis}$ ,  $\sigma_{\gamma p}^{tot}$ ), the inclusive single differential cross section as function of  $p_{\perp}$  and  $\hat{y}$  ( $d\sigma_{\gamma p}/dp_{\perp}$ ,  $d\sigma_{\gamma p}/d\hat{y}$ ) and finally the double differential cross section in bins of  $p_{\perp}$  and  $\hat{y}$  ( $d^2\sigma_{\gamma p}/dp_{\perp}d\hat{y}$ ).

Firstly, some general aspects of cross section measurement are discussed. Due to the fact that HERA is an  $ep$  collider, the cross sections measured are electroproduction cross sections. The connection to the photoproduction cross section is given by the Weizsäcker-Williams approximation discussed in chapter 2.1. Because of the usage of the electron tagger for the analysis, we have to deal with weighted histograms (see chapter 4.5.1), which are not following the Poisson statistic anymore. Therefore, they have to be reweighted for the final fits by the “equivalent number of events” method.

For the cross section measurement a good knowledge of the acceptance of the detector  $\mathcal{A}$ , the reconstruction efficiency  $\varepsilon_{rec}$  and the trigger efficiency  $\varepsilon_{trig}$  is essential. They are studied in detail using simulated and reconstructed Monte Carlo events. Efficiency calculations were done for the direct and the resolved process separately and the results were summed, weighted with the predicted mixing ratio.

Studies of systematic errors have been done using real and Monte Carlo data samples. Contributions to the systematic error originate from detector effects or theoretical uncertainties.

## 5.1 General aspects of cross section measurement

The connection of cross section, number of events and luminosity is:

$$\int L(t)dt \cdot \sigma(ep \rightarrow e'D^*X) = N_{true}^{D^*} \quad (5.1)$$

The charm production cross section in the visible range of the detector is then given by the expression

$$\sigma_{vis}(ep \rightarrow e'D^*X) = \frac{N(D^{*\pm} \rightarrow K^\mp \pi^\pm \pi_s^\pm)_{obs}}{BR(D^* \rightarrow K \pi \pi_s) \mathcal{L} \mathcal{A}_{det} \varepsilon_{rec} \varepsilon_{trig}} \quad (5.2)$$

where:

- $N(D^{*\pm} \rightarrow K^\mp \pi^\pm \pi_s^\pm)_{obs}$ : number of  $D^*$  events measured in the running periods 1994, 1995 and 1996 with the photoproduction subtrigger (ST 83) and found in the  $D^*$  peak after all selection and analysis cuts
- $BR(D^* \rightarrow K \pi \pi_s)$ : branching ratio for the decay channel  $D^{*+} \rightarrow D^0 \pi_s^+ \rightarrow (K^- \pi^+) \pi_s^+$
- $\mathcal{L}$ : luminosity seen by ST 83, including correction for prescaling, pilot bunches and high voltage problems of detector components needed (see chapter 4.4)
- $\mathcal{A}_{det}$ : correction for detector acceptance
- $\varepsilon_{rec}$ : reconstruction efficiency
- $\varepsilon_{trig}$ : total trigger efficiency of all components of ST 83

The acceptance and efficiency corrections depend on the geometrical properties of the detector, on the spectra of the produced  $D^*$  meson, and are also influenced by the kinematics of the  $D^*$  decay. The corrections are extracted out of a simulated and reconstructed Monte Carlo Data sample. Due to changes of the trigger and detector performance from year to year this has to be evaluated for every year separately.

The number of  $D^*$  candidates observed corresponds to the electroproduction cross section  $\sigma_{ep}(ep \rightarrow e'D^*X)$ . The photoproduction cross section of charm  $\sigma_{\gamma p}(\gamma p \rightarrow c\bar{c}X)$  can be obtained by factoring out the photon flux factor  $f_{\gamma/e}$  (WWA, [17], chapter 2.1). This can be done because the cross section  $\sigma_{\gamma p}$  does not strongly depend on  $W_{\gamma p}$  or on  $y$  ( $W_{\gamma p} = \sqrt{y \cdot s}$ ), respectively:

$$\begin{aligned} \sigma(ep \rightarrow e'c\bar{c}X) &= \int dy f_{\gamma/e}(y) \cdot \sigma(\gamma p \rightarrow c\bar{c}X) \\ &\simeq \sigma_{\gamma p}(\bar{y}) \int_{y_{min}}^{y_{max}} f_{\gamma/e}(y) dy. \end{aligned} \quad (5.3)$$

The photon flux factor is obtained in the extended Weizsäcker Williams approximation (equation 2.4, [17, 18]) for the kinematical region of HERA as:

$$f_{\gamma/e}(y) = \frac{\alpha_{em}}{2\pi} \left[ \frac{1 + (1-y)^2}{y} \cdot \ln \frac{Q_{max}^2}{Q_{min}^2} - 2 \frac{1-y}{y} \left(1 - \frac{Q_{min}^2}{Q_{max}^2}\right) \right] \quad (5.4)$$

$$\begin{aligned} Q_{max}^2 &= E_e^2 (1-y) \vartheta_{min}^2 = 10^{-2} \text{GeV}^2 \\ Q_{min}^2 &= \frac{(y \cdot m_e)^2}{1-y}. \end{aligned} \quad (5.5)$$

This analysis makes only use of tagged events, which means that the electron is required to be detected within the electron tagger ET. The geometrical acceptance of the ET gives the limit of  $\vartheta_{min} = 5$  mrad, and therefore leads, according to equation 5.5, to the value of  $Q_{max}^2 = 10^{-2} \text{GeV}^2$ . Under the condition that  $\sigma_{\gamma p}$  is independent of  $W_{\gamma p}$ ,  $f_{\gamma/e}$  can be determined for a mean value  $\bar{W}$  within the  $y$  region selected for this analysis.

Combining equations 5.3 and 5.4 the photoproduction cross section for charm quarks is then obtained as follows:

$$\begin{aligned} \sigma(\gamma p \rightarrow c\bar{c}X) &= \frac{\sigma_{vis}(ep \rightarrow e'D^*X)}{\int f_{\gamma/e} dy \cdot 2B} \\ &= \frac{N^{obs}(K\pi\pi_s)}{\mathcal{L} \cdot \mathcal{A} \cdot \varepsilon_{rec} \cdot \varepsilon_{trig} \cdot 2BR(c \rightarrow K\pi\pi_s) \cdot \int f_{\gamma/e} dy}. \end{aligned} \quad (5.6)$$

$B(c \rightarrow D^{*\pm})$  denotes the fragmentation probability of a charm quark into a  $D^*$  meson<sup>1</sup>

## 5.2 Determination of the number of events

The number of  $D^*$  events is extracted by fitting the reweighted  $\Delta M$  distributions in various  $p_{\perp}$  and  $\hat{y}$  bins (chapter 4.5.1). For the ET at  $-33$  m as used for this analysis, the energy of the scattered electron is measured with good precision ( $\sigma(E)/E = 0.15/\sqrt{E/\text{GeV}} \oplus 0.01$  [65]) and the acceptance is well known, too. The acceptance of ET 33 does neither depend on the properties of the event, nor on  $Q^2$ , but is strongly correlated to  $y$  (Figure 4.6). To limit the values of the weights below or equal 5.0, the range of the inelasticity  $y$  of the proton is restricted to the central region of the ET, where the acceptance is larger than 0.2 ( $\mathcal{A}(ET) > 0.2 \Rightarrow w_i < 5.0$ , see also chapter 4.4.1).

### 5.2.1 Fitting technique

The sum of all data samples of the running periods 1994 up to 1996 contains enough events to divide the visible range into bins of  $p_{\perp}$  and  $\hat{y}$  and to measure differential

<sup>1</sup> $B(c \rightarrow D^{*-}) = 0$ , replace  $B(c \rightarrow D^*)$  with  $2B(c \rightarrow D^{*+})$ .

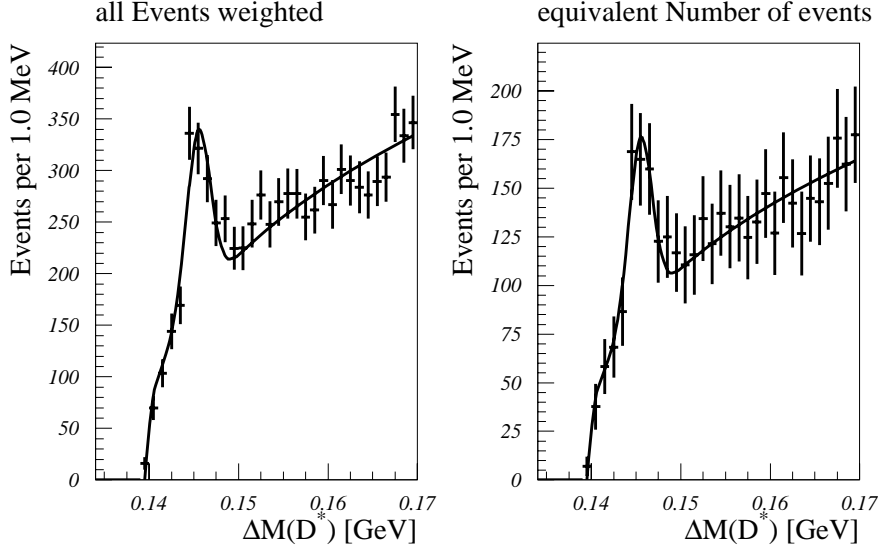


Figure 5.1: Fits to all selected events of ST 83, total and “Equivalent Number of Events”. The fits are performed with free peak width.

and double differential cross sections. To correctly propagate the statistical errors we use a technique known as “Equivalent Number of Events” [66]. This method applies to weighted histograms with small number of events, where neither Gaussian nor Poisson statistics is appropriate.

The statistical error of a sum of  $N$  weighted events with weights  $w_i$

$$\tilde{N} = \sum_{i=1}^N w_i \quad (5.7)$$

is given by

$$\delta \tilde{N} = \sqrt{\sum_{i=1}^N w_i^2}. \quad (5.8)$$

The equivalent number of events  $\bar{N}$  is then defined as the number of unweighted events having the same relative error as the sum of weights and therefore the same statistical significance. For sufficient large  $\bar{N}$  it is required to be Poisson distributed ( $\sigma(\bar{N}) = \sqrt{\bar{N}}$ ):

$$\frac{\delta \bar{N}}{\bar{N}} = \frac{1}{\sqrt{\bar{N}}} \equiv \frac{\delta \tilde{N}}{\tilde{N}} = \frac{\sqrt{\sum_{i=1}^N w_i^2}}{\sum_{i=1}^N w_i} \quad (5.9)$$

$$\frac{1}{\sqrt{\bar{N}}} = \frac{\sqrt{\sum_{i=1}^N w_i^2}}{\sum_{i=1}^N w_i} \Rightarrow \bar{N} = \frac{(\sum_{i=1}^N w_i)^2}{\sum_{i=1}^N w_i^2}. \quad (5.10)$$

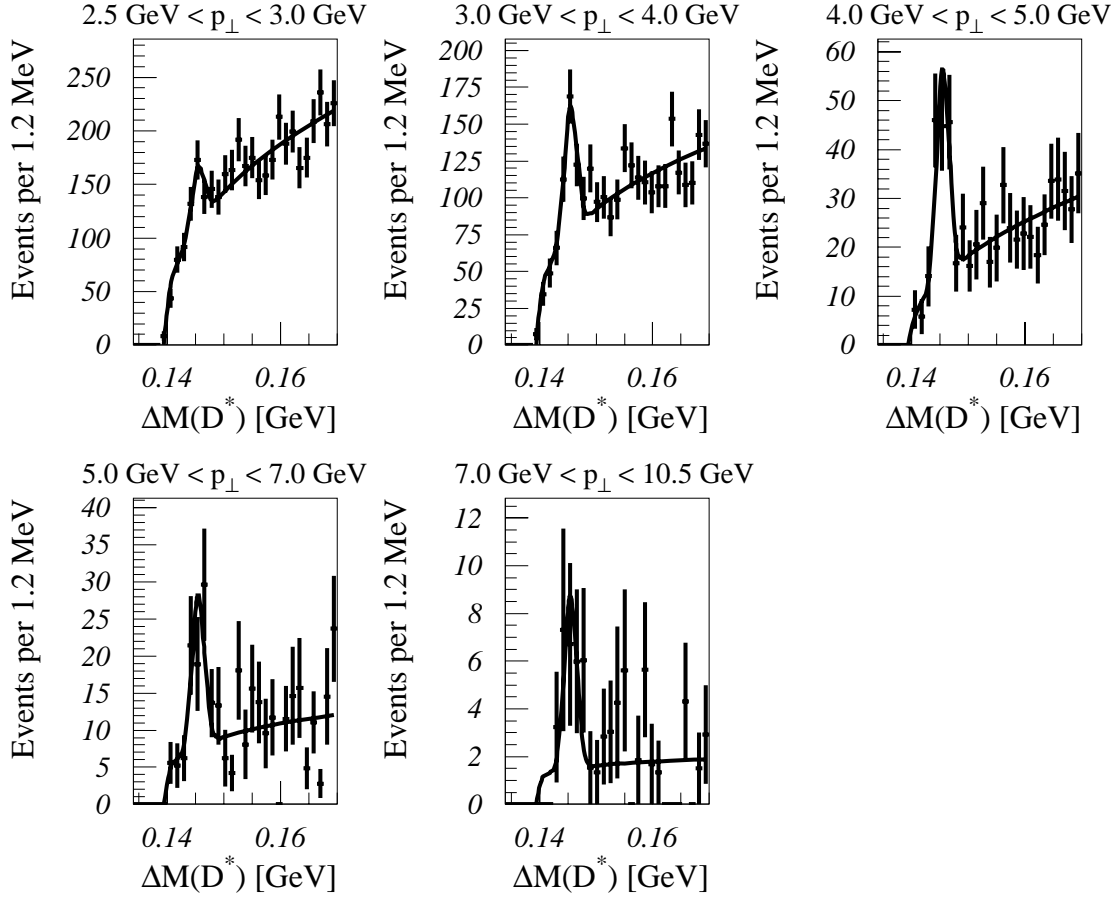


Figure 5.2: Fits to  $\Delta M$  in various bins of  $p_{\perp}$ , with fixed peak width, weighted sample

The histogram with  $\bar{N}$  events is now Poisson distributed and has the same statistical significance as the original histogram with  $N$  weighted events. The rescaling factor is given by

$$\frac{\tilde{N}}{\bar{N}} = \frac{\sum_{i=1}^N w_i^2}{\sum_{i=1}^N w_i}. \quad (5.11)$$

To perform a maximum likelihood fit for a given  $\Delta M$  distribution, the histogram is constructed according to 5.10, and after performing the fit the parameters have to be rescaled with the factor from 5.11.

## 5.2.2 Results of the fits

The reweighted  $\Delta M$  distributions are fit to the function (chapter 4.5.1, equation 4.9)

$$f(\Delta M) = \frac{N}{\sqrt{2\pi} \cdot \sigma} \cdot e^{-\frac{(\Delta M - \mu)^2}{2\sigma^2}} + A \cdot (\Delta M - m_{\pi})^b. \quad (5.12)$$

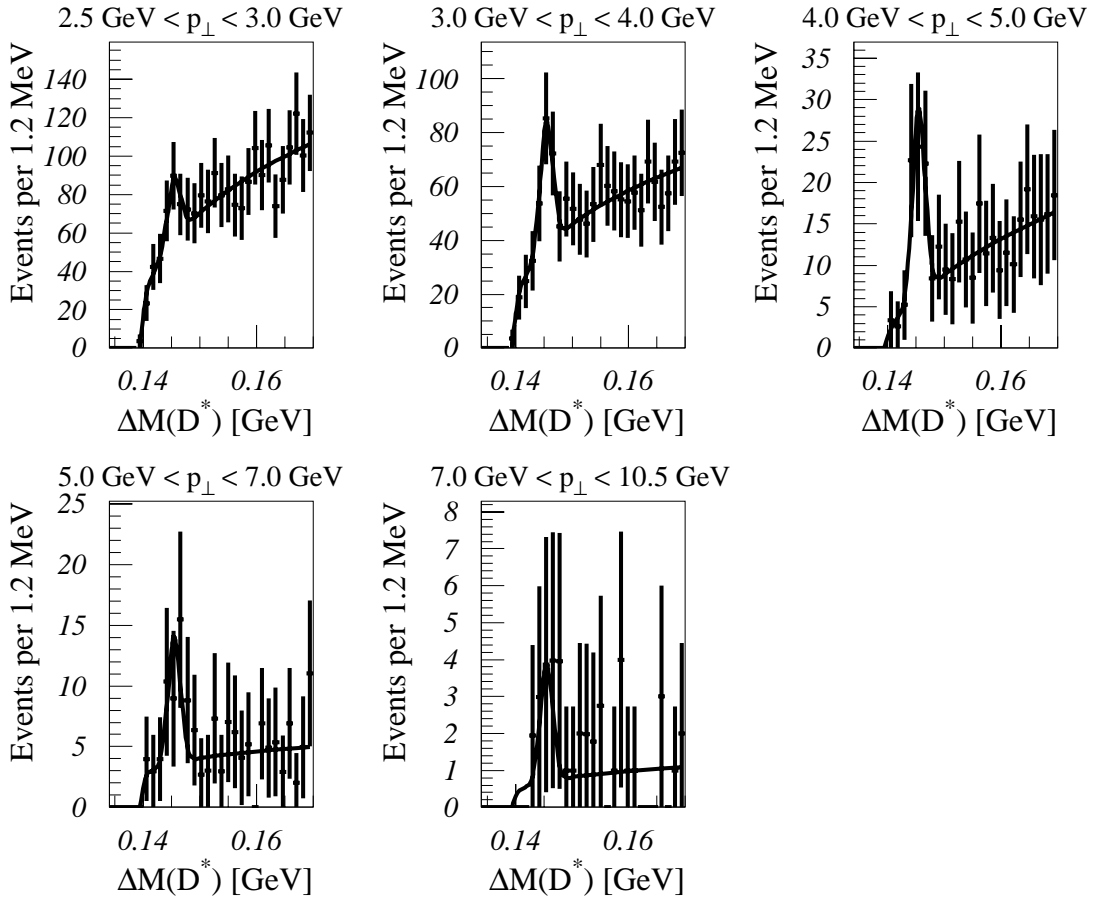


Figure 5.3: Fits to  $\Delta M$  in various bins of  $p_{\perp}$ , with fixed peak width, after reweighting the events by the method of “equivalent number of events”

i. e. the sum of a Gaussian for the signal and a polynomial for the background. In Figure 5.1 both the original and reweighted  $\Delta M$  distribution are shown. These histograms contain a sufficient number of events that four of the five free parameters in the function can be left free: the peak width ( $\sigma$ ), the exponent of background ( $b$ ), the number of background ( $A$ ) and  $D^*$  ( $N$ ) events. The peak position was fixed to get a better stability of the fit. However, when the position of the peak left open too in a fit to the  $\Delta M$  distribution from larger photoproduction sample with looser cuts the value  $\mu = 145.51 \pm 0.09$  MeV was found. This value is in good agreement with the accepted value of  $145.42 \pm 0.05$  MeV [64] and was therefore fixed at this value for all other fits. For the peak width the value of  $\sigma = 1.08 \pm 0.11$  MeV was found.

For the fits of the  $\Delta M$  distributions in bins of  $p_{\perp}$  and  $\hat{y}$  only three parameters were left free, namely the number of  $D^*$  events and background events, and the exponent of the background function, the peak width  $\sigma$  and the peak position  $\mu$  were fixed at the quoted values. Since the background is quite high, a simultaneous

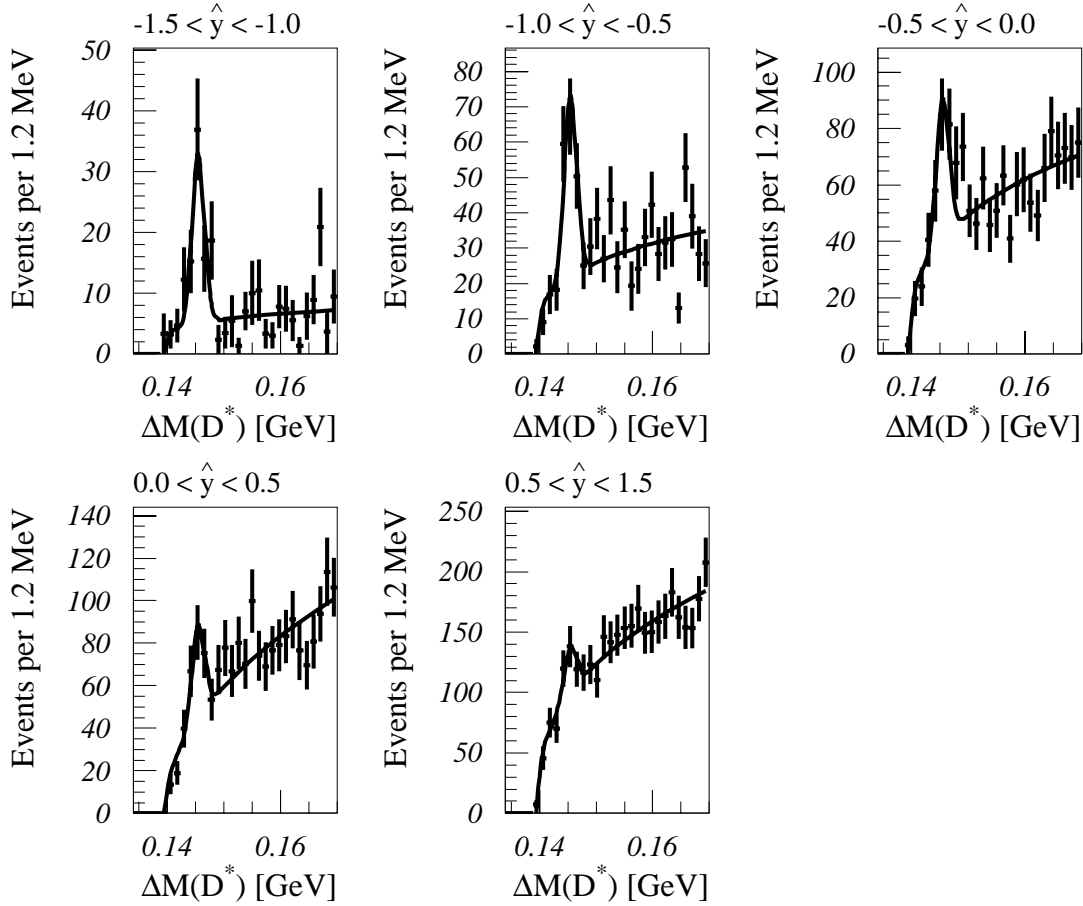


Figure 5.4: Fits to  $\Delta M$  in various bins of  $\hat{y}$ , with fixed peak width, weighted sample.

fit of all four parameters is unstable. To determine the systematic error of the fixed peak width the value of  $\sigma$  was varied by its error  $\delta\sigma$ . An overview of all fit results is given in Table 5.1, the corresponding curves and distributions are shown in Figures 5.3 and 5.5. For comparison, the weighted histograms before the rescaling are shown, too.

In earlier analyses [72] the combinatorial background of wrong sign combinations ( $D^{*\pm} \rightarrow (K^\mp \pi^\mp) \pi_s^\pm$ ) has been fitted separately, in order to determine the normalization of the background independently. The shape of the background is expected to be the same for both combinations, as has been argued in chapter 4.5.1. To reduce the data volume, wrong sign combinations have not been written to tape anymore since the running period 1995.

To get an estimate of the stability of the fit, all fits were redone with free peak width and also compared to Monte Carlo simulations. The agreement within the albeit large statistical errors is quite satisfactory. The simulations indicate that in higher  $p_\perp$  region, where no information from data can be obtained, no major change in the width is expected. Similar agreement is also observed for the different rapidity

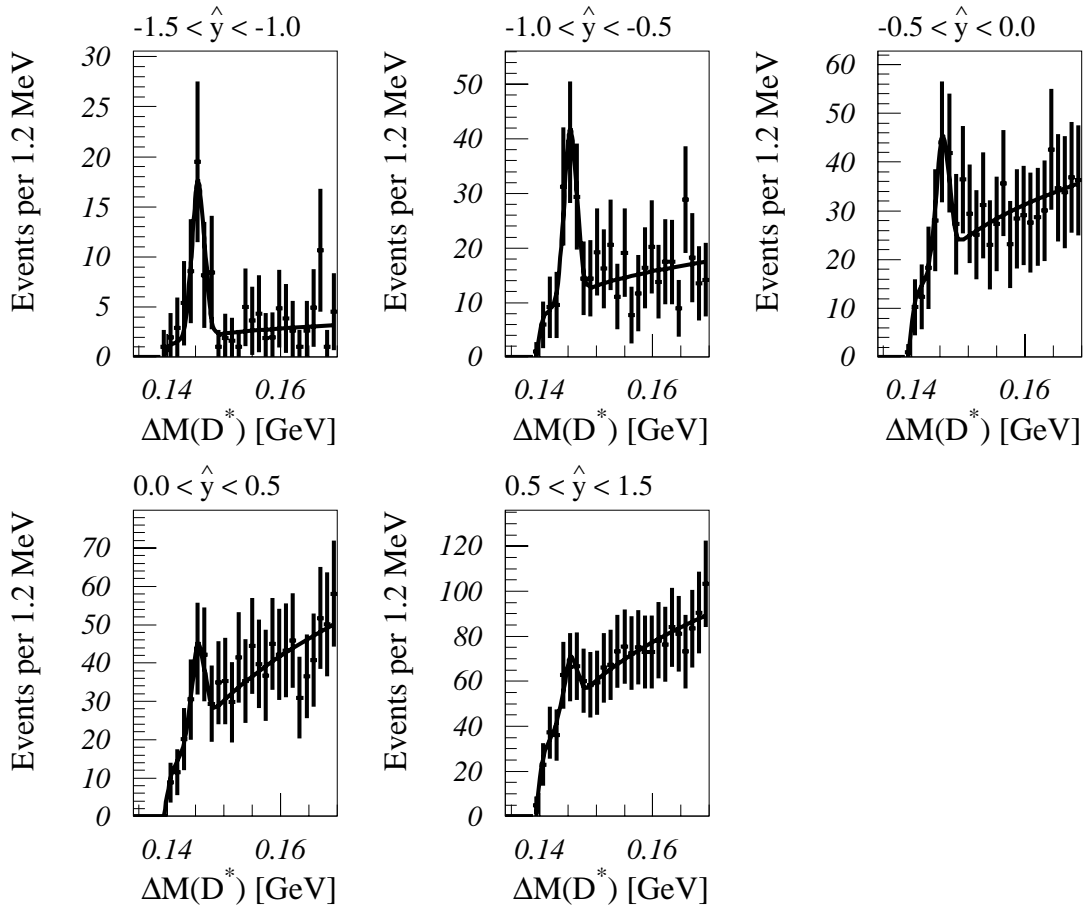


Figure 5.5: Fits to  $\Delta M$  in various bins of  $\hat{y}$ , with fixed peak width, after reweighting the events by the method of “equivalent number of events”.

bins. All values found are furthermore consistent with the average value chosen for the fits, which leads to the procedure chosen.

For the rapidity  $\hat{y}$  the fits converge in all bins, but the errors are too large to draw strong conclusions. A tendency can be seen at the edges towards bigger values of  $\sigma$ . The edge of  $\hat{y}$  corresponds to the edge of the acceptance. There it sometimes happens that a track does not cross both central drift chambers CJC’s (i.e. CJC2). This leads to a worse resolution of the track parameters. However, within the errors the fits with free peak width are consistent with the value of  $\sigma = 1.08 \pm 0.11$  MeV. To conclude, no variation found to be larger than the systematic error allows. Therefore, the procedure to keep the peak width fixed for all fits is justified.

| $p_{\perp} (D^*)$ in [GeV]<br>$\hat{y}$ dim. less | $\sigma = 1.08$ MeV      | $\sigma$ varied: $\delta\sigma = 0.12$ MeV |                           |
|---------------------------------------------------|--------------------------|--------------------------------------------|---------------------------|
|                                                   | events at $\bar{\sigma}$ | events at $+\delta\sigma$                  | events at $-\delta\sigma$ |
| $2.5 \leq p_{\perp} < 3.0$                        | 131 $\pm$ 18             | 139 $\pm$ 19                               | 120 $\pm$ 17              |
| $3.0 < p_{\perp} < 4.0$                           | 209 $\pm$ 17             | 218 $\pm$ 18                               | 197 $\pm$ 16              |
| $4.0 < p_{\perp} < 5.0$                           | 103 $\pm$ 9              | 107 $\pm$ 10                               | 98 $\pm$ 9                |
| $5.0 < p_{\perp} < 7.0$                           | 51 $\pm$ 7               | 54 $\pm$ 7                                 | 47 $\pm$ 6                |
| $7.0 < p_{\perp} \leq 10.5$                       | 11 $\pm$ 4               | 12 $\pm$ 4                                 | 9 $\pm$ 3                 |
| $-1.5 \leq \hat{y} < -1.0$                        | 76 $\pm$ 7               | 80 $\pm$ 7                                 | 72 $\pm$ 7                |
| $-1.0 < \hat{y} < -0.5$                           | 136 $\pm$ 11             | 140 $\pm$ 12                               | 131 $\pm$ 11              |
| $-0.5 < \hat{y} < 0.0$                            | 103 $\pm$ 12             | 110 $\pm$ 13                               | 96 $\pm$ 12               |
| $0.0 < \hat{y} < 0.5$                             | 100 $\pm$ 13             | 106 $\pm$ 13                               | 93 $\pm$ 12               |
| $0.5 < \hat{y} \leq 1.5$                          | 92 $\pm$ 17              | 97 $\pm$ 17                                | 85 $\pm$ 16               |

Table 5.1:  $\Delta M$ -fit results for cross section measurements in bins of  $p_{\perp}$  and  $\hat{y}$ . For systematic studies the fixed peak width is varied by its error.

| $p_{\perp}$ | 2.5 - 3.0       | 3.0 - 4.0       | 4.0 - 5.0       | 5.0 - 7.0       | 7.0 - 10.5      |
|-------------|-----------------|-----------------|-----------------|-----------------|-----------------|
| data        | $1.27 \pm 0.38$ | $0.99 \pm 0.18$ | $1.11 \pm 0.22$ | $1.72 \pm 0.49$ | —               |
| MC          | $0.84 \pm 0.04$ | $0.96 \pm 0.04$ | $0.99 \pm 0.06$ | $1.01 \pm 0.10$ | $0.79 \pm 0.12$ |

Table 5.2: Peak width  $\sigma$  of  $p_{\perp}$  fits in data and MC.  $p_{\perp}$  units are [GeV], the units of  $\sigma$  are [MeV].

### 5.3 Acceptance and efficiencies

In this section the efficiency calculations are described in detail. The exact corresponding tables are given in the appendix (Tables A.1 and A.2).

#### 5.3.1 The method used for efficiency determination

For cross section measurement the real number of produced  $D^*$  mesons in the visible range  $N_{true}^{D^*}$  is needed. The number of  $D^*$  mesons which are really measured and reconstructed with the H1-detector  $N_{obs}^{D^*}$  is only a small fraction of the events produced in reality, because  $D^*$  mesons are lost due to several reasons:

| $\hat{y}$ | -1.5 - -1.0     | -1.0 - -0.5     | -0.5 - 0.0      | 0.0 - 0.5       | 0.5 - 1.5       |
|-----------|-----------------|-----------------|-----------------|-----------------|-----------------|
| data      | $1.31 \pm 0.22$ | $1.05 \pm 0.15$ | $1.40 \pm 0.58$ | $1.17 \pm 0.36$ | $1.15 \pm 0.41$ |
| MC        | $1.07 \pm 0.06$ | $0.92 \pm 0.05$ | $0.86 \pm 0.04$ | $0.87 \pm 0.08$ | $0.84 \pm 0.07$ |

Table 5.3: Peak width  $\sigma$  of  $\hat{y}$  fits in data and MC.  $\hat{y}$  is dimensionless, the units of  $\sigma$  are [MeV].

- The event is rejected by the trigger prescale.
- The event has not been triggered.
- One of the decay particles of the  $D^*$  meson falls outside the acceptance of the central jet chamber.
- One of the decay particles does not fulfill one of the analysis cuts (e.g.  $p_{\perp}$  is too small).
- All decay particles enter the main detector (CJC), but at least one of them was not reconstructed.

While the prescale of the trigger is absorbed in the luminosity correction, the trigger efficiency still needs to be determined. The acceptance of the electron tagger is taken into account by the event weights and needs no further investigation, whereas the acceptance of the central jet chamber CJC must be calculated separately. The same is true for the reconstruction efficiency of CJC.

The acceptance and efficiency correction were determined using a Monte Carlo event sample. The efficiency for the direct and the resolved part is not the same due to their different kinematics. Therefore two different MC samples are used. For the direct part, the MC generator AROMA 2.2 [56] was used, while the resolved part was produced by the generator PYTHIA 5.7 [57, 61]. AROMA is a leading order MC generator, using leading order matrix elements of parton shower (see also chapter 4.1.1). After the separate calculation of the efficiencies for the direct and the resolved part, they are added up according to the predicted mixing ratio of the two processes [63]. This has to be done for the visible and the full kinematical range and for each bin of the differential and double differential cross sections. Therefore the mixing ratio was extracted for every bin separately.

The total efficiency is given as follows, where *gen* stands for generated MC <sup>2</sup> and *rec* for simulated and reconstructed MC:

$$\begin{aligned}
\epsilon_{tot} &= \frac{N_{obs}^{D^*}}{N_{true}^{D^*}} = \frac{N_{rec}^{D^*}(\text{all rec cuts, TE})}{N_{gen}^{D^*}} = \\
&= \frac{N_{gen}^{D^*}(\text{all gen cuts})}{N_{gen}^{D^*}} \times \frac{N_{rec}^{D^*}(\text{all rec cuts})}{N_{gen}^{D^*}(\text{all gen cuts})} \times \frac{N_{rec}^{D^*}(\text{all rec cuts, TE})}{N_{rec}^{D^*}(\text{all rec cuts})} \\
&= \mathcal{A} \times \epsilon_{Reconstr.} \times \epsilon_{Trigger}, \tag{5.13}
\end{aligned}$$

where *gen cuts* stands for all cuts on generator level to restrict the MC sample to the visible range of H1 (i.e. cuts on  $p_{\perp}(D^*)$ ,  $\hat{y}(D^*)$ ,  $\vartheta(\text{decay particles})$ ,  $p_{\perp}(\text{decay particles}), y, Q^2$ ) and *rec cuts* stand for all analysis cuts as described in chapter 4. The trigger elements TE are defined in chapter 4. According to equation 5.13 the total efficiency can be split into the acceptance  $\mathcal{A}$ , the reconstruction efficiency  $\epsilon_{rec}$  and the trigger efficiency  $\epsilon_{trig}$ , which can be calculated separately.

---

<sup>2</sup>Generated MC events stands for events out of the generator, which are not effected by the H1 detector simulation, in opposite to simulated and reconstructed MC.

### 5.3.2 Acceptance corrections

The decay particles of the  $D^*$  meson need to fulfill the selection cuts ( $p_{\perp}(\pi_s) < 150$  MeV,  $p_{\perp}(K, \pi) < 500$  MeV,  $20^\circ < \vartheta_{track} < 160^\circ$ ) depending on the detector geometry ( $\vartheta$ ) and on the resolution of the CJC ( $p_{\perp}$ ). Here only the kinematics is needed, which is well described in the generator. The acceptance is then given by

$$\mathcal{A} = \frac{N_{D^*}^{gen}(p_{\perp}(D^*), \hat{y}(D^*), \vartheta(K, \pi, \pi_s), p_{\perp}(K, \pi, \pi_s), y, Q^2)}{N_{D^*}^{gen}(p_{\perp}(D^*), \hat{y}(D^*), y, Q^2)}. \quad (5.14)$$

Table 5.4 lists the values found for the single inclusive cross sections. The acceptance did not change during the whole data taking period. The dependence of the acceptance on the choice of parameters in the MC generator, as for example  $m_c$  or  $g(x)$ , were studied in [72] and found to be negligible.

|                              |                |                |                |                |                |
|------------------------------|----------------|----------------|----------------|----------------|----------------|
| $p_{\perp}$ [GeV]            | 2.5 - 3.0      | 3.0 - 4.0      | 4.0 - 5.0      | 5.0 - 7.0      | 7.0 - 10.5     |
| $\mathcal{A}(p_{\perp})[\%]$ | $50.5 \pm 0.7$ | $67.0 \pm 0.7$ | $76.5 \pm 0.9$ | $86.3 \pm 1.0$ | $90.8 \pm 1.4$ |
| $\hat{y}$                    | -1.5 - -1.0    | -1.0 - -0.5    | -0.5 - 0.0     | 0.0 - 0.5      | 0.5 - 1.5      |
| $\mathcal{A}(\hat{y})[\%]$   | $48.8 \pm 0.8$ | $69.7 \pm 0.7$ | $73.9 \pm 0.8$ | $74.4 \pm 1.1$ | $66.9 \pm 1.4$ |

Table 5.4: *Detector acceptance corrections, calculated with a generated MC sample (AROMA 2.2).*

### 5.3.3 Reconstruction efficiencies

The track reconstruction depends crucially on a correct description of the central jet chamber in the detector simulation and needs to be checked against data. Important quantities to monitor the detector performance are the number of hits per track (e.g. influenced by dead drift cells), the radial track length  $R_{length}$  and the distance of closest approach  $DCA$ . The checks were done for  $K$ ,  $\pi$  and  $\pi_s$  separately.

#### Dead drift cells

Due to hardware problems in the jet chamber, some drift cells have not been fully operational in certain periods of the data taking. This causes inefficiencies of the detector at the corresponding position in  $\varphi$  and leads to a worse track measurement. Inefficiencies of drift cells or single wire efficiencies are accounted for the detector simulation by producing a single wire efficiency map for every interval between major changes at the end of every running period using real data. Figure 5.6 shows the number of hits per track versus  $\varphi$  for all running periods used in this analysis. After tuning the 1996 data, a good agreement is found between real data and detector simulation. The changes from year to year can be seen clearly.

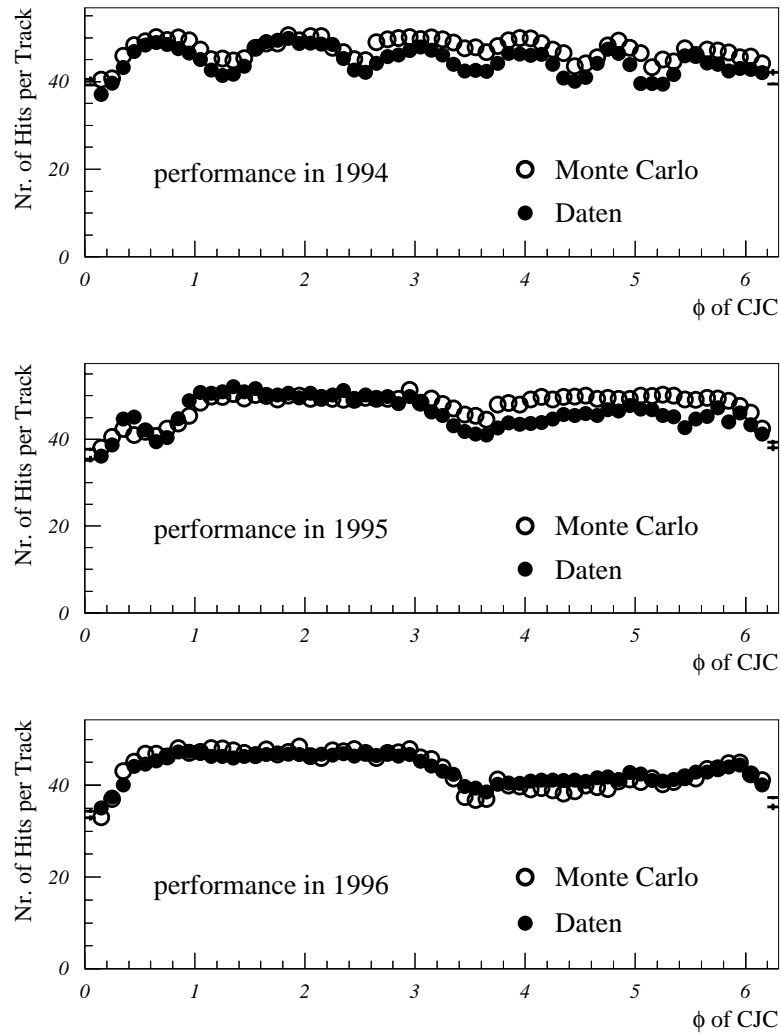


Figure 5.6: Performance of CJC for the years 1994 - 1996, showing hits per track versus  $\phi$ .

### Distance of closest approach and radial track length

In Figures 5.7 - 5.9 the distributions of the radial track length and the DCA for data and simulated MC events are shown. The radial track length is the difference of the radii of the first and last hit of the track measured. These distributions peak at 20 cm and 60 cm, corresponding to the radial dimensions of the inner CJC (CJC1) and both chambers (CJC1 + CJC2). Also a good agreement of data and MC is found, which lets us believe that the chamber efficiency is treated correctly in the simulation. For the following control plots the cuts are relaxed compared to those used in the main analysis.

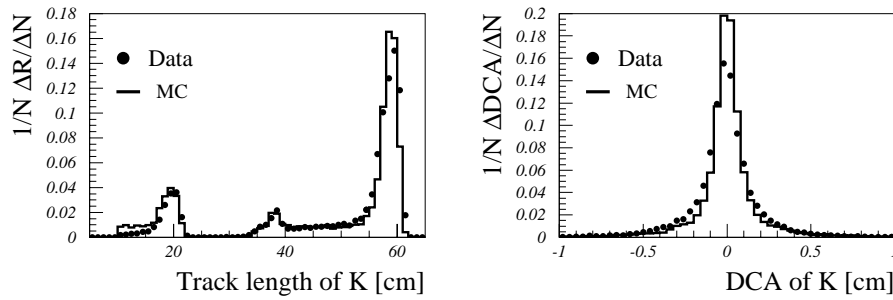


Figure 5.7: *Distribution of radial track length  $R_{length}$  and distance of closest approach DCA of  $K$ , comparison of data and MC*

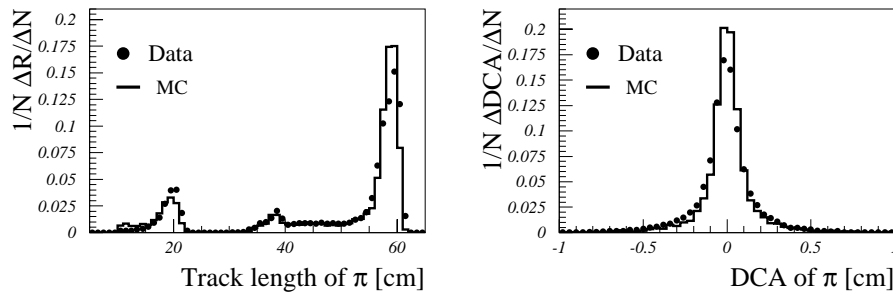


Figure 5.8: *Distribution of radial track-length  $R_{length}$  and distance of closest approach DCA of  $\pi$ , comparison of data and MC.*

### Efficiency determination

The reconstruction efficiency is determined for the direct and the resolved processes (see chapter 4.1), using

$$\epsilon_{rec} = \frac{N_{D^*}^{rec}(\text{all analysis cuts}, \delta(\Delta M))}{N_{D^*}^{gen}(p_{\perp}(D^*), \hat{y}(D^*), \vartheta(\text{tracks}), p_{\perp}(K, \pi, \pi_s), y, Q^2)}. \quad (5.15)$$

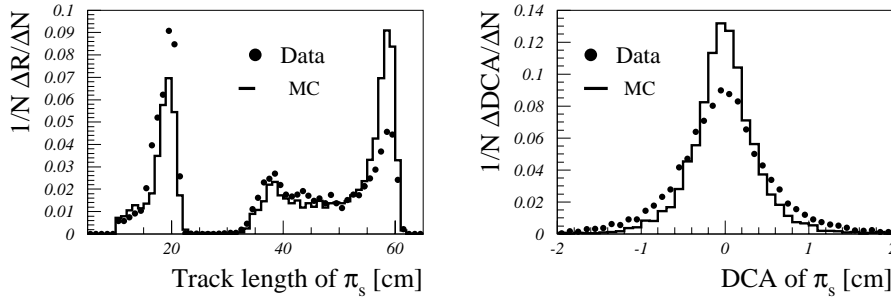


Figure 5.9: *Distribution of radial track-length  $R_{length}$  and distance of closest approach DCA of  $\pi_s$ , comparison of data and MC*

In a second step the final efficiency is obtained by averaging the results weighted with the mixing ratio for both contributions bin-wise:

$$\epsilon_{tot; rec}^{bin\ i} = w_{dir}^{bin\ i} \times \epsilon_{dir; rec}^{bin\ i} + w_{res}^{bin\ i} \times \epsilon_{res; rec}^{bin\ i}. \quad (5.16)$$

The weights are given via the number of MC events found in the corresponding bin. In the visible range the direct and the resolved contribution are predicted [63] to be 93 % and 7 % respectively. The efficiency is repeated for every year separately. The 1996 results are given in Table 5.5.

|                                 |                |                |                |                |                |
|---------------------------------|----------------|----------------|----------------|----------------|----------------|
| $p_{\perp}$ [GeV]               | 2.5 - 3.0      | 3.0 - 4.0      | 4.0 - 5.0      | 5.0 - 7.0      | 7.0 - 10.5     |
| $\epsilon_{rec}(p_{\perp})$ [%] | $76.5 \pm 2.7$ | $79.0 \pm 2.2$ | $76.3 \pm 3.6$ | $76.4 \pm 5.0$ | $81.0 \pm 7.1$ |
| $\hat{y}$                       | -1.5 - -1.0    | -1.0 - -0.5    | -0.5 - 0.0     | 0.0 - 0.5      | 0.5 - 1.5      |
| $\epsilon_{rec}(\hat{y})$ [%]   | $68.3 \pm 3.4$ | $80.5 \pm 2.4$ | $81.6 \pm 2.7$ | $79.4 \pm 4.4$ | $76.9 \pm 4.6$ |

Table 5.5: *Reconstruction efficiencies 1996 calculated with simulated MC data samples separately for direct and resolved events.*

### 5.3.4 Trigger efficiency

The photoproduction subtrigger used for the present analysis consists of several trigger elements as was described in Chapter 4.2.1. In principle all trigger elements (TE) have to be analyzed separately. The efficiency of the ET is absorbed in the acceptance and needs no further investigations. The zVtx\_T0 inefficiency can be neglected, as confirmed by previous analyses within the collaboration [73]. The effect of the veto conditions on heavy quark events is also very small. The z-vertex and drift chamber trigger elements zVtx\_sig and DCr $\varphi$ \_Tc, respectively, remain to be investigated:

- zVtx\_sig: significant peak in the z-vertex histogram

- DCr $\varphi$ -Tc: at least three track candidates in CJC

We define the trigger efficiency as:

$$\epsilon_{trig}(TE(i)) = \frac{N_{D^*}^{rec}(\text{all analysis cuts}, \delta(\Delta M)) \times TE(i)}{N_{D^*}^{rec}(\text{all analysis cuts}, \delta(\Delta M))}. \quad (5.17)$$

and determine it using simulated data, too, as it was done for the reconstruction efficiency. The trigger part of the detector simulation is carefully tuned to describe the data as well as possible and can be reliably used for the determination of the trigger efficiency [73, 69, 74, 75]. The results from the 1996 run are given in Table 5.6 as an example:

|                                  |                |                |                |                |                |
|----------------------------------|----------------|----------------|----------------|----------------|----------------|
| $p_{\perp}$ [GeV]                | 2.5 - 3.0      | 3.0 - 4.0      | 4.0 - 5.0      | 5.0 - 7.0      | 7.0 - 10.5     |
| $\epsilon_{trig}(p_{\perp})[\%]$ | $87.4 \pm 2.2$ | $88.4 \pm 1.9$ | $88.1 \pm 3.0$ | $82.5 \pm 4.7$ | $83.1 \pm 6.6$ |
| $\hat{y}$                        | -1.5 - -1.0    | -1.0 - -0.5    | -0.5 - 0.0     | 0.0 - 0.5      | 0.5 - 1.5      |
| $\epsilon_{trig}(\hat{y})[\%]$   | $83.8 \pm 3.2$ | $89.5 \pm 2.1$ | $88.8 \pm 2.2$ | $84.8 \pm 4.1$ | $85.3 \pm 3.8$ |

Table 5.6: *Trigger efficiencies for 1996, calculated with simulated MC data samples, separately for direct and resolved events.*

If an independent monitor trigger exists, the trigger efficiencies can in principle be obtained from  $ep$  data. This was done using the 1996 data for the drift chamber and the  $z$ -Vertex trigger elements. A good agreement with the efficiency obtained from monte carlo was found within 3 %. This could not be applied for the 1995 data, because the necessary monitor triggers were downscaled by large factors to reduce deadtime, and hence the available event sample was too small. The photoproduction trigger did not change from 1995 to 1996 and the cross check for 1996 was done successfully, therefore the trigger efficiency could be determined for the whole period of this analysis from the corresponding monte carlo samples. Several analyses within our collaboration exist however, where these comparisons have confirmed the results obtained for the simulation [73, 76].

## 5.4 Systematic studies

We considered the following possible sources of experimental errors:

- proper simulation of the drift chamber trigger [69],
- proper simulation of the  $z$ -Vertex (proportional chamber) trigger [73],
- track reconstruction [67],
- acceptance of the electron tagger [52],

- luminosity measurement [65],
- variation of the  $D^*$ -peak width (see Chapter 5.2.2),
- decay branching ratios [64].

These errors are listed in Table 5.7. References to other analyses within our collaboration are given above, where appropriate.

| experimental systematic errors                |                  |
|-----------------------------------------------|------------------|
| track triggers                                | 5 %              |
| track reconstruction                          | +9%<br>-0%       |
| ET - acceptance                               | 5 %              |
| luminosity measurement                        | 1.5 %            |
| width of $D^*$ -signal                        | +5.6%<br>-7.4%   |
| $D^*$ , $D^0$ branching ratios                | 4 %              |
| $\bar{c}c \rightarrow D^*$ branching fraction | 7 %              |
| total experimental uncertainty                | +15.2%<br>-13.1% |

Table 5.7: *Experimental systematic errors*

A source of theoretical uncertainties is the predicted ratio of direct and resolved processes. It is a theoretical input and therefore sensitive to the choice of the photon structure function, which is chosen as GRV [32] for the present analysis. This choice delivers a mixing ratio of 90 % to 10 % of direct and resolved fraction. If the photon structure function is changed to the LAC1 [31] calculation, the mixing ratio changes to (80 %/20 %) for *dir/res*. This influences the efficiencies on the per cent level: the mean values of the trigger efficiency are about 5 % lower, whereas the reconstruction efficiencies agree within the statistical errors.

## 5.5 Raw Data Spectras

Figure 5.10 presents the comparison of the raw data spectra to the reconstructed Monte Carlo event sample used for the acceptance and efficiency corrections as a function of the transverse momentum  $p_{\perp}$  and the rapidity  $\hat{y}$ . The errors shown are statistical only, the systematic errors of the order of  $\mathcal{O}(14\%)$  are not shown. Within the errors a good agreement of data and Monte Carlo can be found.

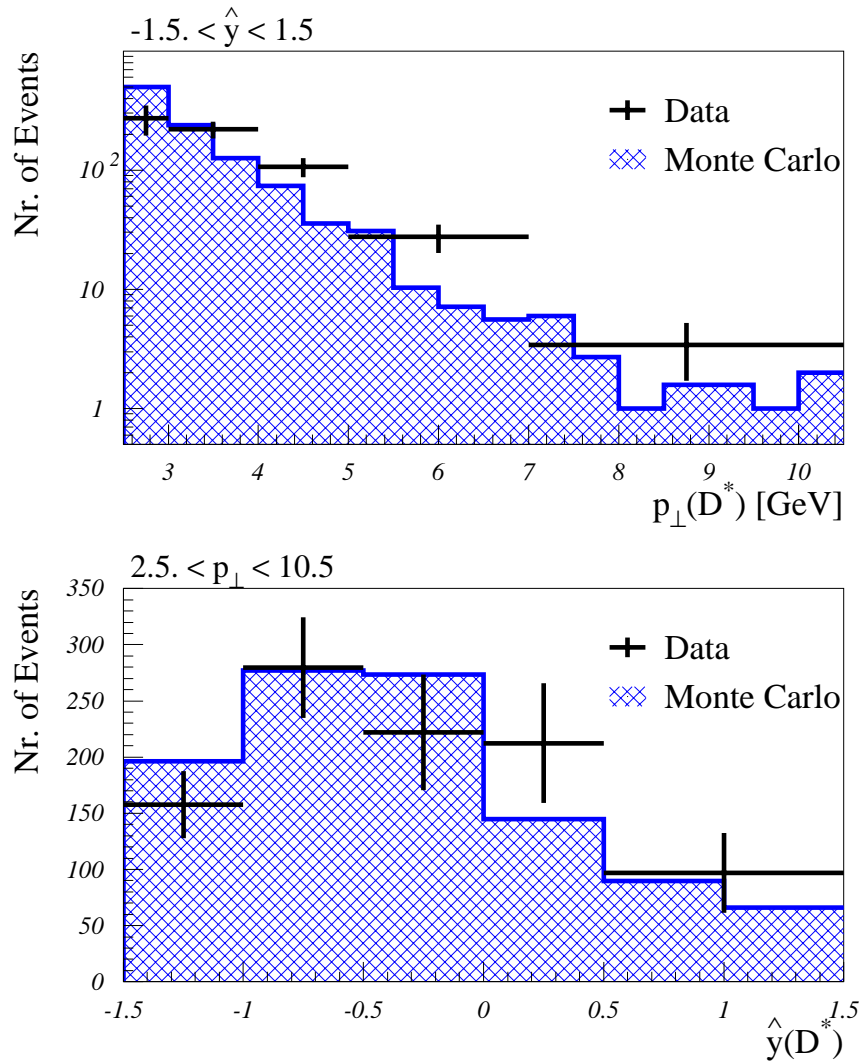


Figure 5.10: Comparison of the raw  $p_{\perp}$  and  $\hat{y}$  spectras to reconstructed Monte Carlo (AROMA + IJRAY)

## 5.6 The total cross section $\sigma(\gamma p \rightarrow c\bar{c}X)$

Recalling equation 5.6, the visible cross section for the kinematical range of  $p_t(D^*) > 2.5$  GeV/c in transverse momentum and  $|\hat{y}(D^*)| < 1.5$  for rapidity is given by:

$$\sigma(ep \rightarrow e'D^{*\pm}X) = \sigma(ep \rightarrow e'D^{*+}X) + \sigma(ep \rightarrow e'D^{*-}X) = \frac{N^{obs}(K\pi\pi_s)}{\mathcal{L} \cdot BR \cdot \epsilon} \quad (5.18)$$

The combined branching ratio for the decay of  $D^*$  and  $D^0$  mesons is  $BR = (0.0273 \pm 0.0011)$  [64]. The total number of events is measured after ET correction as  $N^{obs}(K\pi\pi_s) = (636 \pm 36)$ , and the total efficiency as  $\epsilon = 44.84 \pm 0.65$  %. For the kinematical region of photoproduction ( $\langle W_{\gamma p} \rangle = 198$  GeV,  $Q^2 < 0.01$  GeV<sup>2</sup>) the *visible*  $ep$  production cross section is determined to be

$$\sigma(ep \rightarrow e'D^{*\pm}X) = (4.30 \pm 0.35_{-0.56}^{+0.66})nb, \quad (5.19)$$

where the first error is the statistical one and the second the experimental systematic error.

To obtain the total cross section  $\sigma(\gamma p \rightarrow c\bar{c}X)$ , the visible cross section has to be extrapolated to the full phase space in  $p_\perp$  and  $\hat{y}$ . The acceptance to the full range is given by the fraction of  $D^*$  mesons within the visible range and the total number of  $D^*$  produced and is determined with NLO QCD calculations.

| proton<br>parton density | photon<br>parton density | $m_c$<br>[GeV/c <sup>2</sup> ] | acceptance<br>% |
|--------------------------|--------------------------|--------------------------------|-----------------|
| GRV LO [71]              |                          | 1.2                            | 4.8             |
| GRV LO [71]              |                          | 1.5                            | 6.3             |
| GRV LO [71]              |                          | 1.8                            | 10.8            |
| MRSB [62]                |                          | 1.5                            | 6.7             |
| MRSB' [70]               |                          | 1.5                            | 6.7             |
| GRV LO [71]              | GRV LO [71]              | 1.5                            | 2.1             |
| GRV LO [71]              | LAC 1 [31]               | 1.5                            | 2.1             |

Table 5.8: *Acceptance for direct and resolved contributions for the extrapolation from the visible to the total range using different parton density parameterizations and for different charm quark masses [72].*

The acceptance is different for direct and resolved processes and depends on the choice of the parton densities and the charm quark mass. In Table 5.8 an overview of different calculations is given. For the extrapolation of our measurement, the GRV LO parameterizations for the proton and the photon are used [71] with a charm quark mass of 1.5 GeV/c<sup>2</sup>, which gives a 79 % direct and a 21 % resolved contribution for the full  $p_\perp$  and  $\hat{y}$  range.

The choice of the parameterization is motivated by the measurement of the differential cross sections shown in the following chapter. GRV LO represents our data points best. Dividing by the photon flux factor ( $f_{\gamma/e} = 0.0127$ ) and the fragmentation fraction ( $B(c \rightarrow D^*) = (0.260 \pm 0.021)$  [68]) we obtain for the total charm production cross section

$$\sigma(\gamma p \rightarrow c\bar{c}X) = (12.02 \pm 1.29_{-1.58}^{+1.83})\mu b. \quad (5.20)$$

The errors are the same as before. This is in good agreement with earlier measurements with the 1994 data only [72] ( $\sigma(\gamma p \rightarrow c\bar{c}X)_{1994} = (13.2 \pm 2.2_{-1.7}^{+2.6})\mu b$ ).

## 5.7 Differential cross sections

Figures 5.11, 5.12 and 5.13 show the single and double differential cross sections, respectively, for the various bins in  $p_{\perp}$  and  $\hat{y}$ . Tables 5.9 and 5.10 just list the results for the single differential cross sections, since all ingredients and formulas for the calculation have been given above. The values of the measurement of the double differential cross sections are given in the appendix (Table A.3). The common systematic errors as determined in Table 5.7 at the order of  $\mathcal{O}(14\%)$  are not shown in all following distributions.

In the next chapter the data are compared to different Monte Carlo generators and to next to leading order QCD calculations. The theoretical models can be tested by using different sets of parton density functions, by varying the fragmentation function and the charm mass and the fragmentation approach.

|                                          |                   |                  |                 |
|------------------------------------------|-------------------|------------------|-----------------|
| $p_{\perp}$ [GeV]                        | 2.5 - 3.0         | 3.0 - 4.0        | 4.0 - 5.0       |
| $d\sigma_{\gamma p}/dp_{\perp}$ [nb/GeV] | $356.5 \pm 104.1$ | $203.7 \pm 33.1$ | $86.6 \pm 15.9$ |
| $p_{\perp}$ [GeV]                        | 5.0 - 7.0         | 7.0 - 10.5       |                 |
| $d\sigma_{\gamma p}/dp_{\perp}$ [nb/GeV] | $19.5 \pm 5.5$    | $2.4 \pm 1.4$    |                 |

Table 5.9: Result of the measurement of the single differential cross section  $d\sigma_{\gamma p}/dp_{\perp}$  as function of  $p_{\perp}$

|                                    |                  |                  |                  |
|------------------------------------|------------------|------------------|------------------|
| $\hat{y}$                          | -1.5 - -1.0      | -1.0 - -0.5      | -0.5 - 0.0       |
| $d\sigma_{\gamma p}/d\hat{y}$ [nb] | $234.6 \pm 46.5$ | $251.9 \pm 41.1$ | $179.6 \pm 42.4$ |
| $\hat{y}$                          | 0.0 - 0.5        | 0.5 - 1.5        |                  |
| $d\sigma_{\gamma p}/d\hat{y}$ [nb] | $176.4 \pm 45.1$ | $97.2 \pm 36.7$  |                  |

Table 5.10: Results of the measurement of the single differential cross section  $d\sigma_{\gamma p}/d\hat{y}$  as function of  $\hat{y}$

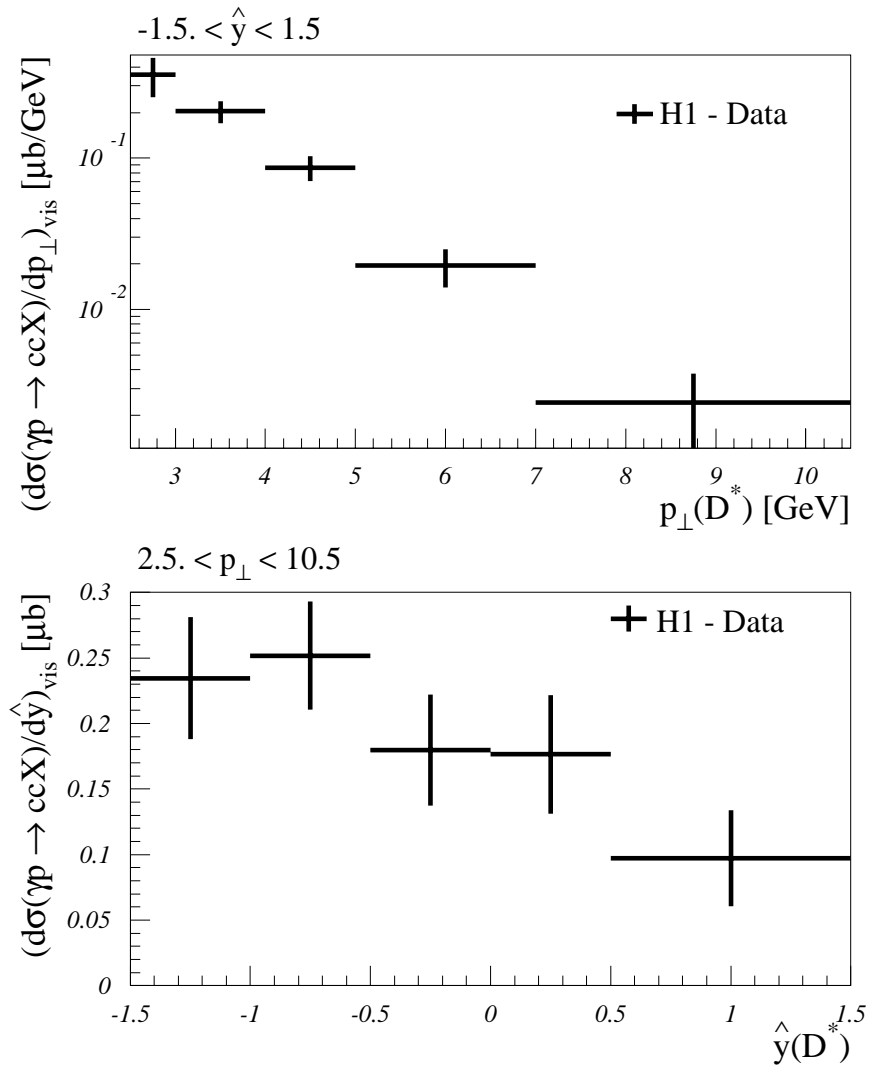


Figure 5.11: Single differential cross section in function of  $p_{\perp}$  and  $\hat{y}$ .

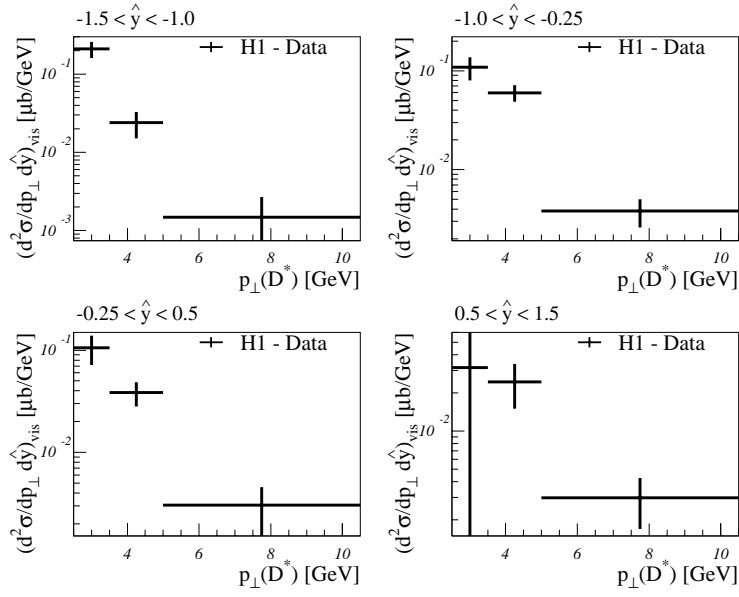


Figure 5.12: *Double differential Cross Sections as function of  $p_{\perp}$  for different  $\hat{y}$  regions.*

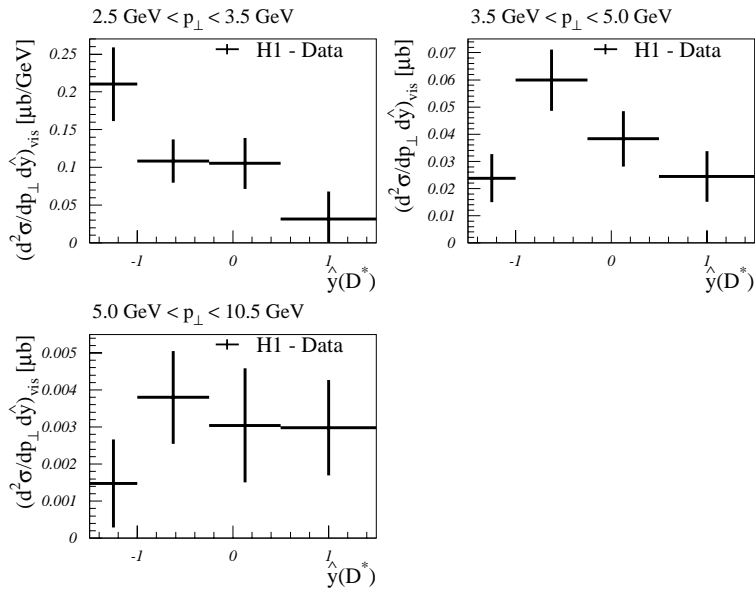


Figure 5.13: *Double differential cross Sections as function of  $\hat{y}$  for different  $p_{\perp}$  regions.*

# Chapter 6

## Comparison to theory

In the previous chapter we discussed how the charm photoproduction cross sections were measured. Now we compare the results to predictions of different Monte Carlo generators and the next to leading order theoretical calculations (“massive” and “massless”) described in Chapter 2.

### 6.1 Comparison to Monte Carlo generators

The measured charm cross sections are compared to those predictions by the AROMA-IJRAY and the HERWIG Monte Carlo generators, which differ mainly in the treatment of the resolved part of the process and in the treatment of the fragmentation and hadronization. Since we are mainly interested in a test of the theoretical prediction of the generators, and the higher order calculations, we can do this comparison at the generator level.

#### 6.1.1 AROMA-IJRAY

The generators AROMA [55, 56] and IJRAY [58, 59] have been described already in chapter 4.1.1. The cross sections were calculated separately for the direct (AROMA) and the resolved (IJRAY) process and then added. Figure 6.1 presents the single differential charm photoproduction cross sections as a function of the transverse momentum  $p_{\perp}$  and the rapidity  $\hat{y}$ . Because AROMA contains only leading order matrix elements, the cross section is clearly underestimated. The resolved contribution increases for the forward direction ( $\hat{y} > 0$ ) as can be seen in the rapidity distribution of Figure 6.1. The predicted shape is in good agreement with the data, as was already evident in the acceptance studies shown earlier (Figure 5.10).

The shapes of the double differential cross sections (Figure 6.2) are also in good agreement, even at low  $p_{\perp}$  where the resolved part is important. The underestimation of the cross sections indicates the need for important contributions beyond leading order QCD corrections (NLO QCD).

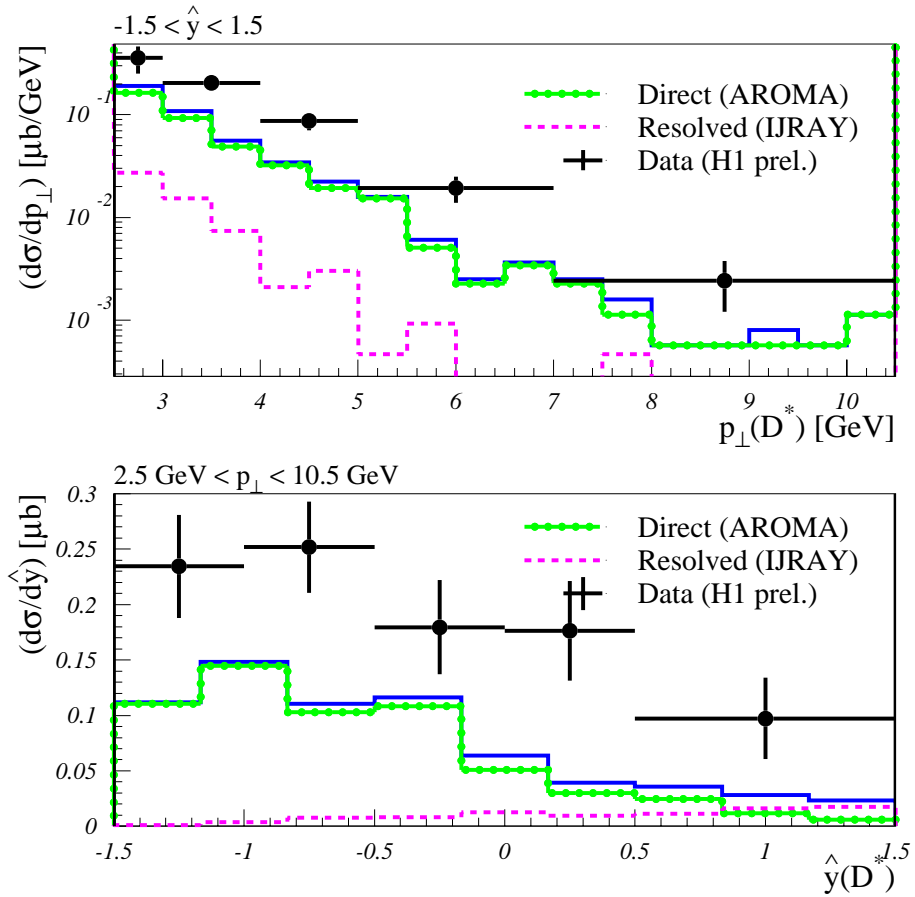


Figure 6.1: Single differential cross section  $d\sigma/dp_{\perp}, d\sigma/d\hat{y}$  as function of  $p_{\perp}$  and  $\hat{y}$  in comparison with the predictions of the AROMA/IJRAY generator. The direct and resolved part are shown separately.

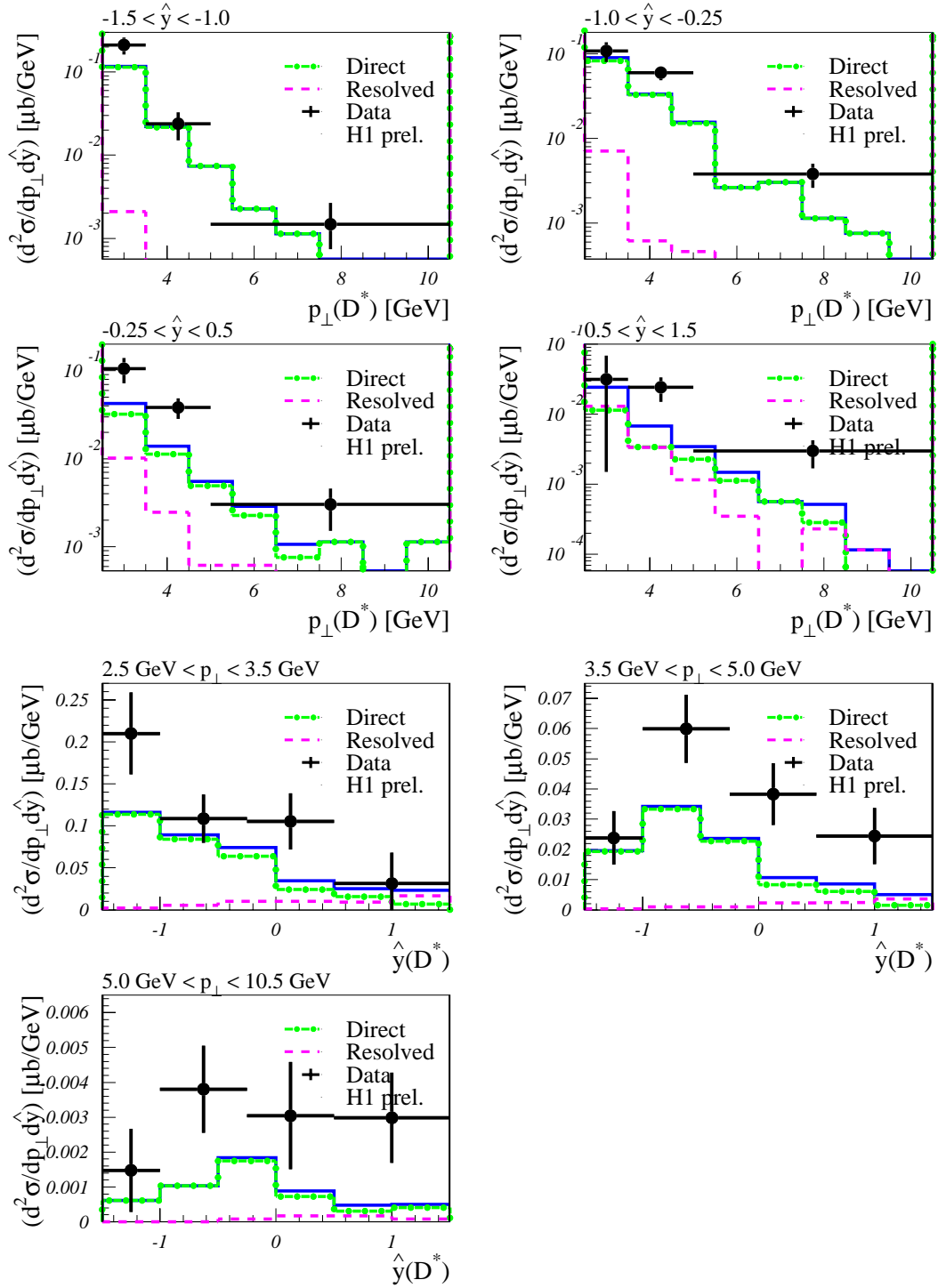


Figure 6.2: Double differential cross section  $d^2\sigma/dp_{\perp}d\hat{y}$  in regions of  $p_{\perp}$  and  $\hat{y}$ , compared to the AROMA/IJRAY generator.

### 6.1.2 HERWIG

HERWIG [77, 78] is a general-purpose event generator for high energy hadronic processes, with particular emphasis on the detailed simulation of QCD parton showers. HERWIG is particularly suited for high momentum transfer, giving rise to emission of jets of hadrons. The theoretical basis is the resummation of the perturbative QCD expansion including all asymptotic and some important subasymptotic contributions. From the point of view of heavy quark physics the generator has the following features:

- simulation of hard lepton-lepton, hadron-lepton and hadron-hadron scattering,
- colour coherence of partons (initial and final) in hard subprocesses,
- heavy flavour hadron production and decay with QCD coherence effects,
- cluster hadronization of jets via non-perturbative gluon splitting.

The generator simulates a variety of primary collision processes, followed by parton shower generation using a coherent branching algorithm and hadronic formation using a cluster fragmentation model. The resolved part of the generator treats the contribution of the  $c$ -quark and the contribution of the light quark ( $u, d, s$ ) and the gluons ( $g$ ) coming out of the hadronic state of the photon separately and gives us the opportunity to study their relative contributions.

The comparison is shown in Figure 6.3. A reasonable description of the shapes of single differential cross sections can be claimed. HERWIG is a leading order generator too, therefore the cross sections are underestimated as in the case of AROMA-IJRAY. There are two remarkable effects: the spectra are harder in  $p_{\perp}$  than in the AROMA-IJRAY generator and the resolved part is clearly dominated by the contributions of the  $c$ -quarks. Generally the resolved contribution to the cross section is bigger than in the AROMA/IJRAY generator and has a different shape in  $\hat{y}$ .

Figures 6.4 and 6.5 present the double differential cross sections as a function of  $p_{\perp}$  and  $\hat{y}$ , again the direct and resolved parts separately. The resolved part is further split in the contributions from  $c$ -quarks and the light quarks or gluons in the photon. In contrast to the AROMA-IJRAY generator, the contribution from the resolved part increases with increasing  $p_{\perp}$ , and dominates the distributions in the high  $p_{\perp}$  range. Again the dominance of the  $c$ -quark contribution to the resolved part can be clearly seen.

Generally, the studies of the leading order Monte Carlo generators point out the importance of next to leading order calculations to predict the cross sections.

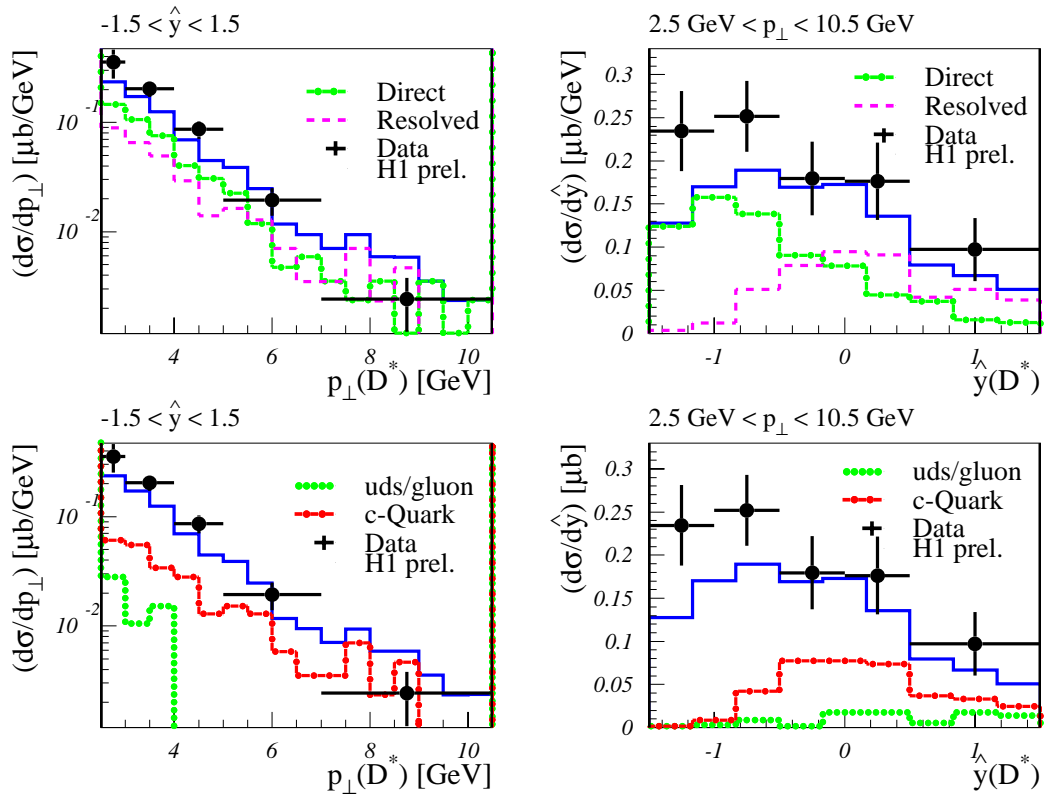


Figure 6.3: Single differential cross section  $d\sigma/dp_{\perp}, d\hat{y}$  as function of  $p_{\perp}$  and  $\hat{y}$  in comparison with the predictions of the HERWIG generator. The direct and resolved part are shown separately, the resolved part is splitted in the contribution of the c-quark and the light quarks/gluon from the photon

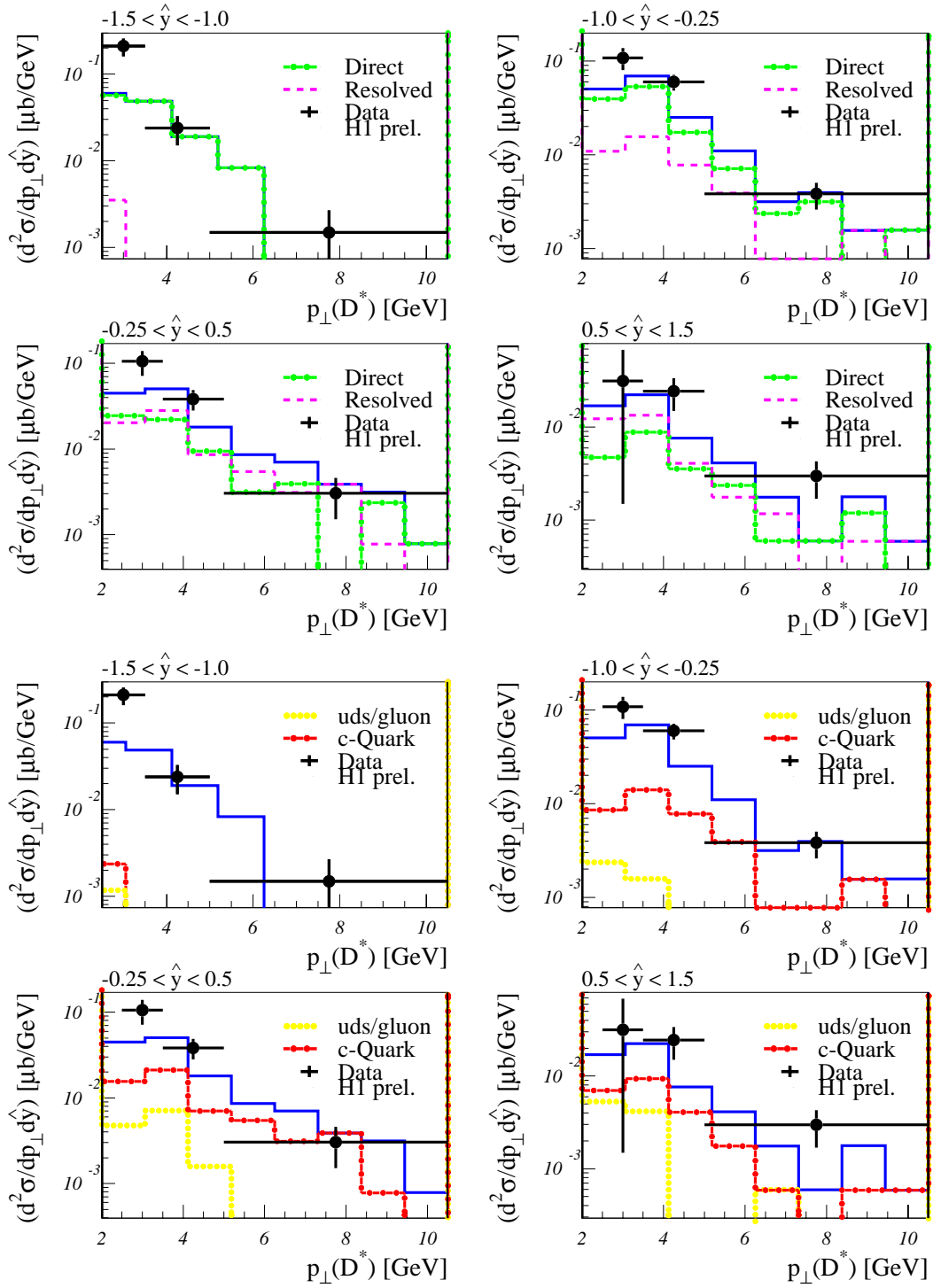


Figure 6.4: Double differential cross section  $d^2\sigma/dp_{\perp}d\hat{y}$  as function of  $p_{\perp}$  in regions of  $\hat{y}$ , compared to the HERWIG generator. The direct and resolved part are shown separately. The resolved part is splitted in the contribution of the  $c$ -quark and the light quarks/gluon from the photon.

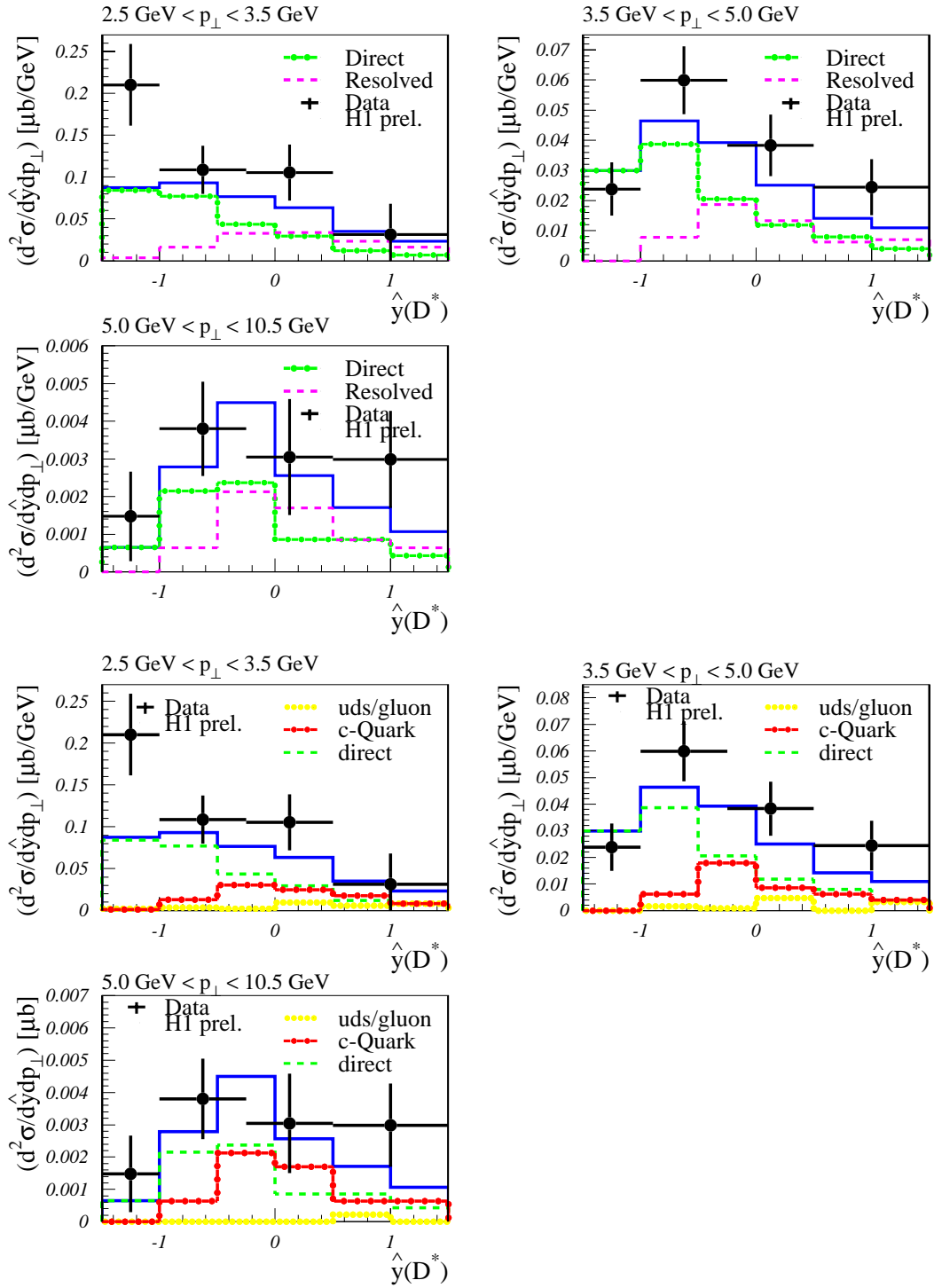


Figure 6.5: Double differential cross section  $d^2\sigma/dp_\perp d\hat{y}$  as function of  $\hat{y}$  in regions of  $p_\perp$ , compared to the HERWIG generator. The direct and resolved part are shown separately. The resolved part is split in the contribution of the c-quark and the light quarks/gluon from the photon.

## 6.2 Comparison to the massive calculations

In Figures 6.6 - 6.13 various comparisons of the measured single inclusive and double differential cross sections to the theoretical NLO models are made, which have been introduced in chapter 2.

For the calculations in the massive scheme the following standard settings were used:

- mass of the charm quark  $m_c = 1.5 \text{ GeV}/c^2$ , varied by  $\pm 0.2 \text{ GeV}/c^2$ ,
- factorization scale parameter  $\mu_F = \mu_\gamma = 2\mu_R = \sqrt{m_c^2 + p_\perp^2}$ ,
- fragmentation function parameter  $\epsilon_{\text{Peterson}} = 0.035$  for comparison  $\epsilon = 0.06$ ,
- Invariant mass of  $\gamma p$  system  $\overline{W}_{\gamma p} = 196 \text{ GeV}$ ,
- $\alpha_s = 0.119$ ,  $\Lambda_{QCD} = 237 \text{ GeV}$
- Parton density for the proton: MRSA' [79], MRSG [80] and MRST [81],
- Parton density for the photon: GRV-HO [32] and LAC1 [31].

All calculations have been performed at a fixed  $\overline{W}_{\gamma p} = 196 \text{ GeV}$  corresponding to the measured mean value of the kinematical range of our analysis. The distributions of the single and double differential cross section in function of  $p_\perp$  and  $\hat{y}$  are shown.

The MRST-GRV parametrization leads to good agreement within the errors with the single differential cross section (Figure 6.6). The variation of the charm quark mass and the fragmentation parameter  $\epsilon$  can best be seen in the rapidity distributions. Different choices of the parton density functions are presented in Figure 6.7. The MRSA' parameterization seems to underestimate the cross section in the forward region ( $\hat{y} > 0$ ) somewhat, while the MRSG parametrization overestimates the cross section in the backward region ( $\hat{y} < 0$ ). For the resolved part, both the GRV and LAC1 parameterizations describe the data within the statistical errors quite well.

In the comparison to the double differential cross section (Figures 6.8 - 6.11) similar observations can be made. The shape of the rapidity distribution is more sensitive to the production mechanism than the shape of the  $p_\perp$  distribution, in particular for the higher  $p_\perp$  region. The choice of  $\epsilon$  and  $m_c$  is less important than the choice of the partonic density function (Figures 6.12 and 6.13).

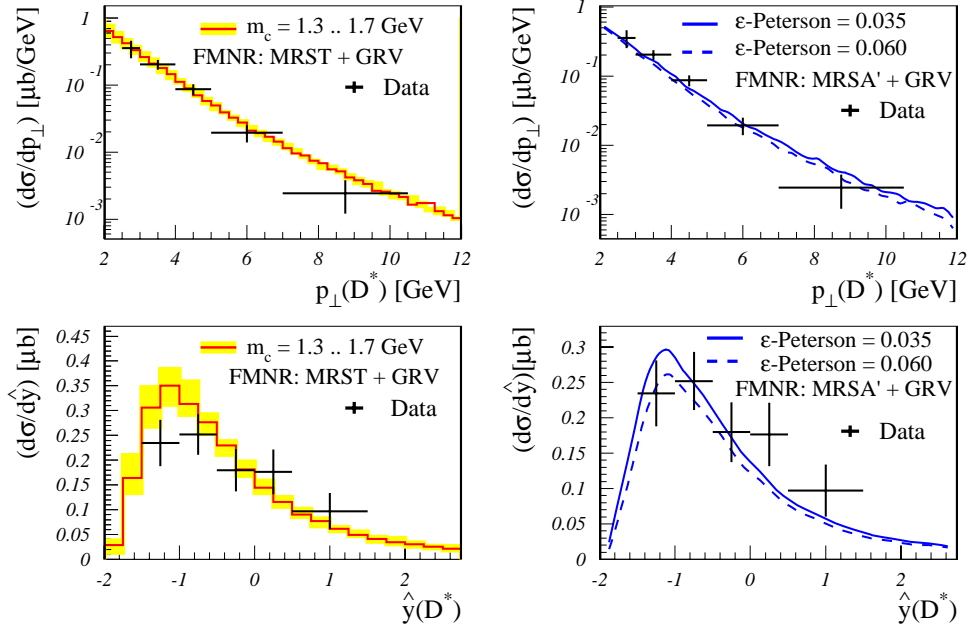


Figure 6.6: Single differential cross section  $d\sigma/dp_{\perp}, d/drap$  as function of  $p_{\perp}$  and  $\hat{y}$  in comparison with the massive theory. Variations of the charm quark mass (a) and  $\epsilon$ -Peterson (b) are shown.

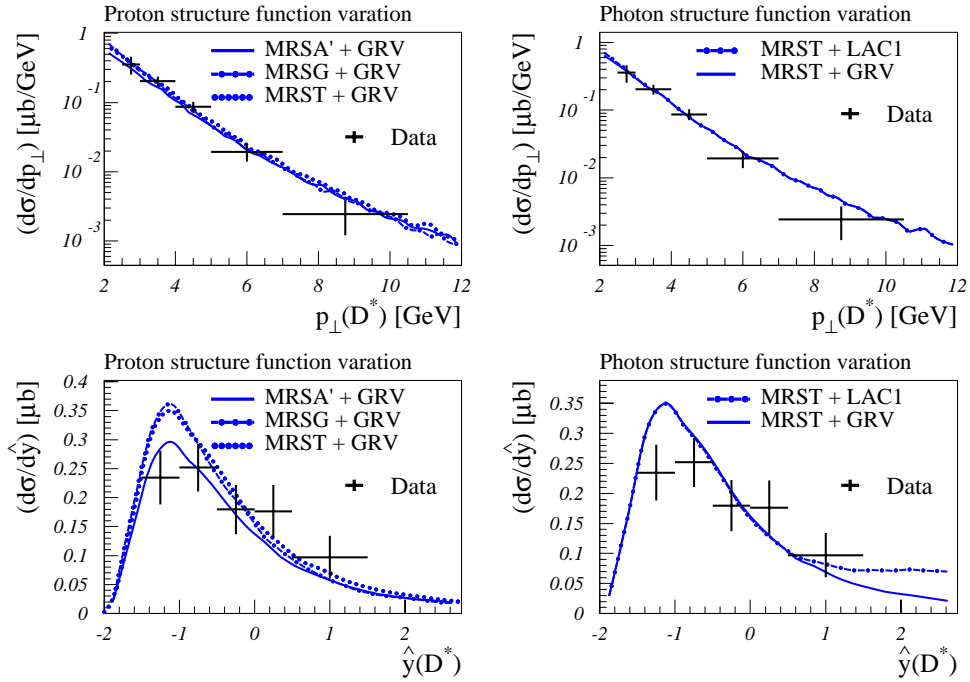


Figure 6.7: Single differential cross section  $d\sigma/dp_{\perp}, d\hat{y}$  as function of  $p_{\perp}$  and  $\hat{y}$  in comparison to the massive theory. Variations of the proton structure function (MRSG/MRSA') (a) and the photon structure function (LAC1/GRV) (b) are shown.

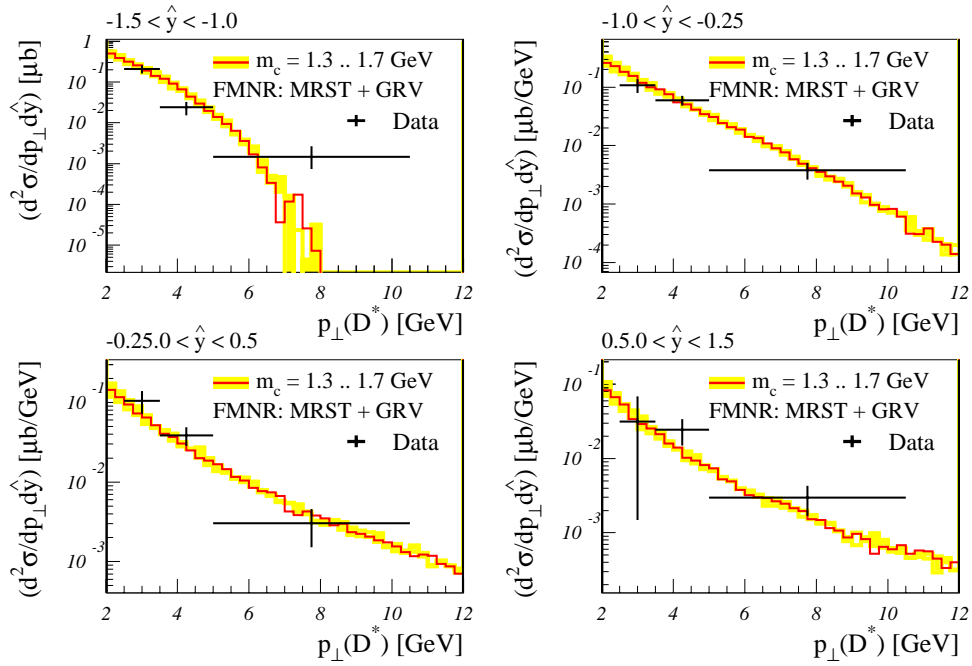


Figure 6.8: *Double differential cross sections  $d^2\sigma/dp_\perp d\hat{y}$  as function of  $p_\perp$  in regions of  $\hat{y}$ , comparison to massive theory. The variations of the charm quark mass is shown.*

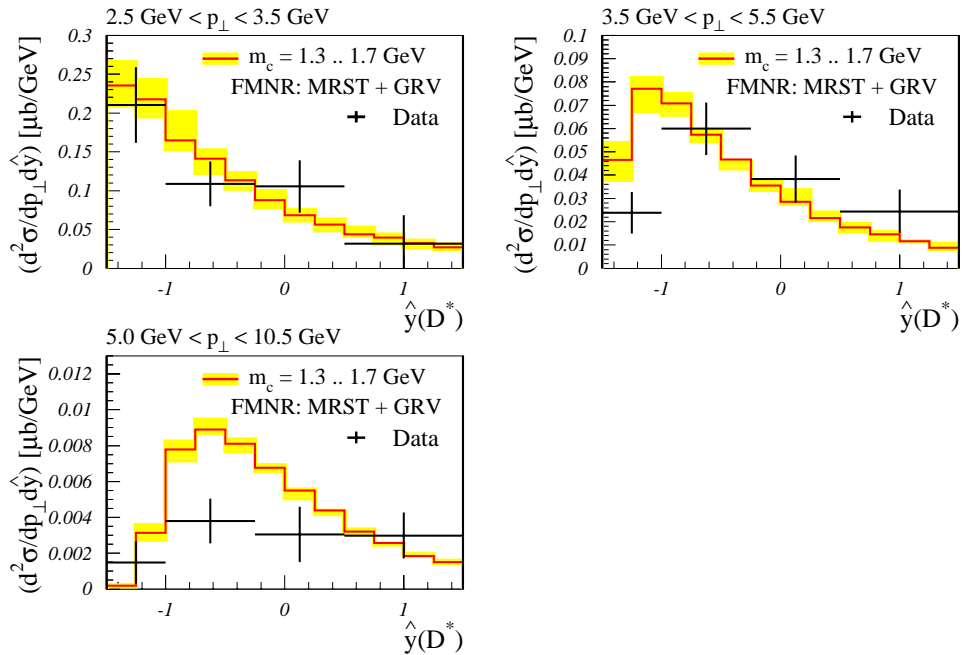


Figure 6.9: *Double differential cross sections  $d^2\sigma/dp_\perp d\hat{y}$  as function of  $\hat{y}$  in regions of  $p_\perp$ , comparison to massive theory. The variations of the charm quark mass is shown.*

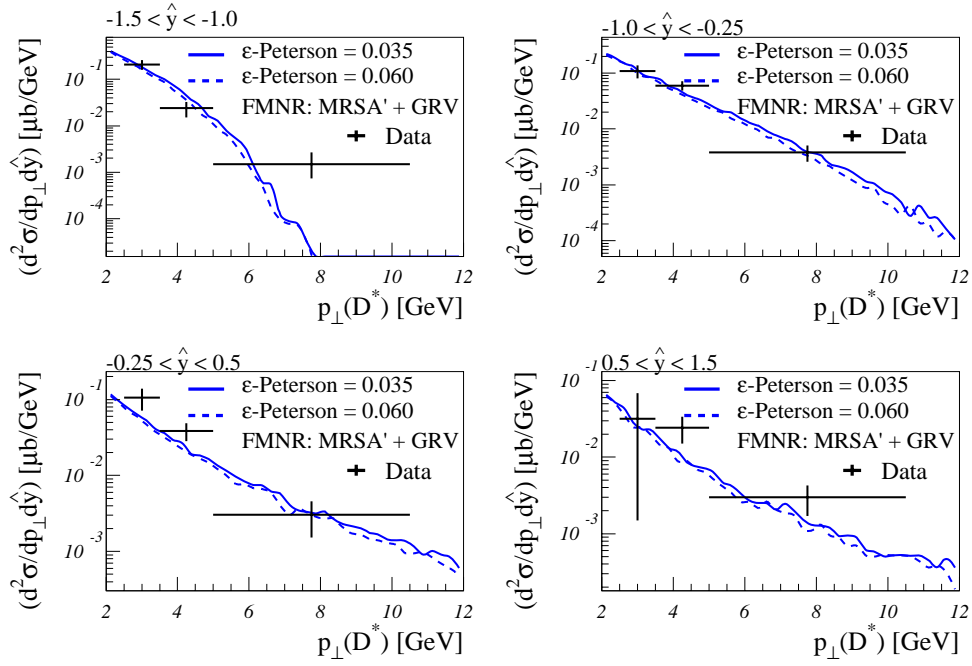


Figure 6.10: Double differential cross sections  $d^2\sigma/dp_{\perp}d\hat{y}$  as function of  $p_{\perp}$  in regions of  $\hat{y}$ , comparison to massive theory. The variations of  $\epsilon$ -Peterson is shown.

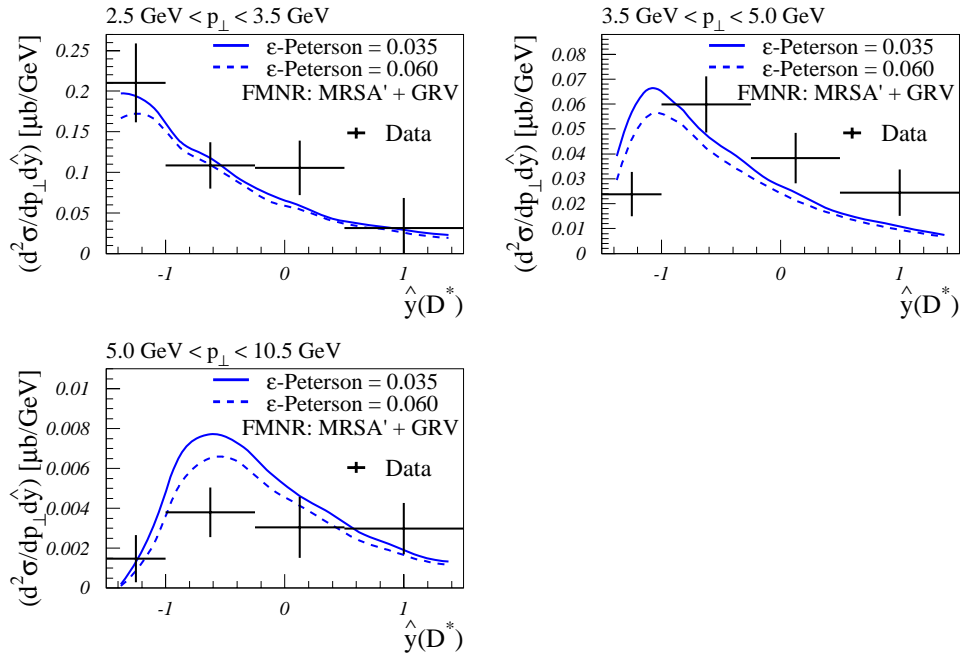


Figure 6.11: Double differential cross sections  $d^2\sigma/dp_{\perp}d\hat{y}$  as function of  $\hat{y}$  in regions of  $p_{\perp}$ , comparison to massive theory. The variations of  $\epsilon$ -Peterson is shown.

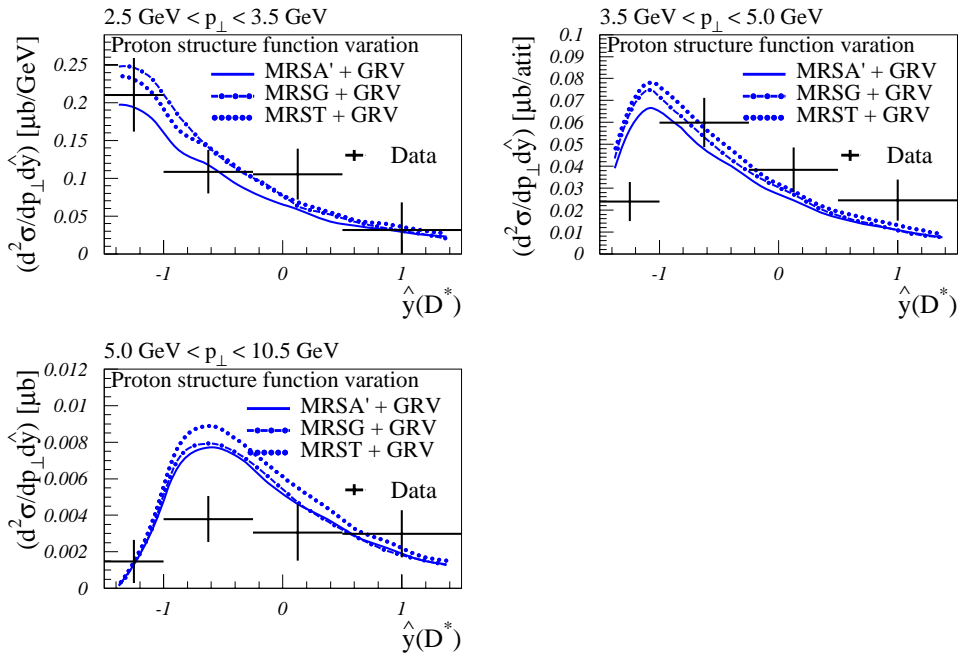


Figure 6.12: Double differential cross sections  $d^2\sigma/dp_\perp d\hat{y}$  as function of  $\hat{y}$  in regions of  $p_\perp$ , comparison to massive theory. The variations of the proton structure function (MRSG, MRSA' and MRST) is shown.

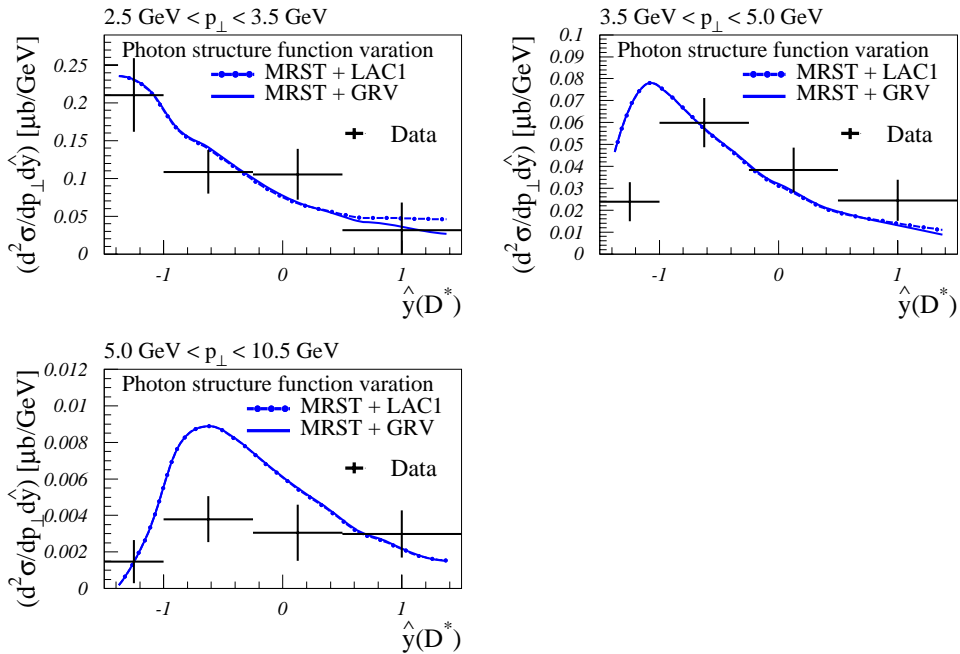


Figure 6.13: Double differential cross sections  $d^2\sigma/dp_\perp d\hat{y}$  as function of  $\hat{y}$  in regions of  $p_\perp$ , comparison to massive theory. The variations of the photon structure function (GRV and LAC1) is shown.

### 6.3 Comparison to the massless calculations

All cross sections were also compared to the massless calculations presented in [33] and [34]. The following setting for the calculation has been used by the authors:

- $m_c = 1.5 \text{ GeV}/c^2$ ,
- renormalization scheme:  $\overline{MS}$ , with  $n_f = 4$  active flavors in the initial state and  $\Lambda_{QCD} = 296 \text{ MeV}$ ,
- proton parton density function: CTEQ4M [30],
- photon parton density function: GRV HO [32] and GS96 HO [83],
- fragmentation function: BKK NLO-O [82], starting at  $\mu_0 = 2m_c$ .

The kinematical range is the same as above  $\overline{W}_{\gamma p} = 196 \text{ GeV}$ ,  $Q^2$  is also restricted to the photoproduction region ( $< 0.01 \text{ GeV}^2$ ), and the inelasticity  $y$  is restricted to the same range as in the analysis ( $0.26 < y < 0.62$ ). Again distributions in  $p_\perp$  and  $\hat{y}$  are shown, and finally the double differential spectra.

Figure 6.14 presents the single differential spectra, using two different parton density functions (PDF) for the photon (GRV and GS96). While the backward  $\hat{y}$  region ( $\hat{y} < 0$ ) is overestimated by the theory for both PDF's, the forward region is in good agreement. The direct and resolved fraction are shown separately. This points to a further difference between the massive and the massless approach: the resolved fraction is much higher than the direct one. The  $p_\perp$  spectra are in quite good agreement. Generally, the GS96 PDF describes the data in a better way than GRV, but the cross sections are still overestimated by a factor 2 (Figure 6.15).

Finally the double differential cross sections are compared to the massless calculations in Figures 6.16 and 6.18. For the  $\hat{y}$  distribution a good agreement for the medium  $p_\perp$  region is seen, but nevertheless the backward region ( $\hat{y} < 0$ ) is overestimated by a factor of 2. In the  $p_\perp$  spectra a good agreement is seen as well. Also for the double differential cross sections the massive and massless approach are compared in one figure (see Figure 6.20 and 6.21). As expected, the cross sections are always overestimated by the massless approach. In the region for highest transvers momenta, both approaches do not fit the data and are at the same order.

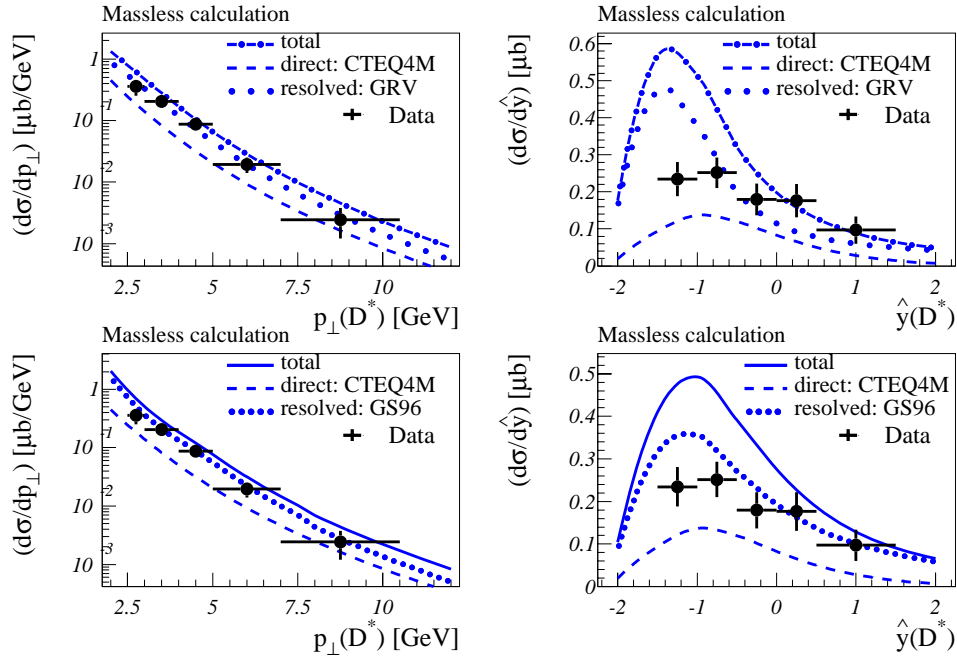


Figure 6.14: Single differential cross section  $d\sigma/dp_{\perp}, d\hat{y}$  as function of  $p_{\perp}$  and  $\hat{y}$  in comparison to the massless theory. The contributions of the direct and resolved part are shown separately.

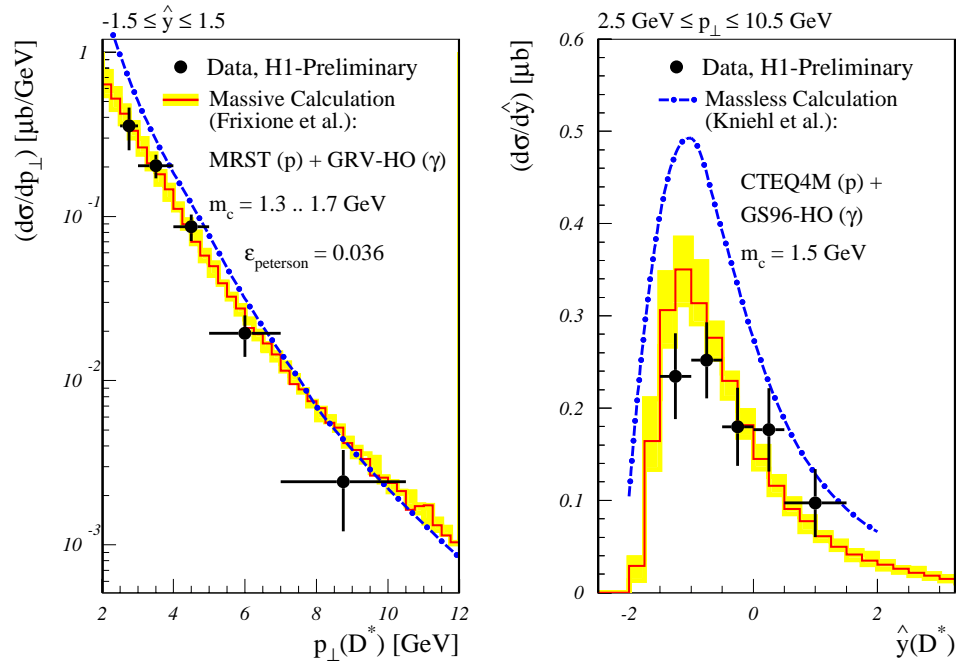


Figure 6.15: Single differential cross section  $d\sigma/dp_{\perp}, d\hat{y}$  as function of  $p_{\perp}$  and  $\hat{y}$  in comparison to the massless and the massive theory. The best fitting parametrization are shown for both approaches.

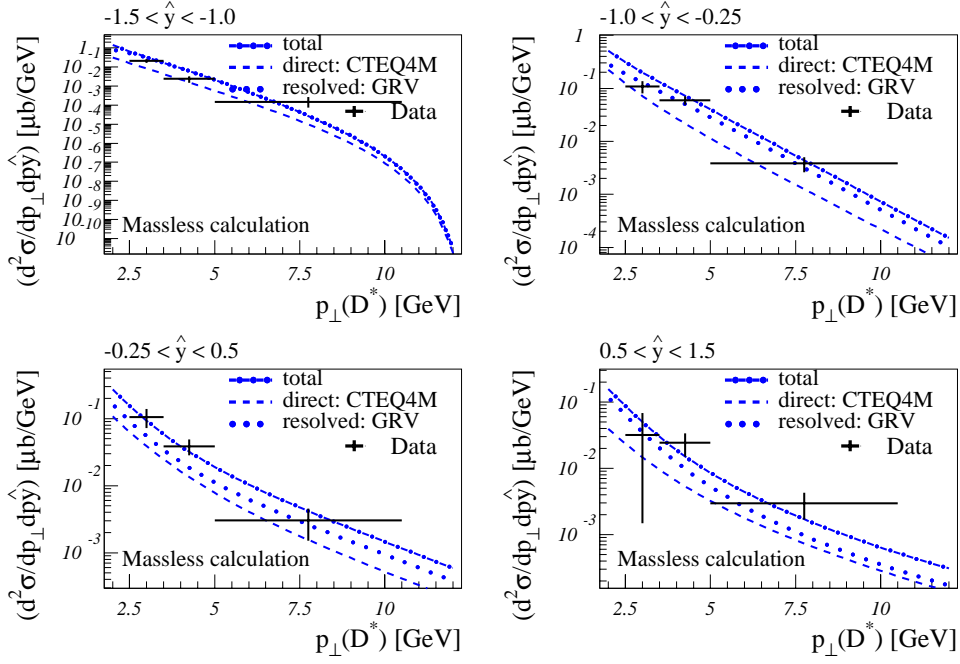


Figure 6.16: Double differential cross sections  $d^2\sigma/dp_\perp d\hat{y}$  as function of  $p_\perp$  in regions of  $\hat{y}$ , comparison to massless theory. The contributions of the direct and resolved (GRV) part are shown separately.

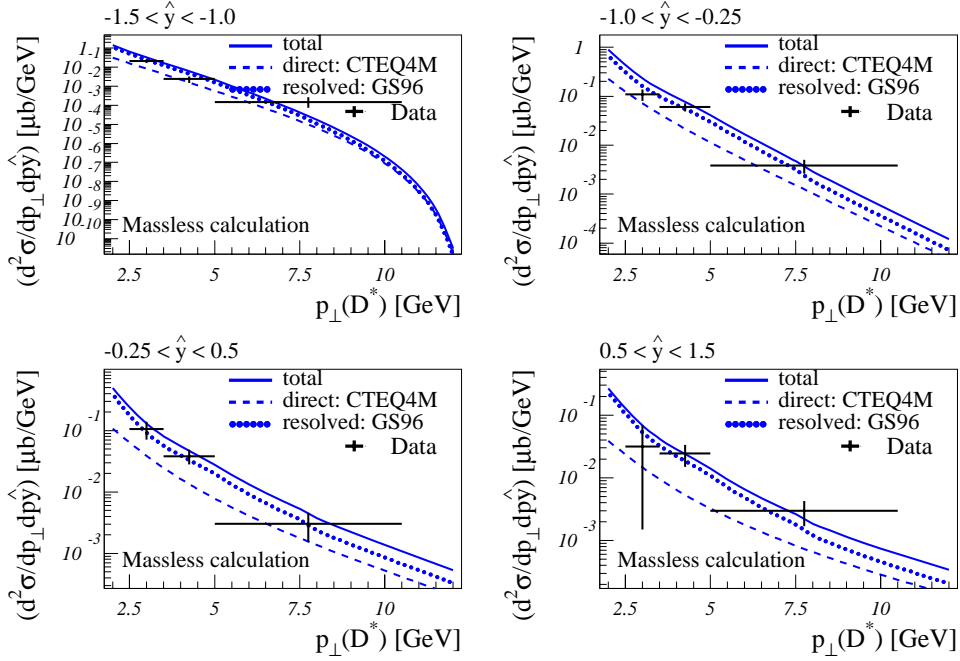


Figure 6.17: Double differential cross sections  $d^2\sigma/dp_\perp d\hat{y}$  as function of  $p_\perp$  in regions of  $\hat{y}$ , comparison to massless theory. The contributions of the direct and resolved (GS96) part are shown separately.

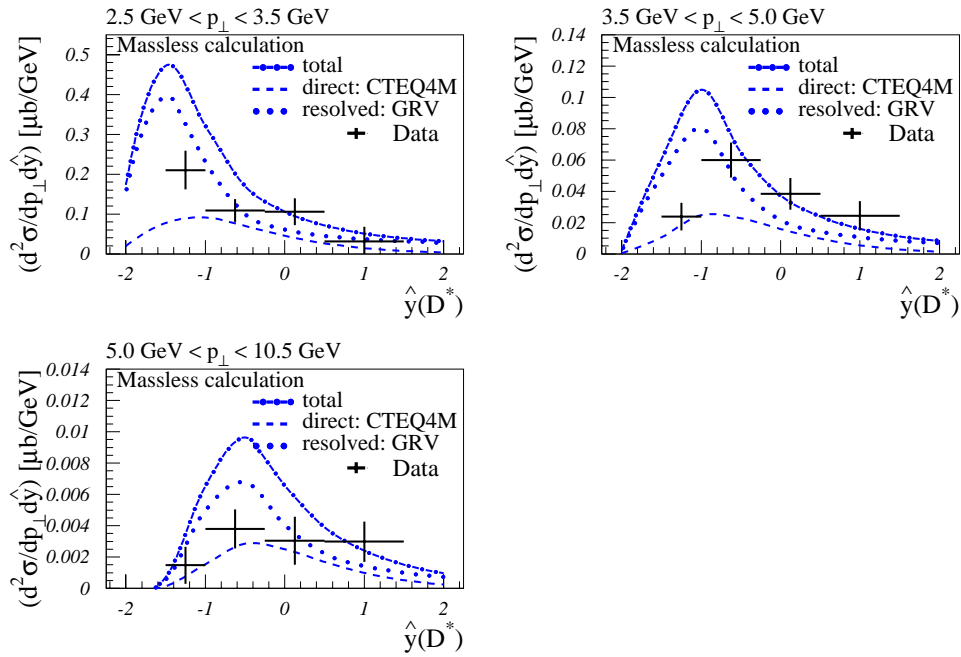


Figure 6.18: Double differential cross sections  $d^2\sigma/dp_\perp d\hat{y}$  as function of  $\hat{y}$  in regions of  $p_\perp$ , comparison to massless theory. The contributions of the direct and resolved (GRV) part are shown separately.

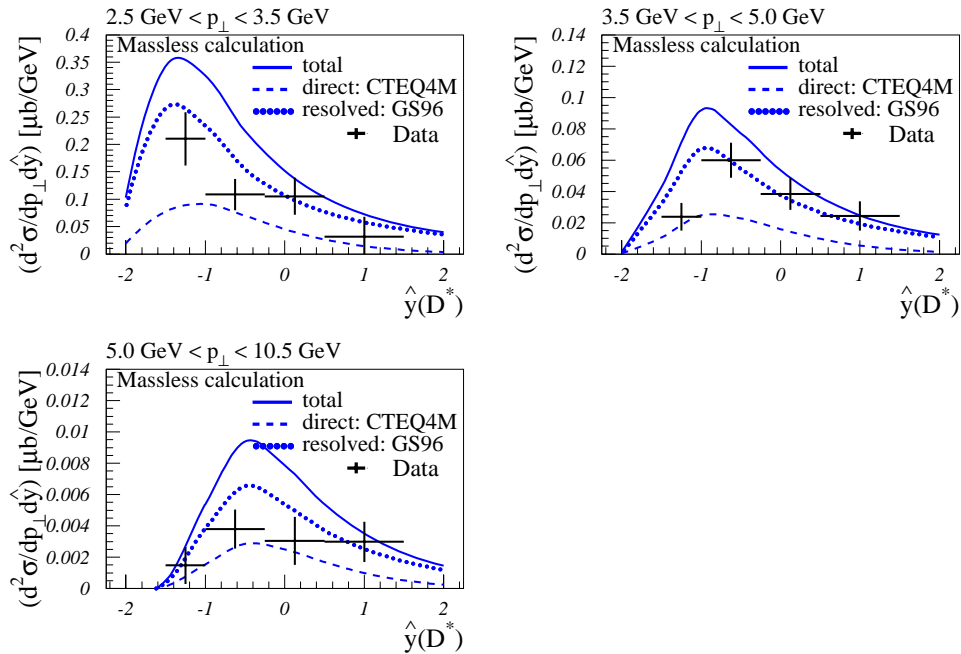


Figure 6.19: Double differential cross sections  $d^2\sigma/dp_\perp d\hat{y}$  as function of  $\hat{y}$  in regions of  $p_\perp$ , comparison to massless theory. The contributions of the direct and resolved (GS96) part are shown separately.

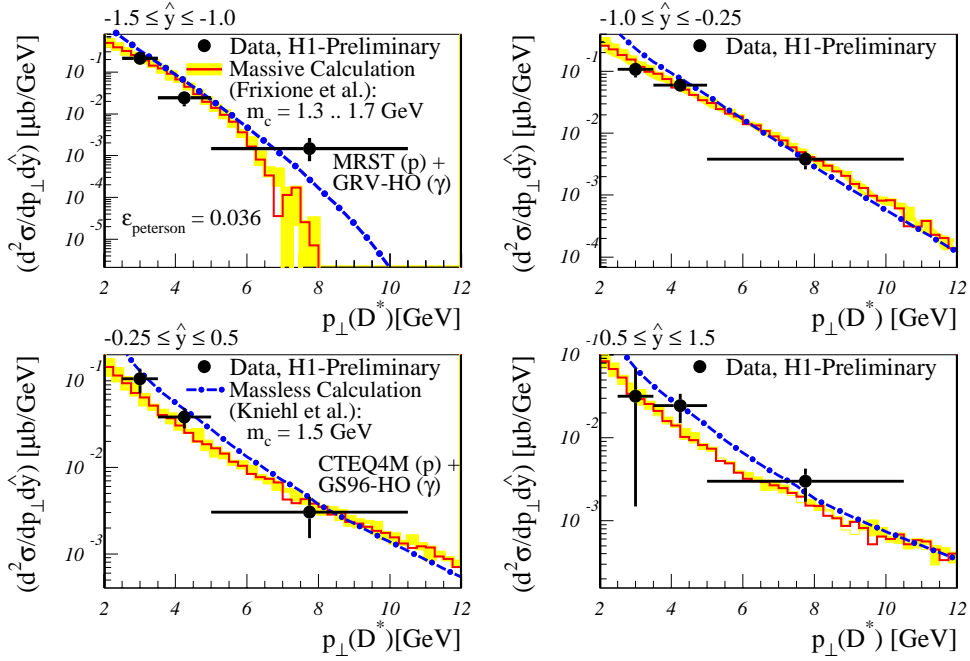


Figure 6.20: Double differential cross sections  $d^2\sigma/dp_{\perp}d\hat{y}$  as function of  $\hat{y}$  in regions of  $p_{\perp}$ , comparison to massive and massless theory

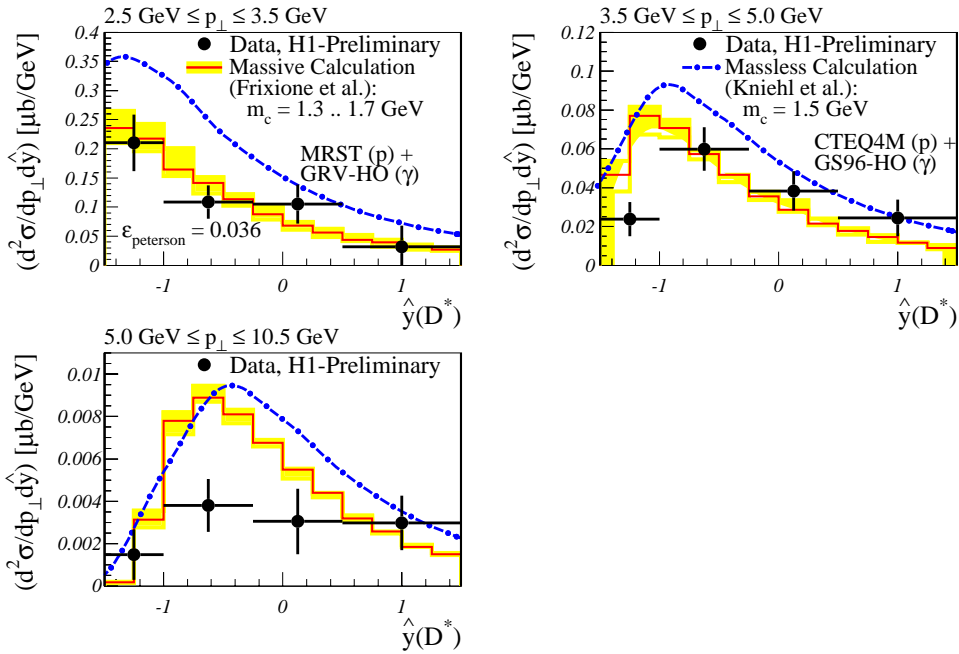


Figure 6.21: Double differential cross sections  $d^2\sigma/dp_{\perp}d\hat{y}$  as function of  $\hat{y}$  in regions of  $p_{\perp}$ , comparison to massive and massless theory.

# Chapter 7

## Conclusions

The goal of this analysis was to present single and double differential cross section measurements for charm quark photoproduction at high energies and confront these new data with the available QCD calculations, for which two different approaches are currently en vogue. In the “massive” scheme the charm quark is produced predominantly by boson-gluon fusion in the final state, in the “massless” scheme the charm quark is treated as a massless parton and active flavour of the initial state as well. This influences the results of the theoretical calculations for the proton and photon parton density functions, and therefore their relative contributions of the direct (boson gluon fusion) and the resolved process (the photon fluctuates into a hadronic state before the interaction) to the total cross section. The rapidity and transverse momentum distributions of the charm quarks were expected to be sufficiently different to distinguish between these two models.

Experimentally charm quarks can be recognized by the decays of  $D^*$  mesons into  $D^* \rightarrow K \pi \pi_s$ , where the decay particles are measured in the central detector. The kinematical region is defined by the scattered electron. In quasireal photoproduction ( $Q^2 \approx 0$ ) the electron is scattered under small angles and measured outside the main detector in the electron tagger. The event sample from the available luminosity of  $12 \text{ pb}^{-1}$  was sufficiently large to allow a measurement of single and double differential cross sections in regions of  $p_{\perp}$  and  $\hat{y}$ .

It was observed that the shape of the  $\hat{y}$  distributions is more sensitive to variations of the theoretical parameters than the shape of the  $p_{\perp}$  distributions. Generally a good agreement with the massive calculation was found. The massless calculation describes the data reasonably well only in the forward region ( $\hat{y} > 0$ ). In the high  $p_{\perp}$  region both theoretical predictions fail to describe the data well. However here also the statistics is fairly low to draw strong conclusions.

In 1997 H1 has accumulated ca.  $25 \text{ pb}^{-1}$  of luminosity. The larger event sample expected from this run should certainly permit to sharpen our conclusions. The present analysis should also be extended to untagged photoproduction ( $0.01 \text{ GeV}^2 < Q^2 < 2 \text{ GeV}^2$ ) to close the gap to the DIS data.

# Appendix A

## Tables of efficiencies and cross sections

The acceptance and efficiency corrections are explained in chapter 5.3. The results are given in the following table.

|                                    |                 |                 |                 |                 |                 |
|------------------------------------|-----------------|-----------------|-----------------|-----------------|-----------------|
| $p_{\perp}$ [GeV]                  | 2.5 - 3.0       | 3.0 - 4.0       | 4.0 - 5.0       | 5.0 - 7.0       | 7.0 - 10.5      |
| $\epsilon_{rec}^{dir}(p_{\perp})$  | $77.4 \pm 1.1$  | $81.2 \pm 0.9$  | $80.0 \pm 1.5$  | $84.1 \pm 1.6$  | $82.0 \pm 2.9$  |
| $\epsilon_{rec}^{res}(p_{\perp})$  | $78.6 \pm 5.5$  | $82.9 \pm 4.5$  | $66.7 \pm 11.1$ | $85.7 \pm 13.3$ | $75.0 \pm 21.7$ |
| $\epsilon_{rec}^{tot}(p_{\perp})$  | $76.5 \pm 2.7$  | $79.0 \pm 2.2$  | $76.3 \pm 3.6$  | $76.4 \pm 5.0$  | $81.0 \pm 7.1$  |
| $\epsilon_{trig}^{dir}(p_{\perp})$ | $89.3 \pm 1.2$  | $90.3 \pm 1.0$  | $93.4 \pm 1.5$  | $86.5 \pm 1.6$  | $86.3 \pm 2.8$  |
| $\epsilon_{trig}^{res}(p_{\perp})$ | $75.6 \pm 6.1$  | $80.6 \pm 4.9$  | $69.4 \pm 12.7$ | $69.7 \pm 17.9$ | $64.0 \pm 18.4$ |
| $\epsilon_{trig}^{tot}(p_{\perp})$ | $87.4 \pm 2.2$  | $88.4 \pm 1.9$  | $88.1 \pm 3.0$  | $82.5 \pm 4.7$  | $83.1 \pm 6.6$  |
| $\hat{y}$                          | -1.5 - -1.0     | -1.0 - -0.5     | -0.5 - 0.0      | 0.0 - 0.5       | 0.5 - 1.5       |
| $\epsilon_{rec}^{dir}(\hat{y})$    | $74.7 \pm 1.1$  | $81.0 \pm 0.8$  | $82.2 \pm 1.0$  | $83.3 \pm 1.3$  | $80.4 \pm 1.7$  |
| $\epsilon_{rec}^{res}(\hat{y})$    | $85.7 \pm 12.3$ | $66.7 \pm 10.2$ | $83.3 \pm 7.5$  | $82.4 \pm 6.4$  | $78.3 \pm 4.7$  |
| $\epsilon_{rec}^{tot}(\hat{y})$    | $68.3 \pm 3.4$  | $80.5 \pm 2.4$  | $81.6 \pm 2.7$  | $79.4 \pm 4.4$  | $76.9 \pm 4.6$  |
| $\epsilon_{trig}^{dir}(\hat{y})$   | $84.6 \pm 1.2$  | $94.4 \pm 0.9$  | $89.3 \pm 1.0$  | $83.3 \pm 1.4$  | $86.1 \pm 1.6$  |
| $\epsilon_{trig}^{res}(\hat{y})$   | $68.6 \pm 18.2$ | $68.7 \pm 11.4$ | $77.5 \pm 8.6$  | $75.9 \pm 7.9$  | $78.0 \pm 5.1$  |
| $\epsilon_{trig}^{tot}(\hat{y})$   | $83.8 \pm 3.2$  | $89.5 \pm 2.1$  | $88.8 \pm 2.2$  | $84.8 \pm 4.1$  | $85.3 \pm 3.8$  |

Table A.1: *Reconstruction efficiencies 1996 calculated with simulated MC data samples separately for direct and resolved events.*

| $p_{\perp}$ [GeV]                  | 2.5 - 3.0       | 3.0 - 4.0       | 4.0 - 5.0      | 5.0 - 7.0       | 7.0 - 10.5      |
|------------------------------------|-----------------|-----------------|----------------|-----------------|-----------------|
| $\epsilon_{rec}^{dir}(p_{\perp})$  | $72.6 \pm 3.7$  | $85.1 \pm 2.6$  | $79.7 \pm 4.5$ | $82.5 \pm 6.0$  | $86.7 \pm 8.5$  |
| $\epsilon_{rec}^{res}(p_{\perp})$  | $83.1 \pm 4.9$  | $79.7 \pm 5.0$  | $83.3 \pm 8.8$ | $42.9 \pm 18.7$ | $75.0 \pm 21.7$ |
| $\epsilon_{rec}^{tot}(p_{\perp})$  | $74.9 \pm 3.1$  | $84.0 \pm 2.3$  | $80.3 \pm 4.1$ | $78.2 \pm 5.7$  | $84.6 \pm 7.9$  |
| $\epsilon_{trig}^{dir}(p_{\perp})$ | $95.4 \pm 2.0$  | $96.2 \pm 1.5$  | $95.4 \pm 2.5$ | $94.4 \pm 3.8$  | $79.6 \pm 10.1$ |
| $\epsilon_{trig}^{res}(p_{\perp})$ | $82.3 \pm 5.3$  | $87.0 \pm 4.5$  | $83.1 \pm 8.7$ | $64.0 \pm 18.4$ | $60.1 \pm 18.5$ |
| $\epsilon_{trig}^{tot}(p_{\perp})$ | $92.0 \pm 2.0$  | $94.3 \pm 1.5$  | $93.5 \pm 2.5$ | $92.5 \pm 3.8$  | $77.1 \pm 9.0$  |
| $\hat{y}$                          | -1.5 - -1.0     | -1.0 - -0.5     | -0.5 - 0.0     | 0.0 - 0.5       | 0.5 - 1.5       |
| $\epsilon_{rec}^{dir}(\hat{y})$    | $68.2 \pm 4.4$  | $83.1 \pm 3.1$  | $85.6 \pm 3.1$ | $87.5 \pm 5.2$  | $72.7 \pm 7.8$  |
| $\epsilon_{rec}^{res}(\hat{y})$    | $83.3 \pm 14.1$ | $85.0 \pm 7.8$  | $87.5 \pm 6.6$ | $85.3 \pm 6.0$  | $70.3 \pm 5.3$  |
| $\epsilon_{rec}^{tot}(\hat{y})$    | $68.6 \pm 4.3$  | $83.2 \pm 2.9$  | $85.9 \pm 2.8$ | $86.7 \pm 3.9$  | $71.1 \pm 4.3$  |
| $\epsilon_{trig}^{dir}(\hat{y})$   | $94.9 \pm 2.5$  | $96.8 \pm 1.6$  | $93.9 \pm 2.2$ | $94.5 \pm 3.7$  | $92.5 \pm 5.0$  |
| $\epsilon_{trig}^{res}(\hat{y})$   | $69.4 \pm 16.6$ | $76.7 \pm 10.2$ | $76.4 \pm 9.2$ | $90.2 \pm 5.3$  | $87.2 \pm 4.5$  |
| $\epsilon_{trig}^{tot}(\hat{y})$   | $93.9 \pm 2.5$  | $94.9 \pm 1.7$  | $91.8 \pm 2.3$ | $92.9 \pm 3.1$  | $89.2 \pm 3.4$  |

Table A.2: Reconstruction efficiencies 1995 calculated with simulated MC data samples separately for direct and resolved events.

| $d^2\sigma_{\gamma p}/dp_{\perp}d\hat{y}[nb]$ | $2.5 < p_{\perp} < 3.5$<br>[GeV] | $3.5 < p_{\perp} < 5.0$<br>[GeV] | $5.0 < p_{\perp} < 10.5$<br>[GeV] |
|-----------------------------------------------|----------------------------------|----------------------------------|-----------------------------------|
| $-1.5 < \hat{y} < -1.0$                       | $210.5 \pm 48.7$                 | $23.9 \pm 8.9$                   | $1.5 \pm 1.1$                     |
| $-1.0 < \hat{y} < -0.25$                      | $108.6 \pm 28.7$                 | $60.0 \pm 11.3$                  | $3.8 \pm 1.2$                     |
| $-0.25 < \hat{y} < 0.5$                       | $105.3 \pm 33.6$                 | $38.4 \pm 10.2$                  | $3.1 \pm 1.5$                     |
| $0.5 < \hat{y} < 1.5$                         | $36.7 \pm 31.7$                  | $24.4 \pm 9.3$                   | $3.0 \pm 1.2$                     |

Table A.3: Values of the double differential cross sections

# Bibliography

- [1] G. Wolf, *HERA Physics*, DESY 94-022, Proc. of 42<sup>nd</sup> Scottish Universities Summer School in Physics (SUSSP 93): High Energy Phenomenology (NATO Advanced Study Institute), St. Andrews, UK (1993), p. 135.
- [2] A. Levy, *Low- $x$  Physics at HERA*, DESY 97-013, Proc. Strong Interaction Study Days, Kloster Banz, Germany (1995), in Lectures on QCD, ed. F. Lenz, p. 347.
- [3] T. Janssens, R. Hofstadter et al., Phys. Rev. 142 (1966) 922.
- [4] R.R. Taylor, Proc. 4<sup>th</sup> Int. Symp. on Electron and Photon Interactions at High Energies, Liverpool, 1969, Daresbury Nucl. Phys. Lab. (1969), p. 521
- [5] J. D. Bjorken, Phys. Rev. 179 (1969) 1547.
- [6] F. Jacquet, A. Blondel, Proceedings of the workshop: Study for an  $ep$  Facility in Europe, DESY 79-48 (1979) 391.
- [7] D. J. Fox et al., Phys. Rev. Lett. 41 (1974) 1504.
- [8] C. Chang et al., Phys. Rev. Lett. 35 (1973) 901.
- [9] S. Weinberg, Phys. Rev. Lett. 31 (1973) 491.
- [10] H. Fritzsch, H. Gell-Mann and H. Leutwyler, Phys. Lett. 47 (1973) 365.
- [11] R. D. Peccei, Proceedings of the HERA Workshop, DESY 1987.
- [12] W. Buchmüller and G. Ingelmann, Physics at HERA, Proceedings of the Workshop DESY 1991.
- [13] G. Ingelmann, A. de Roeck and R. Klanner, Future Physics at HERA, Proceedings of the Workshop, DESY 1996
- [14] J.C. Collins, D. E. Scoper, G. Sterman, Nucl.Phys. B263 (1986) 37.
- [15] C. F. Weizsäcker, Z. Phys. 88 (1934) 612.
- [16] E. J. Williams, Phys. Rev. 45 (1934) 729.

- 
- [17] S. Frixione, M. L. Mangano, P. Nason and G. Ridolfi, Phys. Lett. B319 (1993) 339.
- [18] A. I. Lebedev, *Corrections to the Weitzäcker Williams Approximation for low  $Q^2$  ep-scattering*, Physics at HERA, Proceedings of the Workshop, Vol. 1, p. 613, DESY 1991.
- [19] S. Frixione, M. Mangano, P. Nason and G. Ridolfi, hep-ph/9702287, to appear in “Heavy Flavours II”, eds. A.J. Buras and M. Lindner, Advanced Series on Directions in High Energy Physics, World Scientific Publishing Co., Singapore (1998).
- [20] S. Frixione, P. Nason and G. Ridolfi, Nucl. Phys. B454 (1995) 3.
- [21] C. Peterson, D. Schlatter, I. Schmitt and P. M. Zerwas, Phys. Rev. D27 (1983) 105.
- [22] J. Chrin, Z. Phys. C36 (1987) 163.
- [23] P. Nason and C. Oleari, preprint CERN-TH/98-339, DTP/98/76, hep-ph/9811206.
- [24] R. K. Ellis and P. Nason, Nucl. Phys. B312 (1989) 551.
- [25] P. Nason, S. Dawson and R.K. Ellis, Nucl. Phys. B303 (1988) 607; B327 (1988) 47.
- [26] A. D. Martin, R. G. Roberts and W. J. Stirling, Phys.Rev. D50 (1994) 6734.
- [27] A. D. Martin, R. G. Roberts and W. J. Stirling, preprint RAL-95-021, DTP/95/14, hep-ph/9502336.
- [28] S. Frixione, M.L. Mangano, P. Nason and G. Ridolfi, Nucl. Phys. B431 (1994) 452.
- [29] A. D. Martin, R.G. Roberts and W.J. Steering, Phys. Lett. B306 (1993) 145, Phys. Lett. B309 (1993) 492.
- [30] H.L. Lai et al., preprint MSU-HEP-41024, CTEQ-404, hep-ph/9410404.
- [31] A. Levy, H. Abramowicz and K. Charchula, Phys. Lett. B269 (1991) 458.
- [32] M. Glück, E. Reya and A. Vogt, Phys.Rev. D45 (1992) 3986.
- [33] B. A. Kniehl, M. Krämer, G. Kramer and M. Spira, Phys. Lett. B356 (1995) 539.
- [34] B. A. Kniehl, G. Kramer and M. Spira, Z. Phys. C76 (1997) 689.

- 
- [35] M. Cacciari and M. Greco, Phys. Rev. D55 (1997) 7144.
- [36] P. Nason, S. Dawson and R.K. Ellis, Nucl. Phys. B327 (1989) 49.
- [37] C. Grab, ETH Zürich, *Heavy Flavour Production at HERA*, Proceedings of 7<sup>th</sup> Int. Symp. on Heavy Flavour Physics, Santa Barbara, 1997.
- [38] J. Binnewies, B. A. Kniehl and G. Kramer, Z. Phys. C76 (1997) 677.
- [39] H1-Coll., I. Abt et al., Nucl. Instr. Meth. A389 (1997) 310 (part I); *ibid.* 348 (part II).
- [40] ZEUS-Coll., The ZEUS Detector, Status Report, DESY, 1993.
- [41] HERA-B-Coll., HERA-B Design Report, DESY-PRC 95/01, January 1995.
- [42] HERMES-Coll., Technical Design Report, DESY, July 1993.
- [43] J. Bürger et al., Nucl. Instr. Meth. A279 (1989) 217.
- [44] S. Prell, *Z-Kalibration und dE/dx-Kalibration der zentralen Spurenkammer des H1-Detektors* PhD Thesis, University of Hamburg (1992), DESY FH1T-92-04.
- [45] P. Robmann et al., Nucl. Instr. Meth. A277 (1989) 368.
- [46] S. Egli et al., Nucl. Instr. Meth. A283 (1989) 487.
- [47] P. Robmann, *The central inner z-chamber of the H1 Experiment at HERA*, PhD Thesis, University of Zürich (1994), unpublished.
- [48] H. Bärwolff et al., Nucl. Instr. Meth. A283 (1989) 467.
- [49] K. Müller et al., Nucl. Instr. Meth. A457 (1992) 456.
- [50] H. Bethe und W. Heitler, Proc. Roy. Soc. A146 (1934) 83.
- [51] H1-Coll., Luminosity Measurement in the H1 Experiment at HERA, 28th International Conference on High Energy Physics ICHEP'96, Warsaw, Poland, pa17-026, July 1996.
- [52] H1-Coll., T. Ahmend et al., Z. Phys. C66 (1995) 529.
- [53] C. Dollfus, *Bose-Einstein Correlations in Deep Inelastic Scattering at HERA*, PhD Thesis, University of Zürich (1996), unpublished.
- [54] K. Esslinger and P. Robmann, Nucl. Inst. Meth. A334 (1993) 649.
- [55] G. Ingelman, J. Rathsman and G. A. Schuler, DESY preprint 1995, ISSN 0418-9833.

- 
- [56] G. Ingelman, J. Rathsman and G. A. Schuler, *Comput. Phys. Commun.* 101 (1997) 135.
- [57] T. Sjöstrand, CERN (1994), CERN-TH.7112/93.
- [58] I. Abt, H1 internal note H1-05/93-290, DESY (1993).
- [59] I. Abt, H1 internal note H1-05/93-289, DESY (1993).
- [60] B. Anderson, G. Gustafson, G. Ingelman and T. Sjörsand, *Phys. Rep.* 97 (1983) 31.
- [61] T. Sjöstrand, *Comp. Phys. Comm.* 82 (1994) 74.
- [62] A. D. Martin, R. G. Roberts and W. J. Stirling, RAL-94-055 (1994).
- [63] S. Frixione, M. L. Mangano, P. Nason and G. Ridolfi, *Phys. Lett B* 348 (1995) 633.
- [64] *Phys. Rev. D, Particles and Fields, Part1*, D54 (1996).
- [65] H1-Coll., S. Aid et al, *Z. Phys., C* 69 (1995) 27.
- [66] G. Zech, DESY Report 956-113.
- [67] W. Erdmann, *Untersuchung der Photoproduktion von  $D^*$ -Mesonen am ep-Speicherung HERA*, PhD Thesis, ETH Zürich Nr. 11441 (1996), unpublished.
- [68] R. Ackers et al. (OPAL Coll.), *The LEP Experiments*, CERN-PPE-96/017, *Nucl. Instr. Meth. Phys. Res., A* 378 (1996) 101.
- [69] R. Bernet, *Production of  $D^{*\pm}$  Mesons Measured with the H1 Detector at HERA*, PhD Thesis, ETH Zürich Nr. 11041 (1995), unpublished.
- [70] A. D. Martin, R. G. Roberts and W. J. Steerling, RAL-94-104 (1994).
- [71] M. Glück, E. Reya and A. Vogt, *Phys. Lett. B* 306 (1993) 391.
- [72] H1-Coll., S. Aid et al., *Nucl. Phys. B* 472 (1996) 32, hep-ex/9604005.
- [73] H. P. Beck, *Measurement of the Total Photoproduction Cross Section at the Electron Proton Collider HERA at  $W_{\gamma p}$  of 20 GeV*, PhD Thesis, University of Zürich (1996) unpublished
- [74] U. Langenegger, *A Measurement of the Beauty and Charm Production Cross Section at the ep Collider HERA*, PhD Thesis, ETH Zürich Nr. 12676 (1998), unpublished.
- [75] D. Müller, *A Measurement of the Gluon Density in the Proton based on Charm Production at HERA*, PhD Thesis, University of Zürich (1998), unpublished.

- 
- [76] M. Biddulph, *Scale Dependence of the Charm Production Cross Section in Photoproduction and Performance of the Central Silicon Tracker at the H1 Experiment*, PhD Thesis, ETH Zürich Nr. 12331 (1997), unpublished.
- [77] J. Chyla, H1 internal note H1-05/93-291, DESY (1993).
- [78] G. Marchesini, B. R. Webber, G. Abbiendi, I.G. Knowles, M. H. Seymour and L. Stanco, *Comp. Phys. Commun.* 67 (1992) 465.
- [79] A. D. Martin, R. G. Roberts and W. J. Steerling, *Phys. Rev. D* 51 (1995) 4756.
- [80] A. D. Martin, R. G. Roberts and W. J. Steerling, *Phys. Lett.* B354 (1995) 155.
- [81] A. D. Martin, R. G. Roberts, W. J. Steerling and R.S. Thorne, RAL-TR-98-029, hep-ph/9803445.
- [82] J. Binnewies, B. A. Kniehl and G. Kramer, *Phys. Rev. D* 58 (1998) 14014.
- [83] L. E. Gordon, J. K. Storrow, *Z. Phys.* C56 (1992) 307.

# List of Tables

|      |                                                                                                                                  |    |
|------|----------------------------------------------------------------------------------------------------------------------------------|----|
| 1.1  | Kinematic regions accessible at HERA . . . . .                                                                                   | 6  |
| 2.1  | Comparison of massive and massless scheme . . . . .                                                                              | 22 |
| 3.1  | CIZ drift velocity and time offset in 1995-1998 . . . . .                                                                        | 38 |
| 4.1  | Cut parameters of the L4 heavy quark finder . . . . .                                                                            | 51 |
| 4.2  | Cut parameters of $D^*$ selection . . . . .                                                                                      | 53 |
| 4.3  | Cut parameters on the invariant mass of $D^0$ . . . . .                                                                          | 53 |
| 4.4  | Luminosities 1994 - 1996 . . . . .                                                                                               | 55 |
| 5.1  | $\Delta M$ -fit results for cross section measurement . . . . .                                                                  | 67 |
| 5.2  | Peak with $\sigma$ of $p_{\perp}$ fits in data and MC . . . . .                                                                  | 67 |
| 5.3  | Peak with $\sigma$ of $\hat{y}$ fits in data and MC . . . . .                                                                    | 67 |
| 5.4  | Detector acceptance corrections . . . . .                                                                                        | 69 |
| 5.5  | Reconstruction efficiencies for 1996 . . . . .                                                                                   | 72 |
| 5.6  | Trigger efficiencies for 1996 . . . . .                                                                                          | 73 |
| 5.7  | Experimental systematic errors . . . . .                                                                                         | 74 |
| 5.8  | Acceptance for direct and resolved contributions for the extrapolation<br>to the visible range in NLO QCD calculations . . . . . | 76 |
| 5.9  | Results of the measurement of single differential cross sections<br>( $d\sigma_{\gamma p}/dp_{\perp}$ ) . . . . .                | 77 |
| 5.10 | Results of the measurement of single differential cross sections ( $d\sigma_{\gamma p}/d\hat{y}$ )                               | 77 |
| A.1  | Reconstruction and trigger efficiencies for 1996 . . . . .                                                                       | 98 |
| A.2  | Reconstruction and trigger efficiencies for 1995 . . . . .                                                                       | 99 |
| A.3  | Double Differential Cross sections . . . . .                                                                                     | 99 |

# List of Figures

|      |                                                                                                                                                   |    |
|------|---------------------------------------------------------------------------------------------------------------------------------------------------|----|
| 1.1  | Kinematic of a $ep$ event at HERA . . . . .                                                                                                       | 4  |
| 2.1  | Leading order charm photoproduction process . . . . .                                                                                             | 9  |
| 2.2  | Massive versus massless scheme . . . . .                                                                                                          | 10 |
| 2.3  | The factorization scale $\mu_F$ . . . . .                                                                                                         | 11 |
| 2.4  | The Peterson fragmentation function . . . . .                                                                                                     | 12 |
| 2.5  | Charm transverse momentum distributions in photon proton collisions                                                                               | 13 |
| 2.6  | Charm pseudorapidity distribution in photon proton collisions . . . .                                                                             | 13 |
| 2.7  | Sensitivity of the $p_\perp$ distribution to the charm mass and parton densities                                                                  | 14 |
| 2.8  | Sensitivity of the $\eta$ distribution to parton and photon densities . . . .                                                                     | 15 |
| 2.9  | Direct and resolved components of the $p_\perp$ distribution of the charm quark . . . . .                                                         | 15 |
| 2.10 | Massless scheme: charm in the initial state in a LO picture . . . . .                                                                             | 17 |
| 2.11 | Rapidity dependence of the direct and resolved contribution to the charm cross section on $\epsilon_{Pettersen}$ in the massless scheme . . . . . | 19 |
| 2.12 | Cross sections in photoproduction ( $d\sigma/dp_\perp$ ) in the massless scheme .                                                                 | 20 |
| 2.13 | Cross sections in photoproduction ( $d\sigma/d\hat{y}$ ) in the massless scheme . .                                                               | 21 |
| 2.14 | Charm cross sections in photoproduction ( $d\sigma/d\hat{y}$ ) of the 1994 analysis of H1, compared to the massive and massless scheme . . . . .  | 22 |
| 3.1  | The storage ring HERA and the preaccelerators at DESY . . . . .                                                                                   | 24 |
| 3.2  | Integrated luminosity produced of HERA 1992 -1997 . . . . .                                                                                       | 25 |
| 3.3  | The H1 detector at HERA . . . . .                                                                                                                 | 27 |
| 3.4  | The H1 tracking system: side view . . . . .                                                                                                       | 28 |
| 3.5  | The H1 central tracking system: radial view . . . . .                                                                                             | 29 |
| 3.6  | The H1 luminosity system . . . . .                                                                                                                | 31 |
| 3.7  | Overview of the H1 trigger system . . . . .                                                                                                       | 32 |
| 3.8  | The inner $z$ -drift chamber CIZ . . . . .                                                                                                        | 34 |
| 3.9  | The drift cell of the inner $z$ -drift chamber CIZ . . . . .                                                                                      | 35 |
| 3.10 | Calibration of CIZ . . . . .                                                                                                                      | 37 |
| 3.11 | Efficiency and charge of CIZ according to High Voltage . . . . .                                                                                  | 38 |
| 3.12 | Correlation of CIZ-signal wire current and beam current . . . . .                                                                                 | 39 |
| 3.13 | Correlation of CIZ-signal wire current and beam current in the forward, central and backward region . . . . .                                     | 40 |

|      |                                                                                                                                                                  |    |
|------|------------------------------------------------------------------------------------------------------------------------------------------------------------------|----|
| 3.14 | Efficiencies of CIZ after and before rewiringing . . . . .                                                                                                       | 42 |
| 4.1  | Kinematical properties of the $D^*$ meson: direct and resolved . . . . .                                                                                         | 45 |
| 4.2  | Kinematical properties of the $D^*$ meson: acceptance cuts . . . . .                                                                                             | 46 |
| 4.3  | Kinematical properties of the kaons and pions from the $D^*$ and $D^0$<br>decays . . . . .                                                                       | 47 |
| 4.4  | $z$ coordinate of vertex . . . . .                                                                                                                               | 52 |
| 4.5  | Electron measurement of the electron-tagger at $-33$ m . . . . .                                                                                                 | 54 |
| 4.6  | Acceptance function of electron-tagger . . . . .                                                                                                                 | 56 |
| 4.7  | $\Delta M$ fit of $D^*$ signal and $D^0$ signal . . . . .                                                                                                        | 57 |
| 5.1  | $\Delta M$ for all selected events of ST 83 . . . . .                                                                                                            | 62 |
| 5.2  | $\Delta M$ fits for $p_{\perp}$ - bins, weighted sample . . . . .                                                                                                | 63 |
| 5.3  | $\Delta M$ fits for $p_{\perp}$ - bins, "equivalent number of events" . . . . .                                                                                  | 64 |
| 5.4  | $\Delta M$ fits for $\hat{y}$ - bins, weighted sample . . . . .                                                                                                  | 65 |
| 5.5  | $\Delta M$ fits for $\hat{y}$ - bins, "equivalent number of events" . . . . .                                                                                    | 66 |
| 5.6  | Performance of CJC 1994 - 1996 . . . . .                                                                                                                         | 70 |
| 5.7  | $K R_{length}$ and $DCA$ : data and MC . . . . .                                                                                                                 | 71 |
| 5.8  | $\pi R_{length}$ and $DCA$ : data and MC . . . . .                                                                                                               | 71 |
| 5.9  | $\pi_s R_{length}$ and $DCA$ : data and MC . . . . .                                                                                                             | 72 |
| 5.10 | Raw $p_{\perp}$ and $\hat{y}$ spectras, agreement with Monte Carlo . . . . .                                                                                     | 75 |
| 5.11 | Cross sections in function of $p_{\perp}$ and $\hat{y}$ . . . . .                                                                                                | 78 |
| 5.12 | Double differential cross sections in function of $p_{\perp}$ for different $\hat{y}$ regions                                                                    | 79 |
| 5.13 | Double differential cross sections in function of $\hat{y}$ for different $p_{\perp}$ regions                                                                    | 79 |
| 6.1  | Cross Sections of $p_{\perp}$ and $\hat{y}$ , comparison with AROMA/IJRAY<br>prediction . . . . .                                                                | 81 |
| 6.2  | Double differential cross sections $d^2\sigma/dp_{\perp}d\hat{y}$ in regions of $p_{\perp}$ and $\hat{y}$ ,<br>comparison with AROMA/IJRAY predictions . . . . . | 82 |
| 6.3  | Cross Sections of $p_{\perp}$ and $\hat{y}$ , comparison with HERWIG prediction . .                                                                              | 84 |
| 6.4  | Double differential cross sections of $p_{\perp}$ in regions of $\hat{y}$ , comparison<br>with AROMA/IJRAY predictions . . . . .                                 | 85 |
| 6.5  | Double differential cross sections of $\hat{y}$ in regions of $p_{\perp}$ , comparison<br>with HERWIG predictions . . . . .                                      | 86 |
| 6.6  | Cross Sections of $p_{\perp}$ and $\hat{y}$ , comparison with massive calculation, $m_c$<br>and $\epsilon_P$ varied . . . . .                                    | 88 |
| 6.7  | Cross Sections of $p_{\perp}$ and $\hat{y}$ , comparison to massive theory, variation<br>of proton and photon parametrisations . . . . .                         | 88 |
| 6.8  | Double differential cross sections of $p_{\perp}$ in regions of $\hat{y}$ , comparison<br>to massive theory, $m_c$ varied . . . . .                              | 89 |
| 6.9  | Double differential cross sections of $\hat{y}$ in regions of $p_{\perp}$ , comparison to<br>massive theory, $m_c$ varied . . . . .                              | 89 |
| 6.10 | Double differential cross sections of $p_{\perp}$ in regions of $\hat{y}$ , comparison<br>to massive theory, $\epsilon_P$ varied . . . . .                       | 90 |

---

|      |                                                                                                                                                         |    |
|------|---------------------------------------------------------------------------------------------------------------------------------------------------------|----|
| 6.11 | Double differential cross sections of $\hat{y}$ in regions of $p_{\perp}$ , comparison to massive theory, $\epsilon P$ varied . . . . .                 | 90 |
| 6.12 | Double differential cross sections of $\hat{y}$ in regions of $p_{\perp}$ , comparison to massive theory, variation of proton parametrization . . . . . | 91 |
| 6.13 | Double differential cross sections of $\hat{y}$ in regions of $p_{\perp}$ , comparison to massive theory, variation of photon parametrization . . . . . | 91 |
| 6.14 | Cross Sections of $p_{\perp}$ and $\hat{y}$ , comparison to massless theory . . . . .                                                                   | 93 |
| 6.15 | Cross Sections of $p_{\perp}$ and $\hat{y}$ , comparison to massless and massive theory                                                                 | 93 |
| 6.16 | Double differential cross sections of $p_{\perp}$ in regions of $\hat{y}$ , comparison to massless theory . . . . .                                     | 94 |
| 6.17 | Double differential cross sections of $p_{\perp}$ in regions of $\hat{y}$ , comparison to massless theory . . . . .                                     | 94 |
| 6.18 | Double differential cross sections of $\hat{y}$ in regions of $p_{\perp}$ , comparison to massless theory . . . . .                                     | 95 |
| 6.19 | Double differential cross sections of $\hat{y}$ in regions of $p_{\perp}$ , comparison to massless theory . . . . .                                     | 95 |
| 6.20 | Double differential cross sections of $\hat{y}$ in regions of $p_{\perp}$ , comparison to massive and massless theory . . . . .                         | 96 |
| 6.21 | Double differential cross sections of $\hat{y}$ in regions of $p_{\perp}$ , comparison to massive and massless theory . . . . .                         | 96 |

---

# Acknowledgments

First I would like to thank Prof. Dr. Peter Truöl for to giving me the possibility to work within the H1 collaboration at DESY. The trust he putted in me gives me the chance to find my way to work within particle physics and to learn to work independently.

The analysis work was continuously and strongly supported by Felix Sefkow. I could learn a lot from his rich experience. Also Christoph Grab helps me solving the problems of a photoproduction analysis and to understand the theory behind. The common work with Hubert Niggli and Monika Bidulph on photoproduction topics for our analysis is well remembered, too.

A special thank is addressed to the people in the Zürich office at DESY, David Müller, Stefan Hengstmann and Katharina Müller. Our work was partially very close in analysis and hardware. The good atmosphere in the office was always an important support for the big amount of work.

For the times working with CIZ and CIP I would give a big thank to Peter Robmann, Kurt Bösiger and Stefan Steiner. The many times we spend in the North Hall are well remembered.

All other people of the Uni Zürich group, which are still working or have leaved our institute, I give a great thank for the helpful discussion concerning hardware, physics, computing and many other topics: Ueli Straumann, Thomas Walter, Hans Peter Beck, Christian Dollfus and Stephan Egli.

The people of the ETH Zürich sharing the office I would thank for the mutual help: Yorgos Tsiplolitis, Urs Langenegger, Daniel Pitzl and Johannes Gassner.

It was a pleasure to work in the H1-Collaboration and into the Heavy Flavor Working group. A lot of very helpful ideas i get during discussion with people of the various working groups.

Last, but not least I wold thank all my friends outside DESY. Their moral support kept me going in all times. The wonderful times with the Vokalensemble St. Jacobi was always a great enrichment.

This work has been supported by the Swiss National Science Foundation.

---

# Curriculum Vitae

## Personalien:

Name: Martin Erik Gerd zur Nedden  
Geboren: 20. August 1967 in Klagenfurt (Kärnten), Österreich  
Nationalität: Österreich

## Bildungsgang:

1974 - 1981 Volksschule in Innsbruck (Tirol, Österreich) und Primarschule in Zürich  
1981 - 1984 Sekundarschule in Thalwil ZH  
1984 - 1988 Unterseminar an der Kantonsschule Küsnacht ZH  
1988 Kantonale Matura, Typus Unterseminar  
1988 - 1994 Studium der Physik (Mathematik, Philosophie) an der Universität Zürich  
1993 - 1994 Diplomarbeit in Experimentalphysik unter der Leitung von Dr. U. Straumann und Prof. Dr. P. Truöl  
Titel: "Untergrundstudien am H1-Detektor bei HERA"  
1994 Diplom in Experimentalphysik  
1994 - 1998 Wissenschaftliche Mitarbeit beim H1 Experiment am Elektron-Proton Speicherring HERA bei DESY Hamburg,  
1998 Dissertation bei Prof. Dr. P. Truöl.

## DozentInnenverzeichnis:

|              |               |                  |              |
|--------------|---------------|------------------|--------------|
| H. Amman     | C. Amsler     | W. Ballmann      | R. Bannwart  |
| K. Bösiger   | D. Brinkmann  | E. Brun          | R. Durrer    |
| St. Egli     | R. Engfer     | R. Ferber        | P. Gabriel   |
| H. Holzhey   | W. Jauss      | W. Kündig        | M. Mali      |
| P. F. Meier  | C. A. Meyer   | M. Molteni       | V. Mudroch   |
| H. H. Müller | R. E. Pixley  | H. S. Pruyss     | G. Rasche    |
| W. Reichhard | P. Schulthess | J. P. Schobinger | N. Straumann |
| U. Straumann | A. Thellung   | P. Truöl         | D. Wyler     |